CHARACTERIZATION OF THE THERMAL PROPERTIES OF CHEMICAL VAPOR DEPOSITION GROWN DIAMOND FILMS FOR ELECTRONICS COOLING

A Thesis
Presented to
The Academic Faculty

by

Kirkland D. Malcolm

In Partial Fulfillment
Of the Requirements for the Degree
Masters of Science in the
School of Mechanical Engineering

Georgia Institute of Technology

May, 2016

Copyright © Kirkland Malcolm 2016

CHARACTERIZATION OF THE THERMAL PROPERTIES OF CHEMICAL VAPOR DEPOSITION GROWN DIAMOND FILMS FOR ELECTRONICS COOLING

Approved by:

Dr. Samuel Graham, Advisor
School of Mechanical Engineering
Georgia Institute of Technology

Dr. Tequila Harris
School of Mechanical Engineering
Georgia Institute of Technology

Dr. Satish Kumar
School of Mechanical Engineering
Georgia Institute of Technology

Date Approved: [April 19, 2016]

ACKNOWLEDGEMENTS

Many individuals have helped me through my time here at Georgia Tech, and I cannot begin to thank them enough for their time and support. I would first like to thank my advisor, Dr. Samuel Graham, for coaching and teaching me through the research process. I would also like to thank all the past and present members of the EMRL group. Luke Yates and Georges Pavlidis have provided countless hours of support and training in their respective areas of expertise. Dr. Anu Bulusu has also guided me in many aspects of my research in the clean room. I could not have done this without everyone's patience, time, support, and expertise. I would also like to thank my committee members, Dr. Tequila Harris and Dr. Satish Kumar for their time and expertise.

I would also like to thank Major Todd Moulder and Captain Craig Thompson for their mentorship and advice at my time here at Georgia Tech. They have pushed me in my leadership challenges and provided an example of the leader I hope to one day become. I would also like to thank the midshipman of the NROTC Marine Platoon of the Atlanta Consortium in pushing me in my physical training and leadership abilities.

Living close to my family has been such a blessing at my time here at Georgia Tech. My mom and sister have been the greatest emotional support in aiding me in my time here in Atlanta. I would also like to thank my friends in Atlanta, and fellow students at Georgia Tech especially Kenechi Agbim, Steven Bohleman, Cole Skinker, Brendan Place, Andreas Gabrielsen, Lucas Kunsman, Tyler Boring, Chris Elliot, John Murphy and Sam Stowell.

TABLE OF CONTENTS

ACKNOWLEDGEMENTS iii

LIST OF TABLES vii

LIST OF FIGURES viii

SUMMARY xv

CHAPTER 1: INTRODUCTION 1

1.1 Gallium Nitride High Electron Mobility Transistors (HEMTs) 1

1.1.1 Device Background 1

1.2.2 Device Structure 3

1.2 Thermal Reliability 5

1.2.1 Current Substrate Solutions 6

1.2.2 Diamond Substrate 9

1.2.2 Chemical Vapor Deposition (CVD) Diamond 10

1.2.3 Methods of Implementation 15

1.2.4 Issues with Diamond Implementation 17

1.3 Previous Diamond Programs 23

1.4 Research Problem Statement and Research Objectives 25

CHAPTER 2: CHEMICAL VAPOR DEPOSITION DIAMOND 27

2.1 Introduction 27

2.2 The CVD Process 29

2.2.1 Nucleation 29

2.2.2 CVD Growth 30

2.1.1 Growth Techniques 32

2.3 Diamond Samples 34

2.3.1 Issues in Fabrication 38

2.4 Summary and Conclusions 40

CHAPTER 3: THERMAL PROPERTIES OF DIAMOND 42

3.1 Introduction 42

3.2 Device Structure 43

3.2 Raman Spectroscopy 53

3.2.1 Peak Position Method 54

3.2.2 Nanoparticles for Surface Measurements 55

3.2.3 Calibration 56

3.3 Experimental Setup 58

3.4 Results and Discussion 59

3.4.1 Lateral/In-Plane Thermal Conductivity 60

3.4.3 Vertical/Cross-Plane Thermal Conductivity and Thermal Boundary Resistance 69

3.4.4 Temperature Dependence 72

3.5 Summary and Conclusions 75

CHAPTER 4: MATERIAL CHARACTERIZATION USING QUICK SCREENING METHODS 78

4.1 Introduction 78

4.2 Raman Spectra and FWHM 78

4.3 FTIR 84

4.4 XPS 87

4.4 Summary and Conclusion 90

CHAPTER 5: MEASUREMENT AND MODELING OF GAN ON SIC/DIAMOND HEMT DEVICES 92

5.1 Introduction 92

5.2 Device Measurements 93
5.2.1 Thermal Boundary Resistance on Transmission Line Measurements............. 96
5.3 Modeling 98
5.3.1 Temperature Results 102
5.3.2 Substrate and Thickness Comparison... 105
5.3.3 Effect of Diamond Thermal Properties 106
5.4 Summary and Conclusions... 109
CHAPTER 6: CONCLUSION AND FUTURE WORK 111
REFERENCES 115

LIST OF TABLES

Table 1: Material Properties of substrate materials, AlN buffer layer, and GaN layer [12, 23, 24] 8

Table 2: Properties of Bulk Diamond [25, 26] 9

Table 3: GaN-Substrate Thermal Boundary Resistances Summary [48] 20

Table 4: TBRs dependence on growth conditions [46] 21

Table 5: Diamond samples tested for thermal properties 34

Table 6: Change in peak position vs. temperature for diamond calibration 57

Table 7: Cross-plane thermal conductivity and Thermal Boundary Resistance results for Sample A. 71

Table 8: Vertical thermal conductivity and Diamond on silicon TBR obtained from a collaborating university. 72

Table 9: Temperature dependent lateral thermal conductivity measurements for Sample A. 73

Table 10: Diamond FWHM and thermal conductivity comparison 83

Table 11: FTIR comparison of thermal conductivity to integrated area 86

Table 12: sp^3 to sp^2 ratio and comparison 89

Table 13: Thermal properties of materials used in FEA model [11] 98

Table 14: Design parameters used for FEA Model 107

Table 15: Temperature results from various design point 108

LIST OF FIGURES

Figure 1: Aluminum gallium nitride/Gallium nitride (AlGaN/GaN) HEMT applications as radio frequency (RF) modules in satellite communications and power switches in electric vehicles [4, 5] 1

Figure 2: Diagram of material properties for transistor materials. GaN has advantageous properties such as a large band gap, high electron mobility, and high thermal conductivity, which make it an attractive material for power and RF circuits [10]. 3

Figure 3: Graphical representation of a 2-finger AlGaN/GaN HEMT device [14]. 4

Figure 4: Arrhenius plot showing a Mean Time to Failure Plot [18] 6

Figure 5: Schematic of AlGaN/GaN HEMT with thermal path through substrate and TBR with buffer layer. 7

Figure 6: Next generation GaN-on-Diamond HEMT device provide ~ 40°C lower junction temperature and increased power handling over GaN-on-SiC HEMT [19]. 10

Figure 7: IR thermal signatures from GaN on diamond compared to GaN on Si. Peak temperatures have decreased by over 40°C [33] 11

Figure 8: Example of a 3x reduction in the size (gate-to-gate spacing) of an AlGaN/GaN on diamond HEMT when compared to an AlGaN/GaN on SiC HEMT. Devices were made in the Defense Advanced Research Projects Agency (DARPA) Near Junction Thermal Transport (NJTT) program by Raytheon, Inc. [34] 12

Figure 9: Graphical representation of typical CVD Diamond grain structure and its columnar growth structure. The grains grow from seeds on the surface on the substrate and take on a columnar structure which provides anisotropy and vertical property gradients in thermal conductivity [37]. 13

Figure 10: Scanning electron micrograph (SEM) of a CVD diamond sample 355μm thick. The columnar growth and increasing grain size are shown moving up the image. Images of the top surfaces of three samples are shown on the right [40]. 14

Figure 11: Comparison of diamond thickness for columnar growth and grain size in CVD diamond samples courtesy of Dr. Mark Goorsky at UCLA. 15

Figure 12: GaN-on-diamond HEMT Device process flow following “double flip” process [41] 16

Figure 13: Wurtzite crystal structure is in GaN, (Aluminum Nitride) AlN, and AlGaN while diamond has a cubic structure [42]. 17

Figure 14: SEM image of GaN on Diamond interface with SiN dielectic layer 19

Figure 15: GaN and diamond temperatures measured by Raman thermography on the drain side in a two finger GaN-on-diamond transistor. Increasing the TBR to $27m^2K/GW$ increased peak temperature by over 60°C [49]........................... 19

Figure 16: Comparison of TBR and substrate thermal conductivity for GaN on Si/SiC/Diamond. 21

Figure 17: Effective thermal boundary resistance (TBR_{eff}) of GaN-on-diamond wafers as a function of the SiN layer thickness. The thermal conductivity of the amorphous SiN layer is estimated to be 1.9 W/m-K [46]. 22

Figure 18:Schematic cross section of GaN-on-diamond showing thermally unoptimized and optimized designs, before and after the removal of the AlGaN transition layer(left) and experimental results of 2 finger 100µm wide AlGaN/GaN HEMT showing varying substrates [28]. 23

Figure 19: Average in-plane grain size versus film thickness for the columnar-nanocrystalline diamond films. The transition from single crystallites to columnar grains take place in the 1st micron of diamond [35]....................... 25

Figure 20:sp^3-hybrid orbital(left) and diamond crystal structure (right) [61].................. 28

Figure 21: sp^2-hybrid orbital (left) and graphite crystal structure (right) [61]................ 28

Figure 22: Schematic of the physical and chemical process occurring during diamond CVD [26] 30

Figure 23: A simplified Bachmann triangle C-H-O composition diagram. The formation of sp^3 bonds requires highly specific carbon to hydrogen to oxygen ratios [26]. 31

Figure 24: Schematic of the reaction process occurring at the diamond surface. This creates a stepwise addition of CH_3 species and diamond growth [25, 26] 32

Figure 25: Examples of the most common types of CVD reactors. (a) Hot filament (b)'NIRIM-type' Microwave Plasma (c) 'ASTEX-type' microwave plasma (d) DC arc jet (plasma torch) [26] 33

Figure 26: Diamond Anvil sample sent from Texas State University 35

Figure 27: Diagram of the various $1cm^2$ die that were fabricated on a 3 inch CVD diamond on Si wafer for both Raman thermography and TDTR measurement of thermal conductivity. Each die from the wafer was 1 cm x 1 cm in size.

Samples labeled “common” contained both TDTR and Raman samples in close proximity on the same die in order to make comparisons between the techniques without being impacted by material variation across the wafer. Materials characterization was performed by collaborators at UCLA on die taken from the wafer after thermal conductivity testing was completed. 36

Figure 28: (left) Sample B design for Raman thermography to measure in-plane and cross-plane thermal conductivity. (Right) Common sample to measure thermal properties using TDTR and Raman thermography within 1.2mm of each other. 37

Figure 29: (left) Bulk Sample B shows a transparent thick diamond sample with a high thermal conductivity (1927 W/m-K), and (right) Bulk sample E shows an opaque thick diamond sample with a lower thermal conductivity (714 W/m-K). 38

Figure 30: 5x magnification of fabrication issues due to high surface roughness in the samples. (a) non continuous heaters did not allow for heat dissipation through the heater. (b) and (c) show samples with high surface roughness that did not dissipate heat uniformly. Samples with 30nm RMS or greater surface roughness were not able to be measured... 39

Figure 31: Sample showing silicon etching was not performed to the specifications of the mask. 40

Figure 32: Test structure for lateral thermal conductivity 44

Figure 33: Quarter symmetry FEM of lateral heaters comparing finite element conductivity to calculated thermal conductivity using Fourier’s Law............ 45

Figure 34: Membrane geometry used to determine optimal length to width ratio 45

Figure 35: Normalized thermal conductivity compared to membrane size when length is held constant. The maximum occurs at a length to width ratio of 5:1........... 46

Figure 36: Membrane structure A designed for lateral/ in-plane thermal conductivity measurements.. 47

Figure 37: Membrane structure B designed for lateral/ in-plane thermal conductivity measurements.. 47

Figure 38: Test structure for vertical thermal conductivity measurements showing the locations of measurements on top of the heater using the nanoparticle, the through thickness average of the diamond, and the silicon surface temperature (left) and a 5x magnification of the actual ring structure (right). 48

Figure 39: 5x microscope image of diamond ring structures used for vertical thermal conductivity and TBR 49

Figure 40: FEA Model with temperature profile (left) and path in which sensitivity analysis was conducted (right). 50

Figure 41: Sensitivity analysis of vertical ring structures along silicon surface. 50

Figure 42: Vertical/ Cross-plane thermal conductivity unfilled ring structures. 51

Figure 43: Vertical/ Cross-plane thermal conductivity filled ring structures 52

Figure 44: Wafer layout for Round Robin program depicting Raman and TDTR samples. 52

Figure 45: 1 cm^2 samples used in round robin program (a) Common sample for both TDTR and Raman measurements. (b) Raman test structures for lateral and vertical thermal conductivity measurements. (c) TDTR test structures. 53

Figure 46: Common samples includes lateral, vertical measurements for Raman thermography as well as TDTR structures to avoid spatial variations in diamond quality. 53

Figure 47: A schematic of a Raman spectrum with peak positions (ω) shifting to the left with increasing temperatures in the material. 54

Figure 48: Image of nanoparticles used for surface measurement on heater surface for vertical thermal conductivity measurements 55

Figure 49: Raman peak of TiO_2 is centered around 144 cm^{-1}. 56

Figure 50: Temperature calibration from change in temperature to change in peak position of diamond. 57

Figure 51: Experimental setup on Renishaw InVia Raman system using a 488nm laser (left) and schematic showing the calibration of diamond using known calibration of silicon reference sample (right). 58

Figure 52: Magnified image of Sample B. Sample B has both lateral and vertical test structures. The vertical structures are on the right and the lateral structures are on the left. 60

Figure 53: Finite Element Model of lateral thermal conductivity devices 61

Figure 54: Sample A wafer depicting location of samples measured for thermal properties. 62

Figure 55: Sample A thermal conductivity measurements. The experimental data fit a lateral thermal conductivity of 49 ±4 W/m-K. 63

Figure 56: Measurements obtained on Sample A from Bristol University. (Left) Shows data from the center of the wafer. (Right) shows data from the edge of the wafer. 64

Figure 57: TDTR schematic of lateral thermal conductivity measurements. TDTR at Georgia Tech obtained 55.7 W/m-K on the top side and 59.8 W/m-K from the bottom-side. 65

Figure 58: Sample B thermal conductivity measurements. Due to changing growth conditions, the lateral thermal conductivity of sample B was 2.14x higher than the sample A. 66

Figure 59: Sample B's lateral thermal conductivity measurement using asymmetric heaters. 67

Figure 60: TDTR, Raman thermography, 3-omega, and electrical resistance measurement comparison on Sample B3. 68

Figure 61: Spatial variation in lateral thermal conductivity measured using Raman thermography and TDTR from various institutions 69

Figure 62: FEA model of 100μm diameter vertical ring structure. This model was used to fit the various temperature profiles to their corresponding thermal conductivities. 70

Figure 63: Vertical thermal conductivity measurements of Sample A. A FEM model was fit to the experimental data obtained from various power conditions on the ring structure. The model uses $k_{lateral}$=49 W/m-K, $k_{vertical}$=155 W/m-K, TBR=30m^2K/W 71

Figure 64: Temperature profile based on varied base temperature conditions to determine temperature dependence of lateral thermal conductivity of Sample A. 73

Figure 65: SEM images from UCLA of sample B. This lower carbon growth rate increased columnar growth in the diamond allowing for higher anisotropic thermal conductivity. 74

Figure 66: High Resolution Transmission Electron Microscope (HRTEM) image of Sample B's Diamond on Silicon interface via Dr. Mark Goorsky at UCLA. . 75

Figure 67: Cross section (111) dark field images showing grains with similar orientation via Dr. Mark Goorsky at UCLA of companion sample to Sample B. 75

Figure 68: Natural Diamond Ultra Violet (UV) Raman spectra. The sharp peak at 1332 cm^{-1} corresponds to the high quality diamond. 79

Figure 69: Horiba Jobin Yvon Raman Spectroscopy Setup using UV laser at 325nm. .. 80

Figure 70: UV Raman Spectra comparison of various samples. Diamond reference refers to the bulk diamond qualities and Sample A has a lateral thermal conductivity of 49 W/m-K. 80

Figure 71: FWHM Graphical representation on a diamond peak centered around 1332 cm^{-1} 82

Figure 72: Thermal conductivity vs. FWHM for free standing diamond 83

Figure 73: Thermo Scientific Nicolet iS50 FT-IR spectrometer at the Georgia Tech's Organic Cleanroom. 84

Figure 74: The IR absorption spectra and the measured integrated absorption between 2760 and 3030 cm^{-1} [75]. 85

Figure 75: FTIR results showing CH stretching region from 2760cm^{-1} to 3030cm^{-1} relation to thermal conductivity 86

Figure 76: Graphical representation of FTIR integrated area to thermal conductivity.... 87

Figure 77: Thermo K-Alpha XPS at Georgia Institute of Technology 88

Figure 78: XPS of Bulk Sample F (left) and Sample A (right). The sp^2 content in Sample A shows the poor quality in the microstructure. 89

Figure 79: 10x360μm AlGaN/GaN HEMT on SiC substrate provided by CREE. The red dots represent the locations of the results at various power conditions. 93

Figure 80: Experimental setup for powering HEMT and 100x lens used to take thermal measurements (left) and Renishaw InVia Raman system (right) 94

Figure 81: Diagram of HEMT device and location of measurements. Measurements were taken on the drain side of the channel. Raman measurements in GaN take a volumetric average over the spot size and through the GaN thickness.94

Figure 82: Temperature measurements of GaN in 10x360μm HEMT in center of 5th channel. 200°C was the temperature limit that was set to keep average device reliability over 10^5 hours 95

Figure 83: Transmission Line Measurement (TLM) schematic showing direction of temperature profile 96

Figure 84: Schematic of structure layout for a sing rectangular heat source on complex, multilayered structure. (a) Top view of the xy-plane. (b) Side view of the xz plane [80]. 97

Figure 85: Temperature decay through TLM for GaN on SiC. Each data point corresponds to a temperature measurement made in the channel and the curves

represent changes in the GaN on SiC TBR. Using the analytical solution, the TBR was determined to be 65.1 m^2K/GW 98

Figure 86: Actual GaN HEMT device structure (left) and GaN HEMT device modeled in ANSYS (right). The effective stack resistance represents the layers under the substrate that were modeled as one layer. The thermal resistance of this layer was altered to match the temperature profile in the highest power condition in the experimental results. 99

Figure 87: Meshing and Temperature Profile of 10x360μm HEMT Structure. Finer mesh was used in the area of heat generation and were Raman measurements were taken. 100

Figure 88: Effective stack resistance matching at 7 W/mm. The orange dotted line represents the volumetric average temperature of the Raman location. 101

Figure 89: Geometry of quarter symmetry model. Areas where heat fluxes were applied. Constant base temperature of 30°C was held on the bottom surface with adiabatic conditions on the sides and top of the model. 102

Figure 90: FEA Model to experimental temperature results comparison. Based on the optimized stack resistance, the model's volumetric average temperature was within the uncertainty of the experimental measurements. 103

Figure 91: Raman averaged temperature over the 1 μm spot size and through the 1.4μm thick GaN layer compared to max temperature at various power conditions. 104

Figure 92: Maximum power density using device geometry, limiting the temperature to 200°C. Diamond substrates with the same TBR and lateral thermal conductivity of 750 W/m-K and vertical thermal conductivity of 1500 W/m-K. 105

Figure 93: Maximum temperature for various substrate thickness at 5 W/mm. The minimum temperature for both SiC and Diamond substrates occurred at 300μm. 106

Figure 94: Thermal conductivity gradient used in parametric study. In-plane/Cross-plane thermal conductivity 107

Figure 95: Depth temperature profile for various design points at 5 W/mm power density and 300μm substrate thickness. 108

SUMMARY

Chemical Vapor Deposition (CVD) Diamond is a promising technology for the passive cooling of high power Gallium Nitride (GaN) semiconductor devices. The high thermal conductivity diamond can be placed near the junction of the GaN transistor either by direct growth on the backside of the GaN or by bonding it to the GaN. In both cases, the thermal resistance near the interface with the diamond and any semiconductor it is attached to has the potential for large thermal resistance that limits the effectiveness of the diamond layer.

In this work, several techniques are developed to understand the thermal conductivity of thin diamond films and the thermal boundary resistance with Si and GaN substrates. Anisotropic thermal conductivity measurements are made using Raman spectroscopy temperature mapping along with electric resistance heating. For devices, the thermal boundary resistance is measured using transistors as the heat source and thermal mapping using Raman spectroscopy. Quick screening methods based on Raman, Fourier Transform Infrared Spectroscopy (FTIR) and X-Ray Photoelectron Spectroscopy (XPS) are also correlated with the thermal properties of the films. Based on this work, the properties of CVD diamond films near the interface of semiconductor substrates is revealed for layers less than 5 μm in thickness and their impact or limitations on thermal management shown through simulations.

CHAPTER 1: INTRODUCTION

1.1 Gallium Nitride High Electron Mobility Transistors (HEMTs)

As the market for cellular, radar systems, and broadband access continues to increase and expand into the next generation capabilities (cf., Figure 1), increased capacity of these electronics are needed to transmit and receive data [1, 2]. As manufacturers continue to push the technology's output in power and frequency, a key limiting factor of the technology is related to device reliability under high operational powers which demands attention to advanced thermal management schemes. The dimensional scaling of high-power electronic components especially compound semiconductor devices has incrementally increased power dissipation where localized hot spots have heat fluxes above 1kW/cm^2 and volumetric heat generation above 1kW/cm^3 [3].

Figure 1: Aluminum gallium nitride/Gallium nitride (AlGaN/GaN) HEMT applications as radio frequency (RF) modules in satellite communications and power switches in electric vehicles [4, 5]

1.1.1 Device Background

Compared to previous transistor technology such as metal-oxide-semiconductor field-effect transistors (MOSFETs) or complementary metal-oxide-semiconductors (CMOS), AlGaN/GaN heterostructure field effect transistors (HFETs) present a

compelling technology for future advanced RF communication systems. These devices are termed heterostructure field effect transistors because: A) they utilize two spontaneously polarized materials of different band gaps to create a two dimensional electron gas (2DEG) with high carrier mobility at their interface [6] and B) two ohmic source and drain contacts with the 2DEG along with a Schottky gate contact allow the control of these carriers through variations in the electric field. Because of the formation of the 2DEG, these devices do not need to be doped which can increase scattering and reduce the high carrier mobility, although there is a small amount of unintentional doping that occurs in the growth process. AlGaN/GaN based devices achieve a high critical breakdown field on the order of 3 MV cm^{-1} [7], which is approximately ten times larger than Si and five times that of the Gallium arsenide (GaAs) devices. As in all transistors, increasing junction temperature in the HEMT yields a decrease in electron mobility and dissipated power. In addition, higher junction temperatures are known to cause reliability issues [8].

The material properties of Gallium nitride (GaN), compared to competing materials, are presented in Figure 2. GaN has a wide band gap (3.4 eV at room temperature), a high electron mobility, large breakdown field, and relatively high thermal conductivity, which is advantageous in the design of HEMTs [9]. The high electron mobility allows for high switching capabilities leading to higher frequencies devices. The large breakdown field, and high saturation velocity allow for the achievement of high power. GaN's higher thermal conductivity is advantageous for thermal management that reduces the overall thermal resistance. AlGaN/GaN HEMTs have the potential to greatly

impact both power switching and RF communication applications because of their attractive combination of material properties, especially compared to current technology.

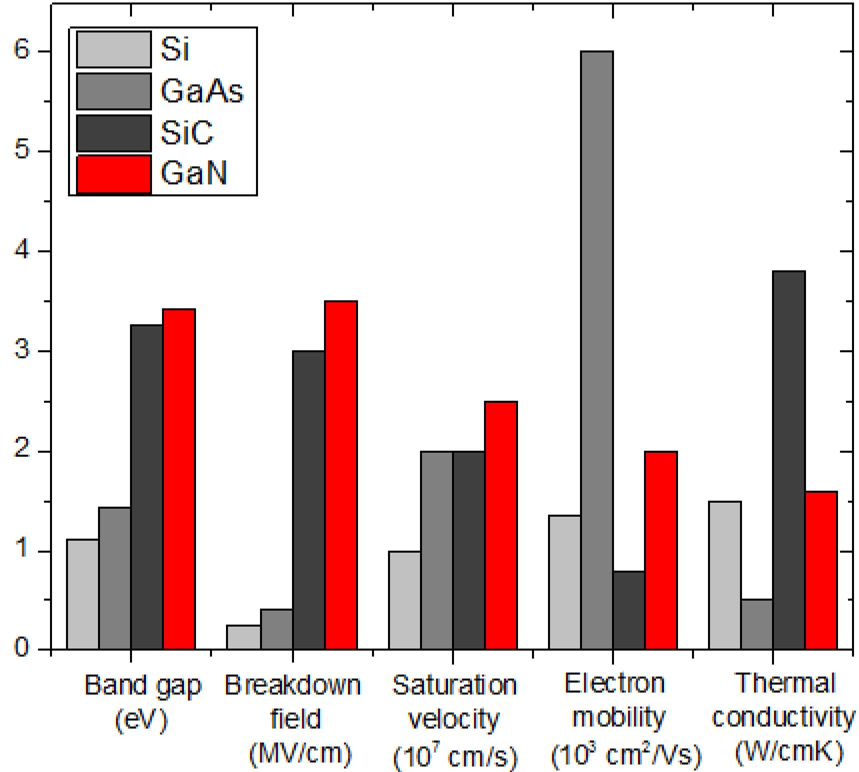

Figure 2: Diagram of material properties for transistor materials. GaN has advantageous properties such as a large band gap, high electron mobility, and high thermal conductivity, which make it an attractive material for power and RF circuits [10].

.

1.2.2 Device Structure

The typical AlGaN/GaN HEMT structure is shown in Figure 3. Most commercially available devices are fabricated by depositing a thin layer of Aluminum Nitride (AlN) on a substrate for the growth of the GaN layer. Silicon carbide (SiC) is the most common substrate material due to its high thermal conductivity of 490 W/m-K at room temperature, and its low lattice mismatch with GaN [11, 12]. GaN is typically grown using metalorganic chemical vapor deposition (MOCVD). A thin layer (usually

20-30 nm) of AlGaN is pseudomorphically grown on top of the GaN layer using either molecular beam epitaxy (MBE) or MOCVD [13]. This psuedomorphic growth of the AlGaN layer stretches the AlGaN lattice constant to that of the GaN, creating a large tensile strain. This piezoelectric polarization allows for the movement of free carriers in the interface. The ohmic (source and drain) and Schottky (gate) contacts are then deposited[11]. Each gate is referred to as a finger, where HEMTs can be single to multi fingered devices. Typical device nomenclature includes the number of fingers by the gate width such as 10x360μm which means there are 10 transistor gates that cover 360 μm wide channels. Power densities are given in units of W/mm, which describe the total power dissipated over the total gate periphery.

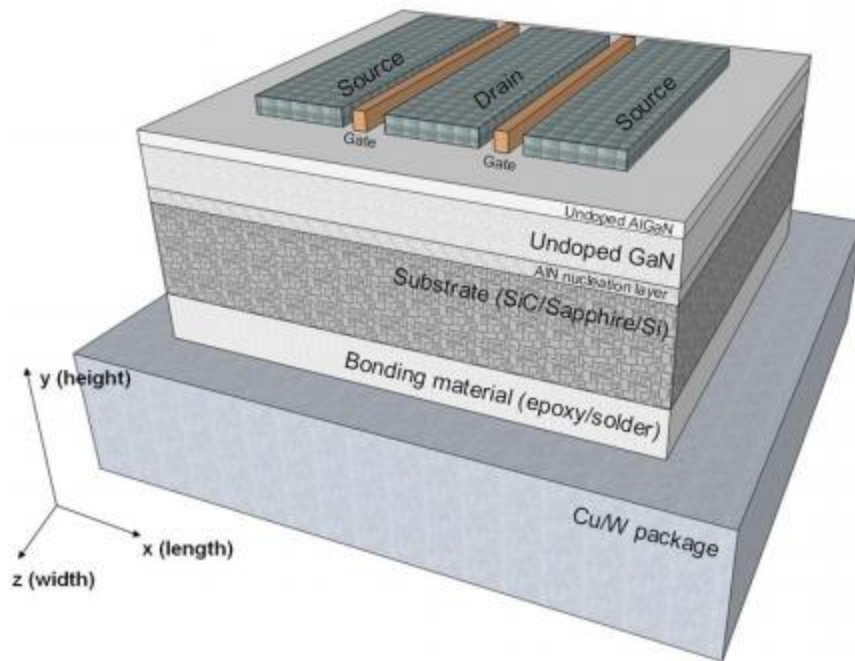

Figure 3: Graphical representation of a 2-finger AlGaN/GaN HEMT device [14].

1.2 Thermal Reliability

As GaN HEMT devices continue to increase in power dissipation over constant areas, power density continues to increase. This places a greater importance on the device's thermal management, which is the limiting factor in the device's performance and reliability over time. Power densities as high as 40W/mm in RF and >7 W/mm in direct current (DC) have been demonstrated [15]. Frequencies well exceeding 300 GHz have been shown [16] while having the device operate at temperatures greater than 200°C. However in practical applications, typical devices operate only up to 5–7W/mm in DC to prevent device failure due to prolonged excessive heating [17]. High peak temperatures in devices can severely decrease the time to failure as seen in Figure 4, where operating above 200°C leads to an average failure time of greater than 10^5 hours whereas 310°C peak temperature fails at less than 10^2 hours [18]. This exponential decrease in reliability with increasing temperatures creates a maximum temperature limit around 200°C. Reliance on the conventional substrate materials, silicon and silicon carbide through passive cooling techniques continue to limit the capability of GaN HEMT technology from their full potential. In order to operate at high heat fluxes of >1 kW/cm^2 and high power densities of >7W/mm for DC conditions, novel thermal management techniques are necessary for continued improvement.

Many large-scale electronic systems utilize active and passive thermal management techniques that greatly increase the overall size, weight, and power (SWaP) of the electronic system [19]. Many of these technologies place size and weight at a premium for portable purposes especially for applications in the aerospace field. By implementing novel and aggressive thermal management techniques into GaN HEMT

thermal packaging, size and weight can be reduced while power and frequency can increase, unlocking the full potential of wide bandgap power electronics.

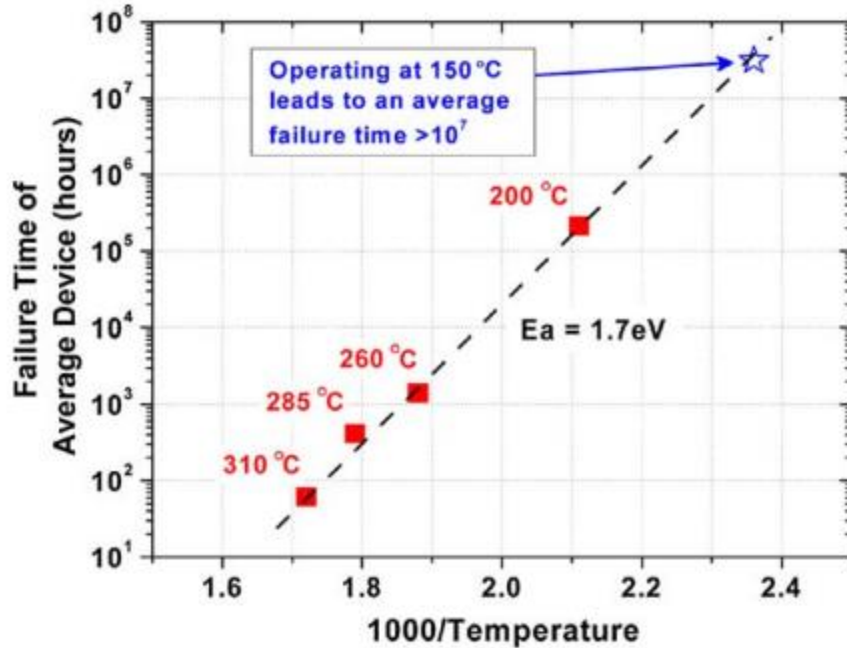

Figure 4: Arrhenius plot showing a Mean Time to Failure Plot [18]

1.2.1 Current Substrate Solutions

These high temperatures over 200°C will degrade the HEMT more rapidly over time; this requires novel thermal management techniques to reduce the peak temperature by decreasing the overall thermal resistance from junction to ambient conditions. Figure 5 shows the typical heat dissipation pathway in an AlGaN/GaN HEMT. The choice and geometry of the substrate has a large effect on the heat dissipation capabilities of the device to act as a heat spreader. High thermal conductivity materials spread the heat more easily away from the junction or hot spots in the device, whereas materials with lower conductivities impede heat flow to the ambient conditions increasing the peak temperatures in a device. Thermal conductivities of substrates used in AlGaN/GaN

HEMTs can vary by an order of magnitude. When choosing a substrate material for thermal management purposes, more factors must be considered than solely the material's thermal conductivity. Other factors to consider include coefficient of thermal expansion (CTE), lattice constants, thermal boundary resistance (TBR), electrical resistivity, and overall costs. Large differences in the CTE or lattice constants can lead to crystallographic defects as the device is operated and can see temperature variations over 200°C. Some substrates require a buffer layer between the GaN and substrate. This buffer layer is required due to a lattice mismatch with GaN and the substrate. Buffer layers decrease the residual stress, but create a thermal boundary resistance which impedes heat flow. An electrically resistive material is required to insulate the AlGaN/GaN active region.

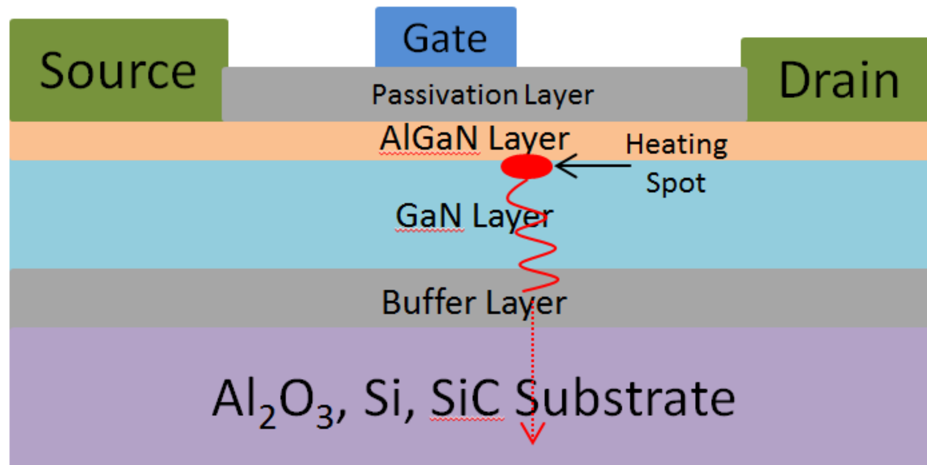

Figure 5: Schematic of AlGaN/GaN HEMT with thermal path through substrate and TBR with buffer layer.

The first GaN HEMT area of research was with a sapphire substrate for the use of light emitting diodes (LEDs) [20]. However, the utilization of sapphire as a substrate proved troublesome due to the low thermal conductivity (27.2 W/m-K) [21], large lattice

mismatch and difference in thermal expansion coefficient between the epitaxial layer and the substrate [22]. These material issues brought rise to new materials that more closely matched the structure of GaN and had higher thermal conductivities. Current GaN HEMT technology is dominated by silicon (Si) and silicon carbide (SiC) substrates for high power applications. This is due to the abundance of and relatively low cost of silicon and the mass manufacturing for SiC. The properties of substrate materials are found in Table 1.

Table 1: Material Properties of substrate materials, AlN buffer layer, and GaN layer [12, 23, 24]

	Al_2O_3	Si	6H-SiC	Diamond	AlN	GaN
Thermal conductivity (W/m-K)	27	149	490	Varied	290	130
Lattice constant	4.758	5.431	3.08	3.567	3.112	3.189
Coefficient of Thermal Expansion (10^{-6}/K @ 300K)	6.66	2.6	4.3	1.5	4.15	5.59
Lattice (Mismatch, %)	33	41	3.5	11	2.5	-
CTE (mismatch, %)	-20	53	23	73	26	-

Unfortunately, the future potential of AlGaN/GaN HEMTs is yet to be unlocked as lower thermal conductivity substrates limit the performance of these devices. As peak temperatures increase, electron mobility decreases as well as dissipated power. These high temperatures can lead to reliability issues so a more aggressive thermal management approach is necessary.

1.2.2 Diamond Substrate

Diamond as a material is known to have advantageous properties for AlGaN/GaN HEMTs as seen in Table 2. As a bulk material, diamond has a high thermal conductivity, and is electrically insulating [25].

Table 2: Properties of Bulk Diamond [25, 26]

Extreme mechanical hardness (90 GPa)
Strongest known material, highest bulk modulus ($1.2x10^{12}$ N/m^2)
Highest known thermal conductivity at room temperature (2000W/m-K)
Low coefficient of thermal expansion ($0.8x10^{-6}$K)
Electrical Insulator (10^{16} Ω at room temperature)
Corrosion Resistant

These properties and the lack of abundance of natural diamond have driven scientist to synthesize diamond in the laboratory. These fabricated diamonds have been synthesized for over 45 years under the high-pressure high temperature (HPHT) technique, where metal solvated carbon experiences pressures from 50-100 kbar and temperatures as high as 2300 K [25] until diamond crystalizes. While this process is useful for applications such as cutting and machining, the formation of single crystals limits the applications in which these industrial diamonds can be used. Although, direct growth of GaN on single crystal diamond has been proven successful [27], the size of the single crystal substrates are too small and do not prove feasible for real world applications [28]. This brought need for a process to synthesize diamonds that could be used as a heat spreader and heat sink in a thin film form [29].

1.2.2 Chemical Vapor Deposition (CVD) Diamond

Instead of replicating the natural way to produce diamond, scientists in 1958, investigated experiments where the thermal decomposition of carbon carrying gases under reduced pressure were capable of growing diamond on the surface of natural diamond [26]. Diamond was produced by the singular addition of carbon atoms to existing diamond to form a tetrahedrally bonded carbon structure [29]. The chemical vapor deposition (CVD) process has continued to be improved since its inception in the 1950s, with varying techniques and processes which will be discussed later in Chapter 2. This process creates films that are polycrystalline, rather than single crystal GaN, Si, and SiC. These polycrystalline diamond films are sensitive to the precise growth conditions and show mechanical and electronic properties comparable to natural, single crystal diamond [25]. The CVD diamond processes has allowed researchers to use high thermal conductivity diamond substrates with thermal conductivities capable of 2000W/m-K used as a heat sink and heat spreader in passive cooling techniques [30-32].

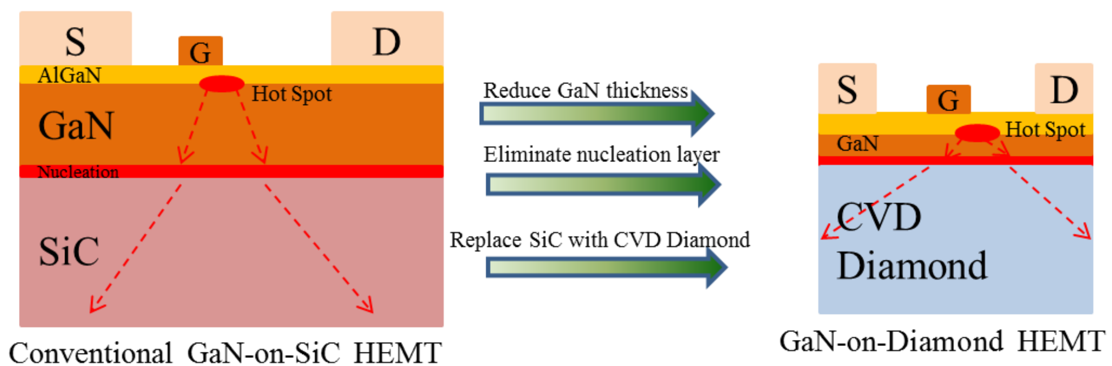

Figure 6: Next generation GaN-on-Diamond HEMT device provide ~ 40°C lower junction temperature and increased power handling over GaN-on-SiC HEMT [19].

These AlGaN/GaN HEMT devices on diamond substrate will operate at much lower junction temperatures under similar power conditions or the reduction of the

overall size and weight as seen in Figure 6. These improvements include a reduction in thickness of the GaN layer, potential elimination of the nucleation layer, and the replacement of the SiC with the CVD diamond substrate increasing the thermal conductivity by over 3x [33]. Figure 7 depicts the change in temperature distribution on a GaN on Diamond device compared to a silicon substrate through infrared spectroscopy. By moving the high conductivity diamond as close as possible to the hotspot in these devices, the thermal resistance will decrease by minimizing the thickness of low thermal conductivity GaN while also allowing the high thermally conductive heat spreading materials to be closer to the active region. These improvements will ultimately improve the ability to increase the maximum output power as well as the thermal reliability of the devices. Previous diamond programs have shown that a 3x decrease in area with the same power output and temperature can be accomplished by using diamond instead of SiC which can be seen in Figure 8 [34].

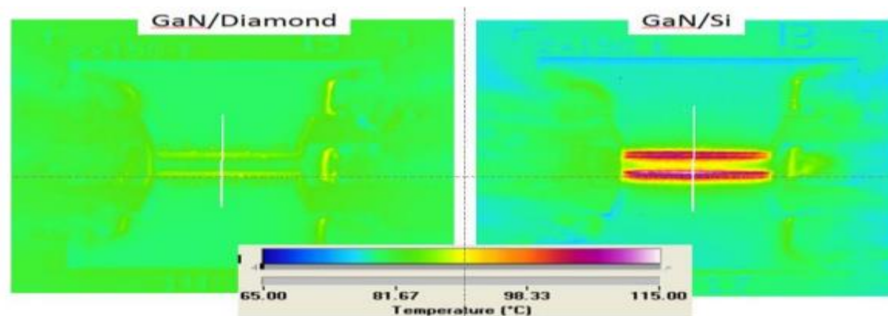

Figure 7: IR thermal signatures from GaN on diamond compared to GaN on Si. Peak temperatures have decreased by over 40°C [33].

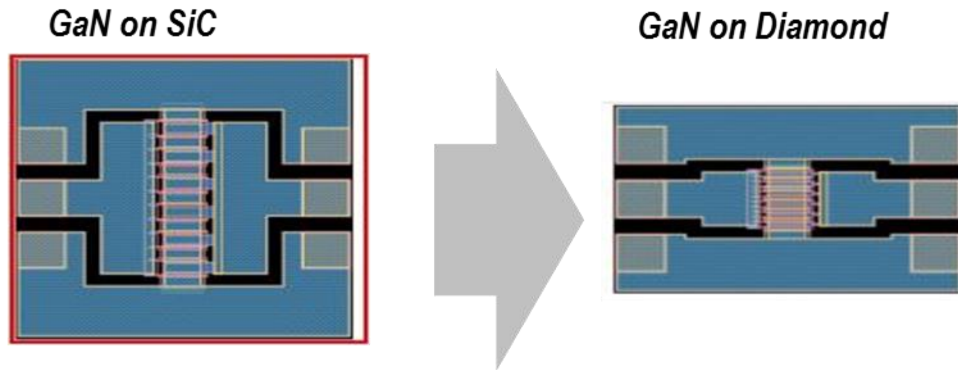

Figure 8: Example of a 3x reduction in the size (gate-to-gate spacing) of an AlGaN/GaN on diamond HEMT when compared to an AlGaN/GaN on SiC HEMT. Devices were made in the Defense Advanced Research Projects Agency (DARPA) Near Junction Thermal Transport (NJTT) program by Raytheon, Inc. [34]

As seen in Figure 9 and Figure 10 diamond nucleates on the substrate surface and growth proceeds in three dimensions until the crystals coalesce. Once a continuous film is formed, the only way growth can precede is upwards. This creates a polycrystalline film with many grain boundaries and defects, while also exhibiting a columnar structure extending upwards. As the film thickness increases, so does the crystal size, decreasing the defects and grain boundaries [25, 26]. Under these growth conditions, the average in-plane dimensions of the grains increase with the distance z from the substrate depending on the initial nucleation density and the growth parameters as seen in Figure 9 [35].

The anisotropy in the shape of the grains as seen in Figure 9 and Figure 11 creates an out-of-plane or vertical size much greater than the in-plane or lateral size. Scattering at the grain boundaries is the main phonon scattering mechanism [36, 37] which causes better heat conduction along the columns or in the vertical direction rather than across adjacent grains due to higher scattering rates. Research has shown a large dependence on the layer thickness for both components of k, the thermal conductivity, with an anisotropy ratio, $k_{vertical}/k_{lateral} \approx 1.2\text{-}2$ [35, 38, 39]. More information on the chemistry

and parameters that influence the grain size and columnar growth of CVD diamond will be discussed in Chapter 2.

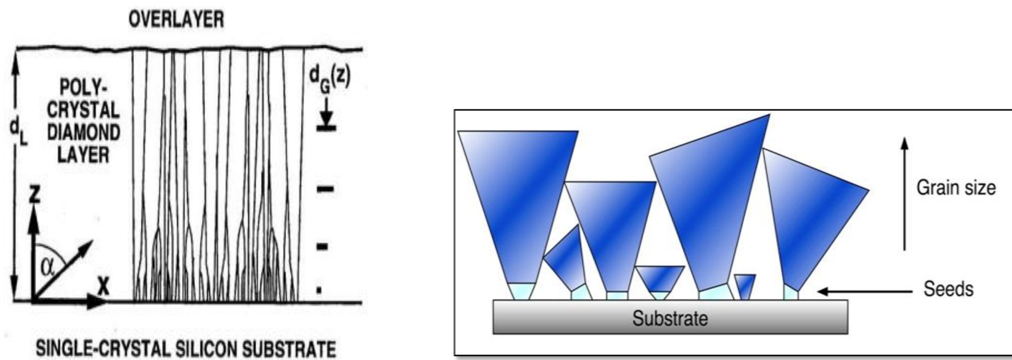

Figure 9: Graphical representation of typical CVD Diamond grain structure and its columnar growth structure. The grains grow from seeds on the surface on the substrate and take on a columnar structure which provides anisotropy and vertical property gradients in thermal conductivity [37].

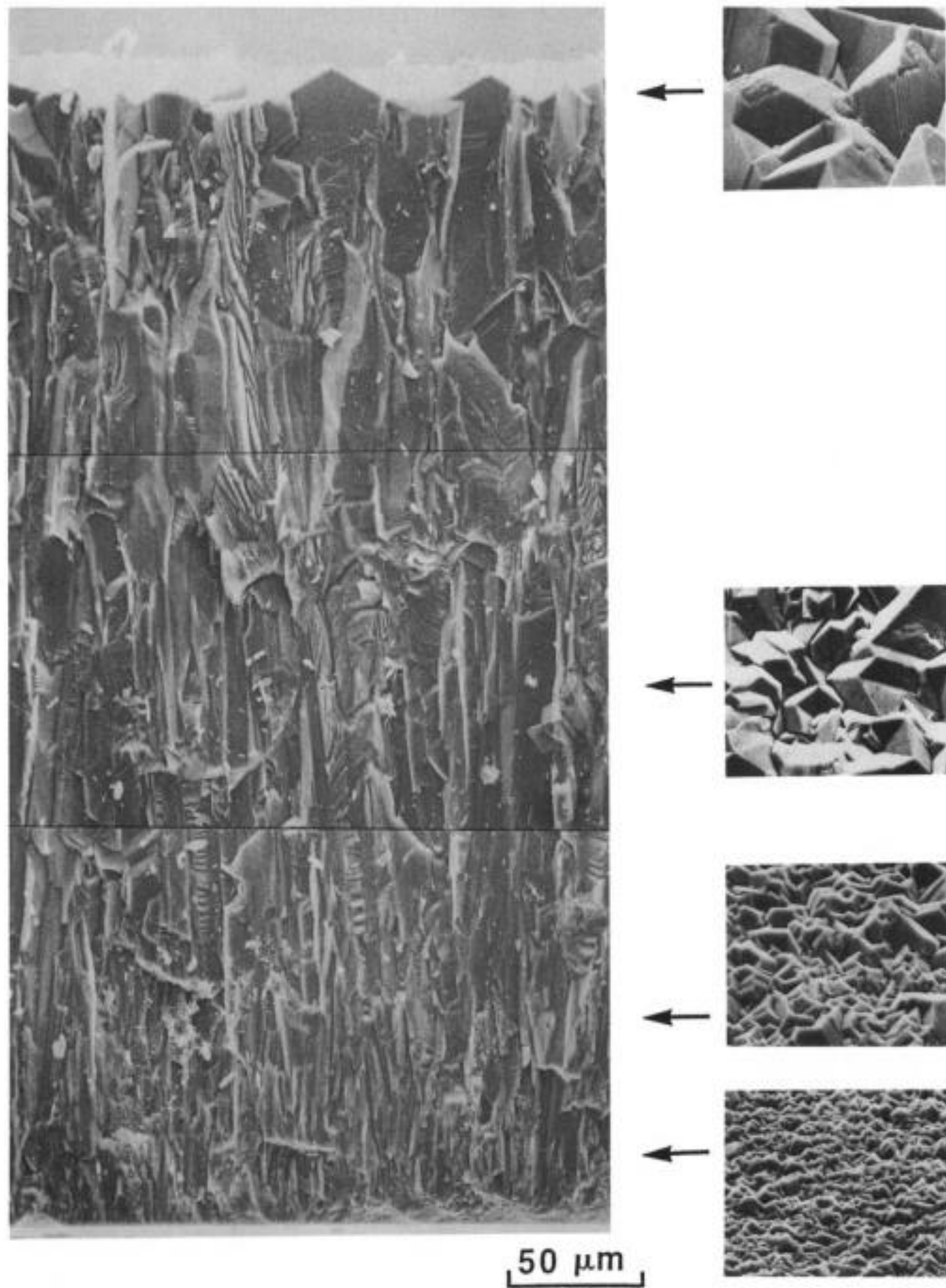

Figure 10: Scanning electron micrograph (SEM) of a CVD diamond sample 355μm thick. The columnar growth and increasing grain size are shown moving up the image. Images of the top surfaces of three samples are shown on the right [40].

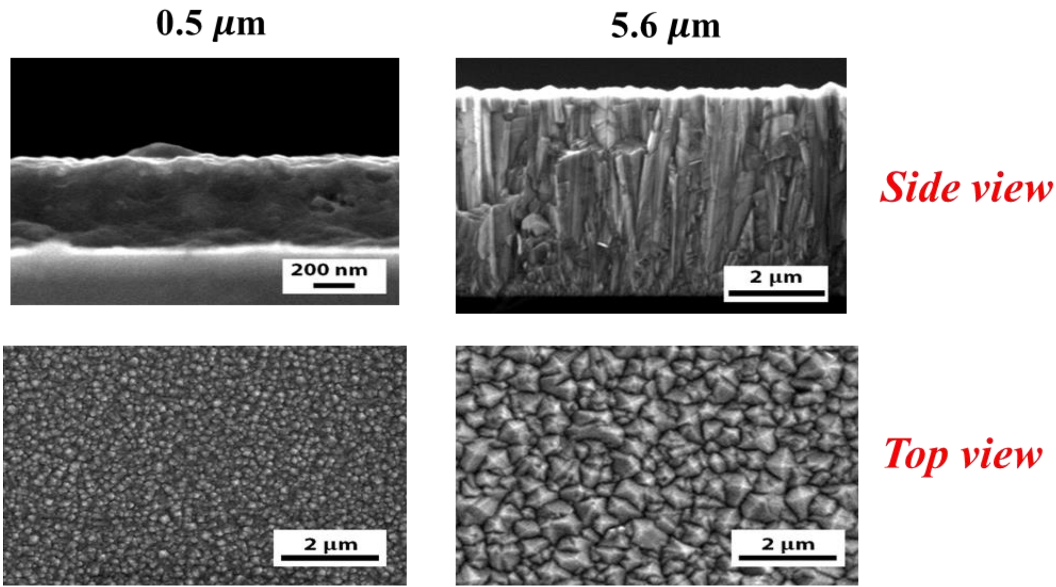

Figure 11: Comparison of diamond thickness for columnar growth and grain size in CVD diamond samples courtesy of Dr. Mark Goorsky at UCLA.

1.2.3 Methods of Implementation

In order to grow diamond on GaN there are two main methods that are employed. The first method of application of GaN-on-Diamond HEMT devices is through the use of a sacrificial substrate such as SiC or Si seen in Figure 12. The process begins with GaN HEMT epitaxial layers grown on silicon. An epilayer transfer is performed twice in order to preserve the orientation of the epilayers, which is referred to as a double flip process. The GaN-epilayer structure is bonded to another silicon wafer creating a silicon-GaN-silicon stack. The second silicon wafer, a sacrificial carrier for the GaN layers, allows for the removal of the growth silicon substrate. The growth silicon wafer is removed using grinding and selective dry etching that leaves the GaN epilayers flipped, exposed, and mounted on top of the sacrificial carrier. The buffer-layer surface is rinsed in de-ionized water and a dielectric layer is deposited after which the structure can receive the diamond. Finally, a CVD diamond wafer is attached to the flipped GaN

epilayers using a 50 nm adhesion layer as shown in step c and the sacrificial carrier is polished away [41]. This adhesion layer creates a thermal boundary resistance between the GaN and diamond which impedes the heat flow from the junction to ambient conditions.

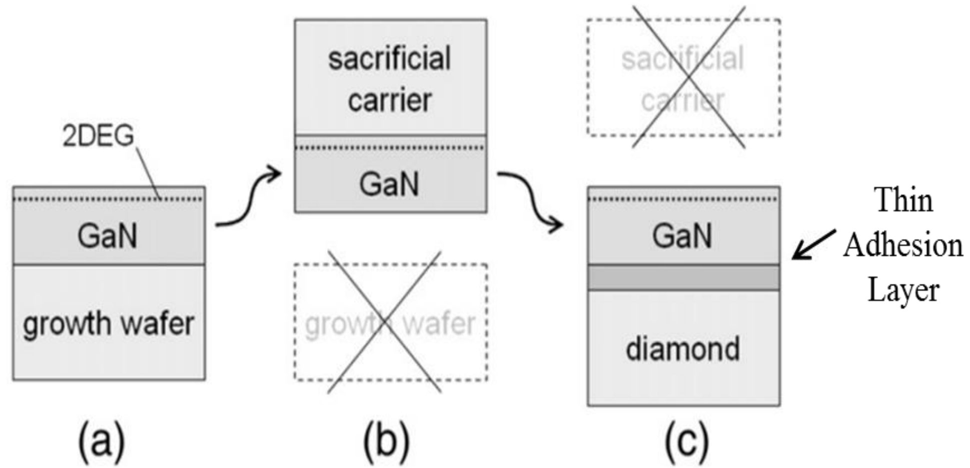

Figure 12: GaN-on-diamond HEMT Device process flow following “double flip” process [41]

The second method is similar to the first method in that it requires a sacrificial carrier, but it differs in that the thick (>100µm) polycrystalline CVD diamond is grown on the inverted GaN buffer layer in step C versus bonding the diamond. This method will be the focus of this study due to the ability to reduce the TBR between the diamond and the substrate. Epitaxy of transistor grade GaN directly onto diamond has yet to be proven feasible [28].

1.2.4 Issues with Diamond Implementation

Although diamond has many characteristics that make it an attractive substitute as a substrate material for aggressive thermal management, diamond has a lattice mismatch and CTE mismatch with GaN which make growth of GaN on diamond difficult, even with a buffer layer [24].

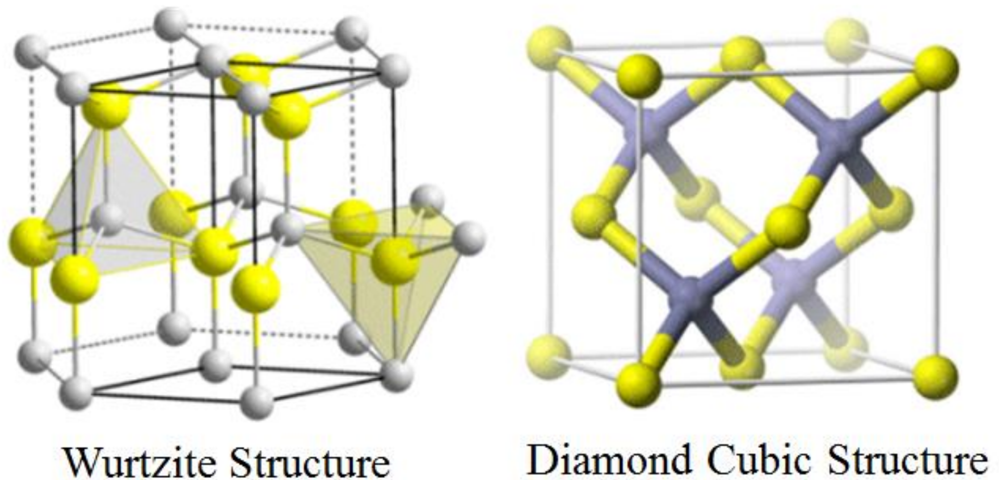

Figure 13: Wurtzite crystal structure is in GaN, (Aluminum Nitride) AlN, and AlGaN while diamond has a cubic structure [42].

GaN, AlN, and AlGaN all have the same crystal structure, wurtzite, while diamond has a cubic structure when formed correctly as seen in Figure 13. CVD diamond is also polycrystalline so the lattice mismatch varies along the interface of the diamond. This creates problems in the integration of GaN on diamond and the implementation difficult [43, 44]. In order to prevent cracking at the interface due to the CTE mismatch as well as to electrically isolate the active GaN region, a thin dielectric layer is deposited on the GaN layer in which the nucleation of diamond can begin.

The chemical vapor deposition process for diamond on non-diamond substrates can lead to many defects and impurities at the interface due to many factors including nucleation techniques, methane concentration, hydrogen concentration, and substrate used [29]. These factors will be discussed in chapter two, but the microstructural defects at the interface create small grain boundaries which are more likely to produce areas with defects, impurities, and vacancies leading to an overall lower thermal conductivity and a large thermal boundary resistance between the diamond and substrate.

1.2.4.1 Thermal Boundary Resistance

Thermal boundary resistance (TBR) is used to describe thermal transport across an interface and is the inverse of the thermal boundary conductivity:

$$TBR = \left[\frac{\dot{Q}}{A \cdot \Delta T}\right]^{-1} \tag{1}$$

where $\dot{Q}$ is a heat flow across an interface, A is the area that the heat is passing through, and ΔT is temperature difference between the two sides of the interface. There have been experimental indications that the overall thermal resistance of AlGaN/GaN device structures is largely due to the thermal boundary resistance (TBR) at the interface between GaN layer and the substrate [45]. The effective TBR is associated with interfaces between materials, the dielectric interlayer used for diamond growth seeding, the adhesion layer if used, the high defect density, and small grain transition region near the nucleation surface [46]. The summation of these resistances, as seen in Figure 14, is the effective thermal boundary resistance for the GaN on the diamond interface. Research has shown a large variation in effective TBRs for GaN on diamond from 27 to 50 m^2K/GW [32, 47, 48].

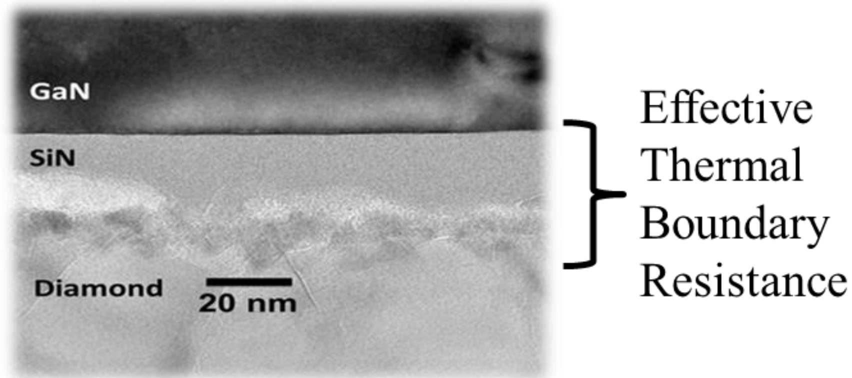

Figure 14: SEM image of GaN on Diamond interface with SiN dielectic layer

As seen in Figure 15, relatively small TBRs can greatly increase the peak junction temperature. Increasing the TBR to 27 m^2K/GW increased peak temperature by over 60°C for this two finger HEMT.

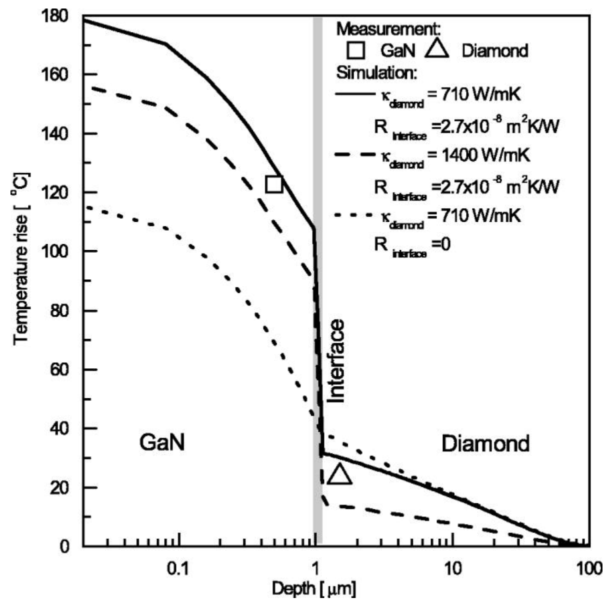

Figure 15: GaN and diamond temperatures measured by Raman thermography on the drain side in a two finger GaN-on-diamond transistor. Increasing the TBR to $27m^2K/GW$ increased peak temperature by over 60°C [49].

Due to similar crystal structures and increased research, the lower limits of the thermal boundary resistance between GaN on silicon and silicon carbide have been shown to be lower than GaN on diamond as seen in Table 3 and Figure 16. New techniques such as thinner adhesion layers and optimization of growth and nucleation techniques as in Table 4 will continue to drive the TBR between GaN on diamond devices lower.

Table 3: GaN-Substrate Thermal Boundary Resistances Summary [48]

	Diamond	Si	SiC	Sapphire
Thermal Boundary Resistance (m^2K/GW)	36-47[32]	33[51]	8-60[53]	120[51]
	27[50]	7-10[52]	4-7[52, 54]	

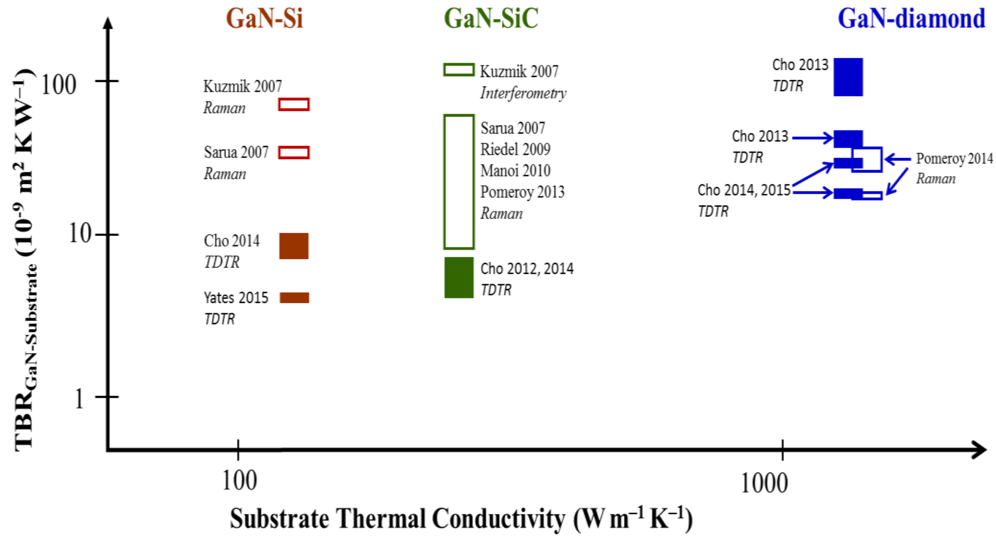

J. Kuzmik *et al.*, J. Appl. Phys., 101 (2007)[55]
A. Sarua *et al.*, IEEE Trans. Electron Dev. ,54 (2007)[51]
G. J. Riedel *et al.*, IEEE EDL, 30 (2009)[56]
A. Manoi *et al.*, IEEE EDL, 31 (2010)[53]
J. Pomeroy et al., IEEE CSICS (2013)[28]
J. Pomeroy et al., Appl. Phys. Lett., 104 (2014)[50]
J. Pomeroy et al., IEEE EDL, 35 (2014)[57]
L. Yates et al., ASME InterPACK (2015)[58]
J. Cho *et al.*, IEEE EDL, 33 (2012)[54]
J. Cho *et al.*, IEEE Trans. CPMT, 3 (2013)[32]
J. Cho *et al.*, Physical Review B, 89 (2014)[52]
J. Cho *et al.*, IEEE CSICS (2014)[59]

Figure 16: Comparison of TBR and substrate thermal conductivity for GaN on Si/SiC/Diamond.

Research has shown a large variation in effective TBRs for GaN-on-diamond from 27 to 50 m^{2}K/GW [32, 47, 48]. This large variation is dependent upon many parameters including nucleation density, intergrain voids, non-diamond carbon in nucleation region, dielectric layer used, and growth techniques in the diamond seen in Table 4.

Table 4: TBRs dependence on growth conditions [46]

	$k_{diamond}$ (W/m-k)	TBR_{eff} (m^{2}K/GW)
34nm seeding Opaque HF diamond	620 ± 50	25 ± 3
100nm seeding Translucent MW Diamond	1500 ± 300	50 ± 5
28nm seeding Translucent MW Diamond	1500 ± 300	12 ± 2

The dielectric layer, usually SiN, creates a large thermal resistance of 5-50 m^2K/GW due to its low thermal conductivity [32]. The dielectric layer thickness is compared to the effective thermal boundary resistance in Figure 17. The amorphous SiN layer has a thermal conductivity of around 1.9 W/m-K. This layer thickness must be reduced in order to minimize the effective TBR between GaN and diamond.

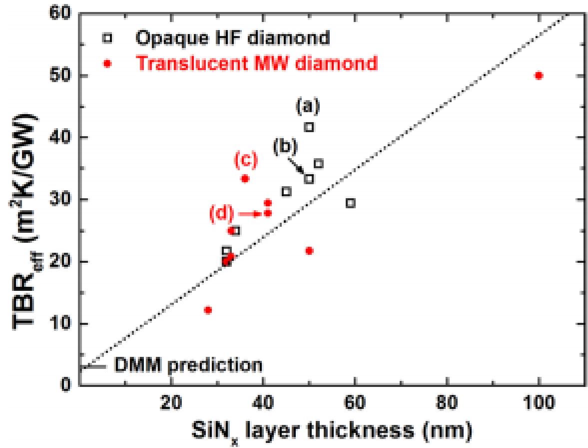

Figure 17: Effective thermal boundary resistance (TBR_{eff}) of GaN-on-diamond wafers as a function of the SiN layer thickness. The thermal conductivity of the amorphous SiN layer is estimated to be 1.9 W/m-K [46].

While diamond as a substrate material is a promising technology due to having a 3-4x increase in the thermal conductivity of SiC, the current leading substrate material in AlGaN/GaN HEMTs, diamonds continued implementation is impeded by the thermal boundary resistance at the interface with the GaN. Figure 18 shows diamond as a substrate material in GaN HEMTs can obtain 30% lower peak temperatures than SiC if the processing is effectively optimized. Poor diamond deposition can lead to a high thermal boundary resistance between the GaN and diamond leading to similar performance as seen with silicon.

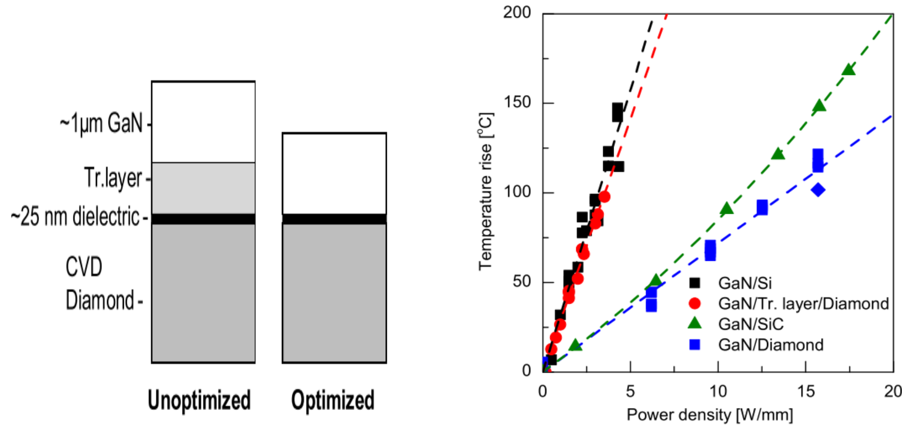

Figure 18:Schematic cross section of GaN-on-diamond showing thermally unoptimized and optimized designs, before and after the removal of the AlGaN transition layer(left) and experimental results of 2 finger 100µm wide AlGaN/GaN HEMT showing varying substrates [28].

1.3 Previous Diamond Programs

Previous studies conducted by Defense Advanced Research Projects Agency (DARPA) have also focused on characterizing the thermal properties of CVD diamonds for implementation in GaN-on-Diamond HEMT devices. Two round robins were conducted to understand the thermal conductivity of thick diamond samples. Two recent DARPA programs, Near Junction Thermal Transport (NJTT) and Intra/Inter Enhanced Cooling (ICECool) program demonstrated through modeling and experiments that a HEMT on diamond substrate could enable a 3x increase in HEMT areal dissipation density without significantly increasing operational temperature as seen in Figure 8 [31]. The methodology in implementation was to grow the AlGaN/GaN epilayers and diamond substrate separately, and then bonding the two layers together including a thin dielectric and adhesion layer using the flip chip method [60]. This method would allow for polishing and abrasion of the first few microns of diamond near the nucleation region, discarding the small grains and low thermal conductivity region. This allowed the

columnar oriented, high thermal conductivity diamond to be as close to the hot spot as possible. This adhesion layer provided for a large thermal boundary resistance between the two layers. This adhesion layer was determined to have a maximum resistance of 40 m^2K/GW [32]. The previous diamond projects measured thick diamond samples, 490-728 µm, with thermal conductivities ranging from 1300-2000 W/m-K. Previous diamond projects used photothermal deflection, heated bar, laser flash, modified Ångström method, and transient grating methods to determine thermal conductivity [60]. These previous groups did not focus on the anisotropy of the diamond and the thermal boundary resistance with the growth substrate.

This work will focus on the method of implementation where the CVD diamond is grown on the GaN epilayers without the use of an adhesion layer. A thin dielectric layer is still necessary to electrically isolate the active region in the GaN and protect the GaN during the diamond deposition process. This diamond growth on GaN process offers great potential in the optimization of nucleation and growth parameters in order to reduce the overall thermal resistance in the interface and first few microns of diamond growth. The combined thermal boundary resistance for GaN on diamond with an adhesion layer has shown to be 70-120 m^2K/GW while direct diamond growth on GaN has a TBR of 20-65 m^2K/GW [32]. This work will focus on the understanding of the thermal properties of diamond in this region (<5µm from the interface). As seen in Figure 19, the first micron of diamond growth contains the smallest grains (<200nm), which significantly hinder the heat flow from the junction to ambient conditions.

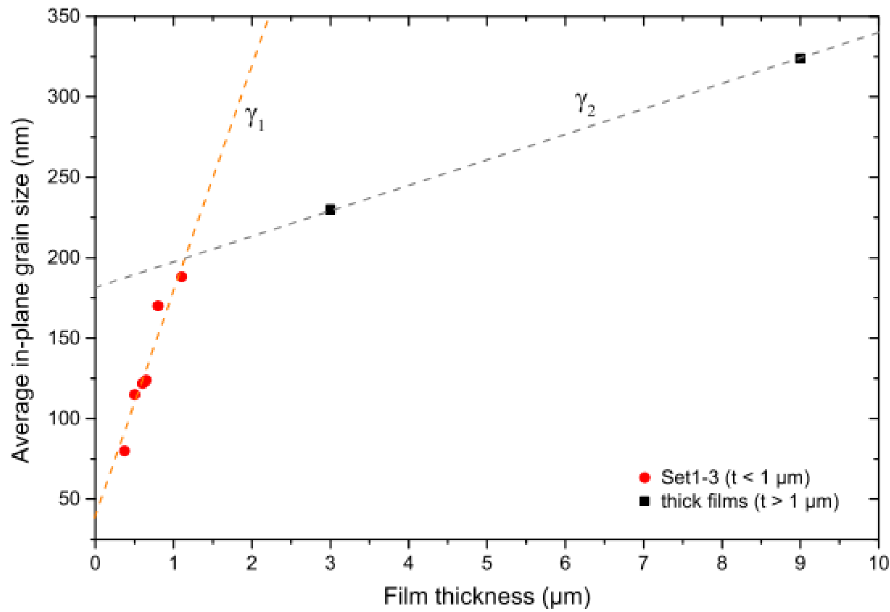

Figure 19: Average in-plane grain size versus film thickness for the columnar-nanocrystalline diamond films. The transition from single crystallites to columnar grains take place in the 1st micron of diamond [35].

1.4 Research Problem Statement and Research Objectives

As discussed in Section 1.2, issues arise due to increased temperatures in AlGaN/GaN HEMTs which can impact its performance and reliability. While diamond is seen as a promising solution to this problem, it is necessary to investigate the thermal conductivity and thermal boundary resistance of diamond near the growth interface of diamond with semiconductor substrates. It is the need to understand these properties and the lack of testing techniques that drive the work of this thesis. In the 2nd chapter, the CVD process will be discussed in detail as well as the diamond samples that will be compared. In the 3rd chapter, several techniques are developed to understand the thermal conductivity of thin nano and micro crystalline diamond films and the thermal boundary resistance with SiC and GaN substrates. A 1.1 µm diamond sample on a silicon substrate

will be compared to various other diamond samples, comparing diamond quality as well as thermal properties. Anisotropic thermal conductivity measurements are made using Raman spectroscopy temperature mapping. In the 4th chapter, quick screening methods based on Raman, FTIR, and XPS are also correlated with the thermal properties of the films. The 5th chapter models a GaN on SiC HEMT and uses the device's temperature profile and geometry to create a thermal model. This model is then used to implement properties found in this work. The properties of CVD diamond films near the interface of semiconductor substrates is revealed for layers less than 5 μm in thickness and their impact or limitations on thermal management are shown through simulations.

CHAPTER 2: CHEMICAL VAPOR DEPOSITION DIAMOND

2.1 Introduction

The implementation of CVD diamond as a substrate material promises to increase the power and frequency of AlGaN/GaN HEMTs through further development and optimization. The CVD process has many input parameters that affect the overall microstructure of the diamond. The microstructure of the diamond determines the overall mechanical properties of the material including the thermal properties. The optimization of the CVD technique will improve the thermal properties of the diamond, including the anisotropic thermal conductivity and the thermal boundary resistance between the diamond and GaN.

The process of chemical vapor deposition utilizes a gas phase chemical reaction occurring above the surface material, where deposition occurs. There are many types of CVD diamond deposition processes, but they all include a means of activating gas phase carbon-containing precursor molecules. This activation involves thermal methods such as hot filament, and electric discharge methods including DC, RF or microwave, and combustion flame [26]. These methods will be discussed in greater detail in the following section.

The ultimate goal of the CVD diamond process is to deposit high quality polycrystalline diamond films. The term quality in this context refers to the ratio of sp^3(diamond) to sp^2-bonded (graphite) carbon in the sample, the composition (e.g. C-C versus C-H bond content) and the crystallinity [25]. The varied CVD processes can

deposit diamond at varied rates, the fastest being up to 1000 μm/hr while the slower methods deposit at 0.1μm/hr. The quicker methods lead to an overall poorer quality diamond inherently affecting the thermal properties. The overall challenge is increasing the growth rates to economically viable rates (100μm/hr) without compromising film quality.

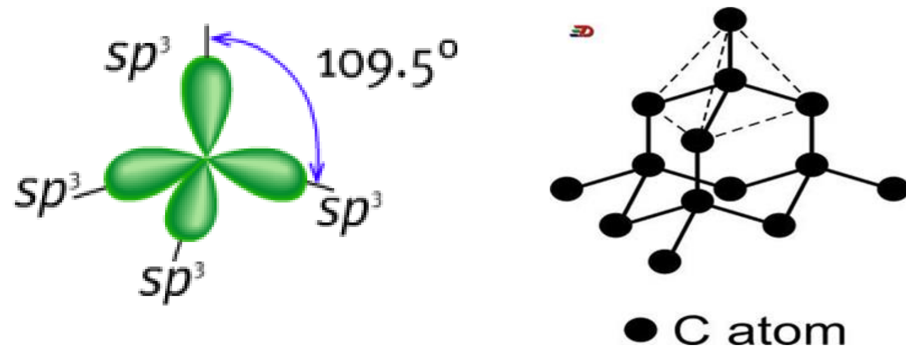

Figure 20:sp^3-hybrid orbital(left) and diamond crystal structure (right) [61]

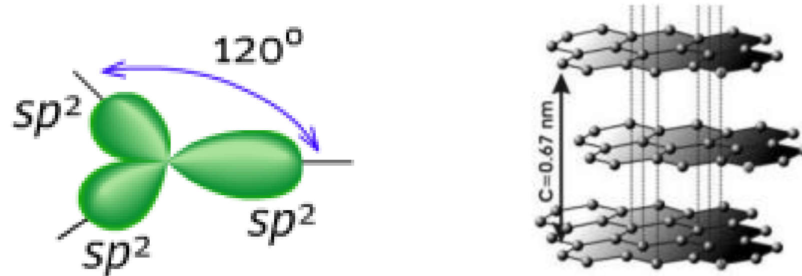

Figure 21: sp^2-hybrid orbital (left) and graphite crystal structure (right) [61]

As seen in Figure 20 and Figure 21, the different hyrbritization of carbon include sp^{3}and sp^2. sp^3 hyrbidization coorelates to the diamond structure that is found in natural single crystal diamond. This tetraheadrol formation packs the carbon atoms together closely with four strong covalent bonds. These strong bonds create a uniform formation of a 3-dimensional network of carbon-carbon (C-C) single (sigma) bonds. The sp^2

hybridized carbon atoms form a two-dimensional sigma and pi bond network to create sheets of graphite. While these sheets of graphite have strong bonds in-plane, their out of plane bonds are much weaker. These weak bonds between sheets greatly reduce the overall thermal conductivity of graphite. The greater the ratio of sp^3/sp^2 bonds is, the higher the thermal conductivity of the material.

2.2 The CVD Process

2.2.1 Nucleation

Nucleation of diamond is the crucial first step in the CVD process. This critical first step is essential for optimizing the diamond properties such as grain size, and orientation that are necessary for reduced thermal resistance [62]. CVD diamond began by using single crystal diamond as the substrate, and later developments allowed for non-diamond substrates by utilizing diamond seeds on the surface. In 1987 Mitsuda *et al.* [63] found that scratching of the substrate surface with diamond powder could greatly enhance the nucleation density. Since then, substrate scratching has become the most common method for achieving nucleation that can form diamond with a high nucleation density and fine uniform grain size [62]. Different nucleation densities greatly affect thermal conductance at the interface. Too low of a nucleation density can create air voids at the interface, while overly high nucleation densities can create extremely small grains near the nucleation region that do not allow for coalescing into the high quality columnar grain structure that is desired. The most common methods for today's nucleation include: mechanical abrasion, by scratching the surface substrate with diamond powder, bias enhanced nucleation, by applying a negative substrate bias voltage, and ultrasonic polishing [62, 64, 65].

2.2.2 CVD Growth

The CVD process begins by mixing the gases, usually hydrogen (H_2) with a small percentage of methane (CH_4) in the chamber before diffusing to the surface. The gasses pass through an activation region that provides energy to the gases, which cause the molecules to fragment into reactive radicals and atoms. These reactive fragments shown in Figure 22 then strike the substrate and can either 1) absorb and react with the surface, 2) desorb back into the gas phase, or 3) diffuse close to the surface until a reaction site is found which is depicted in Figure 22.

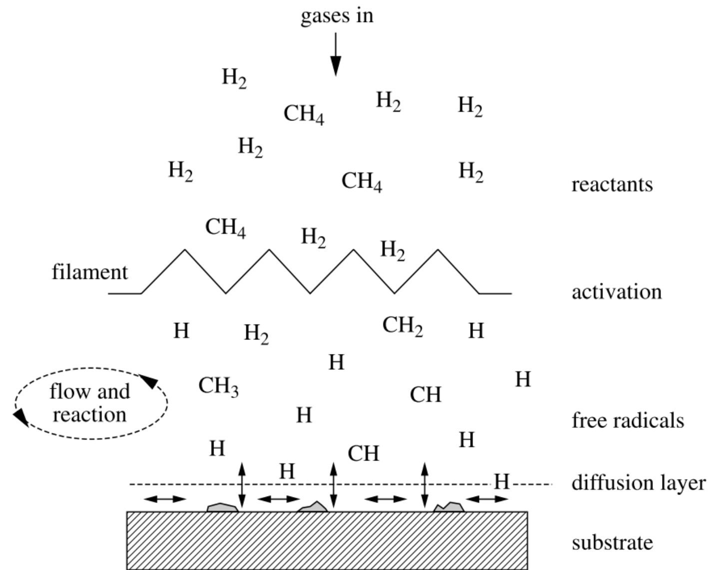

Figure 22: Schematic of the physical and chemical process occurring during diamond CVD [26]

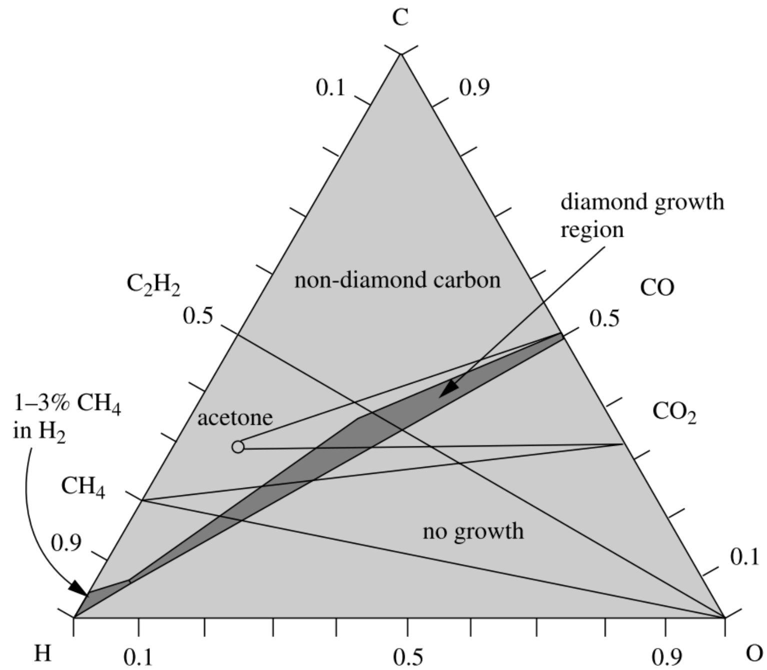

Figure 23: A simplified Bachmann triangle C-H-O composition diagram. The formation of sp^3 bonds requires highly specific carbon to hydrogen to oxygen ratios [26].

The chemical composition of the gasses in the CVD process must be precise, as there is a narrow window for diamond formation as is seen in the shaded portion of the Bachmann triangle in Figure 23.

After the nucleation process, the growth process can begin saturating the surface with hydrogen. Atomic H abstracts a surface H to form H_2, leaving behind a reactive surface site. The site will most likely react with a nearby H atom, returning to the original situation. However, a CH_3 radical may react with the surface site, which adds a carbon atom to the lattice. This process, as pictured in Figure 24, occurs continuously as the diamond growth continues. This is a stepwise addition of carbon atoms to the already existing diamond lattice, catalyzed by the presence of excess atomic H [25, 26].

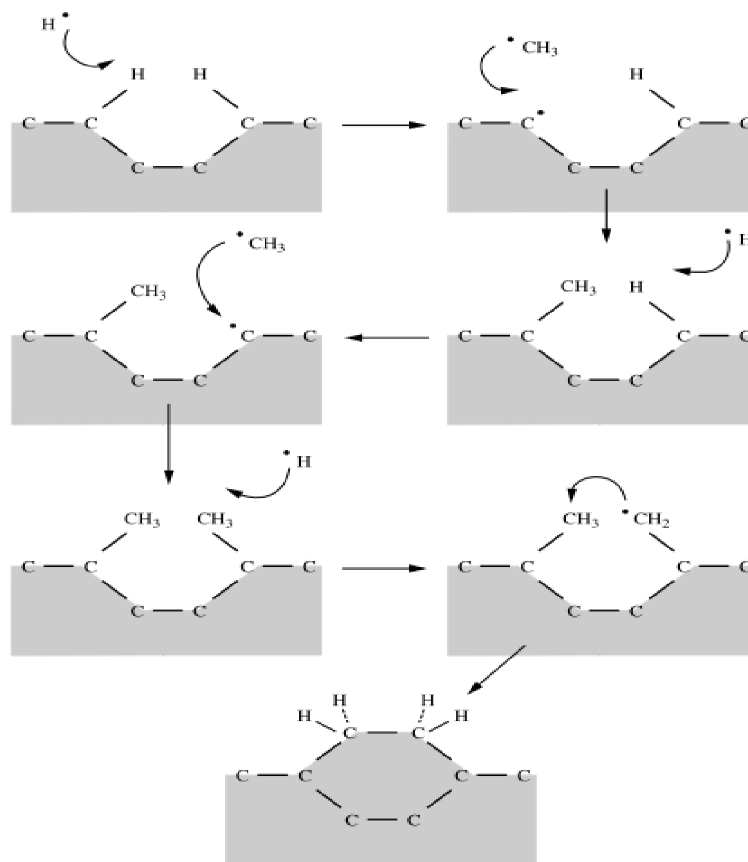

Figure 24: Schematic of the reaction process occurring at the diamond surface. This creates a stepwise addition of CH_3 species and diamond growth [25, 26]

2.1.1 Growth Techniques

In order to obtain the CH_3 radical and singular H atoms, an activation energy source must be present; this is what differentiates the growth methods. The most common method is the microwave plasma CVD (MWCVD) pictured in Figure 25 . Microwave power is coupled into the chamber through a dielectric window to create a discharge. The microwaves couple energy into gas phase electrons, allowing heating and dissociation of the gas molecules, the formation of active species, and then diamond deposition. Hot filament CVD (HFCVD) is seen in Figure 25 (a) where the substrate is beneath the heater, usually tungsten, which is electrically heated in excess of 2200°C.

This takes places in a vacuum chamber, where process gases are metered in at a controlled rate. HFCVD is much cheaper than other methods, but does not produce the same quality as MWCVD, due to contamination that occurs in the diamond film due to the filament material.

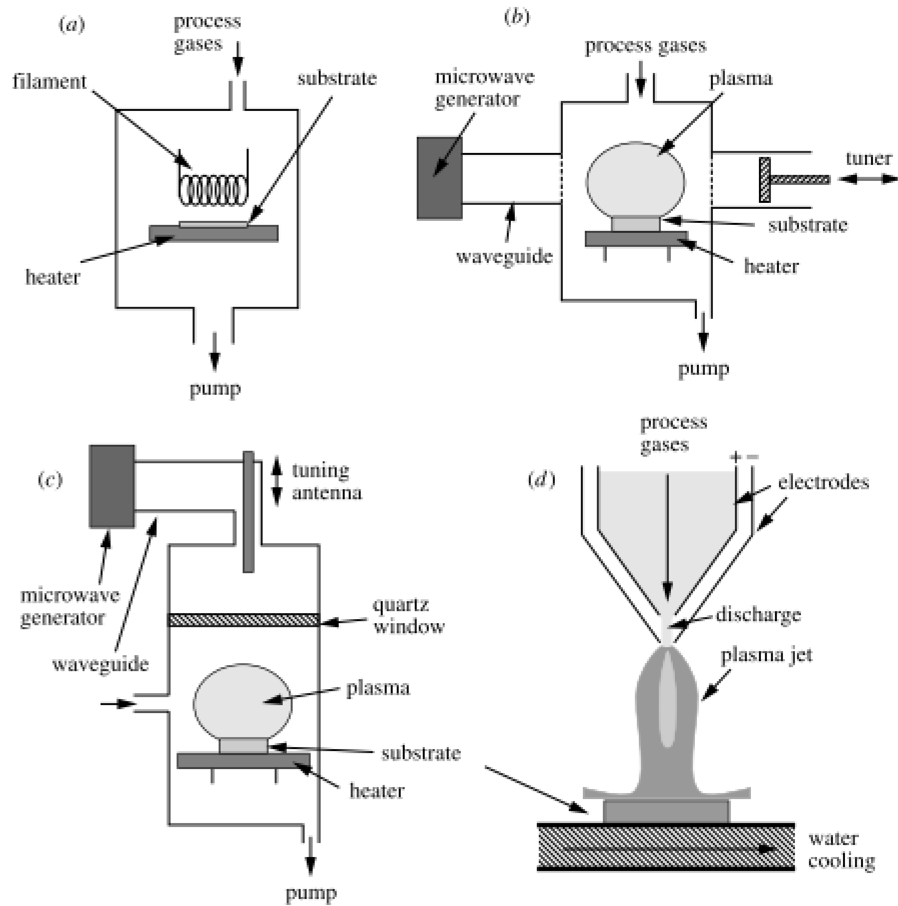

Figure 25: Examples of the most common types of CVD reactors. (a) Hot filament (b)'NIRIM-type' Microwave Plasma (c) 'ASTEX-type' microwave plasma (d) DC arc jet (plasma torch) [26]

Each method of nucleation and growth process can be combined and finely tuned to meet the specific needs of the diamond material and its intended use. This ongoing area of research is key to unlocking the full potential of CVD diamond as an effective thermal management tool.

2.3 Diamond Samples

The CVD diamond samples used in this study were received from various diamond manufacturers with various thicknesses, diamond quality, and growth methods. Table 5 provides a description of the samples that will be compared in this work. These samples include a natural bulk diamond, thin diamond samples grown on a silicon substrate, and bulk CVD samples without a substrate ranging in thickness from 389μm to 534μm. All properties in Table 5 were provided via the manufacturer. These samples were compared based on their thermal properties.

Table 5: Diamond samples tested for thermal properties

Sample Name	Diamond Thickness (μm)	$k_{effective}$ (W/m-K)
Diamond Anvil	-	2000[26]
Sample A	1.1	-
Sample B	1.0	-
Bulk Sample A	511	2137
Bulk Sample B	352	1927
Bulk Sample C	449	1519
Bulk Sample D	389	1284
Bulk Sample E	534	714
Bulk Sample F	525	695

The diamond anvil was a small bulk diamond sample that was obtained from Texas State University. This sample represents the highest quality of diamond available so it will be used as a reference to compare various other sample's quality. This sample can be seen in Figure 26.

Figure 26: Diamond Anvil sample sent from Texas State University

Sample A and Sample B are both a thin layer of CVD grown diamond on a silicon substrate from a 3” wafer. Sample A was grown using a high content of carbon carrying gases in the deposition chamber, where Sample B used a lower carbon content for growth. These samples were fabricated in a laboratory specifically for thermal conductivity measurements. Using the same wafer, various test structures for in-plane and cross-plane thermal conductivity as well as thermal boundary resistance were created. These samples also have specific designs for Raman thermography, Time Domain Thermoreflectance (TDTR), Electrical Resistivity and 3-omega measurements. Samples of 1 cm^2 were fabircated based on the diagram in Figure 27. These samples were sent to collaborators at other institutions which included Stanford University (Prof. Ken Goodson), University of Bristol (Prof. Martin Kuball), and Texas State University (Prof. Mark Holtz) to compare measurement techniques as well as sample spatial variation. Materials were also sent to UCLA (Prof. Mark Goorsky) for microstructural characterization.

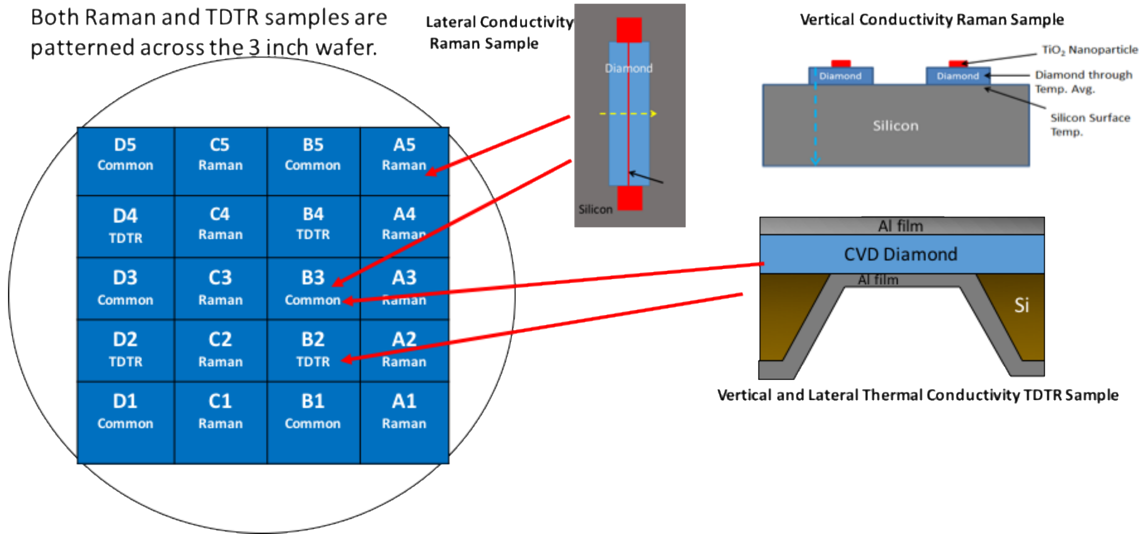

Figure 27: Diagram of the various 1cm^2 die that were fabricated on a 3 inch CVD diamond on Si wafer for both Raman thermography and TDTR measurement of thermal conductivity. Each die from the wafer was 1 cm x 1 cm in size. Samples labeled “common” contained both TDTR and Raman samples in close proximity on the same die in order to make comparisons between the techniques without being impacted by material variation across the wafer. Materials characterization was performed by collaborators at UCLA on die taken from the wafer after thermal conductivity testing was completed.

Devices were fabricated on both Samples A and B for measurements using Raman thermograpy. More information on the geometry of these samples will be discusssed in Chapter 3. Samples were also fabricated that allowed for comparison of thermal properties in the same region through the design of the common samples which allowed for TDTR and Raman thermography measurements within 1.2mm to reduce spatial variations in the microstructre as seen in Figure 28 . Processing conditions were not obtained from the laboratories where the diamond samples were grown due to a proprietary processes for their CVD diamond growth.

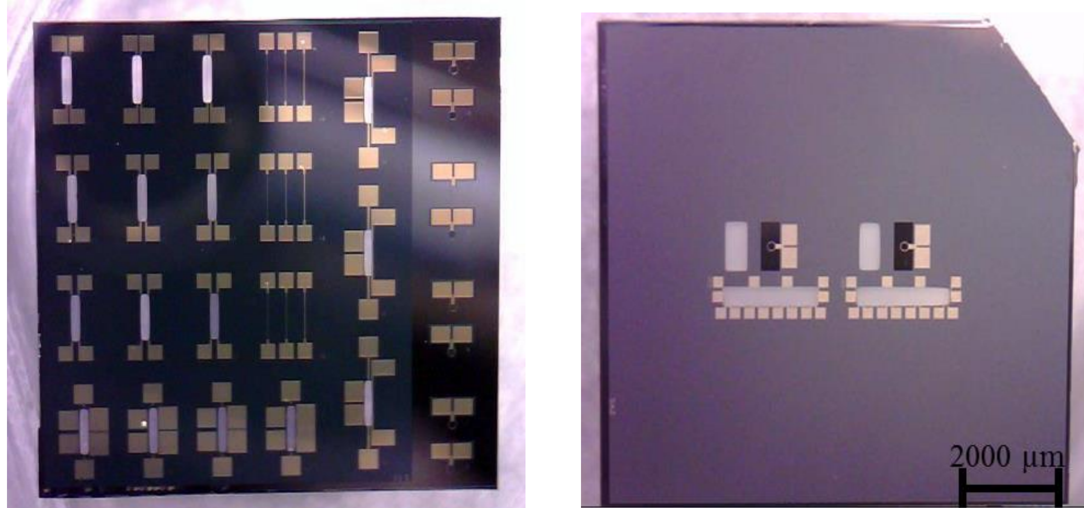

Figure 28: (left) Sample B design for Raman thermography to measure in-plane and cross-plane thermal conductivity. (Right) Common sample to measure thermal properties using TDTR and Raman thermography within 1.2mm of each other.

Bulk samples were also used in this study to compare thermal properties based on thickness. These bulk samples are free-standing polycrystalline diamond substrates that were diced to be 13x13mm with a thickness of approximately 0.5mm. The thermal conductivities reported in Table 5 represent measurements at room temperature. Samples E and F have a low thermal conductivity due to heavy boron doping. Bulk Sample B and Bulk Sample E can be seen in Figure 29.

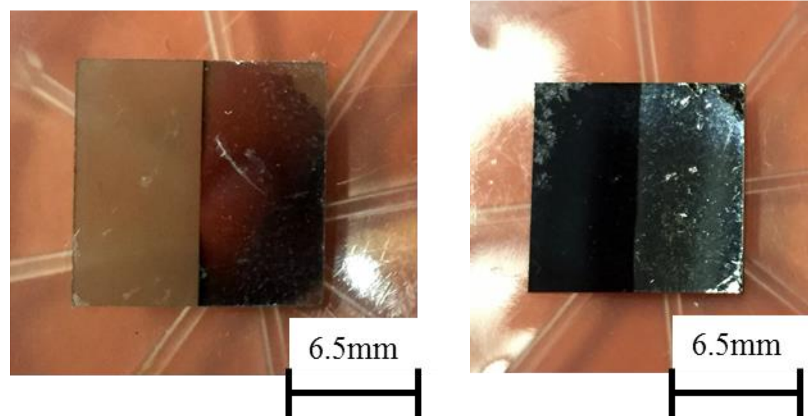

Figure 29: (left) Bulk Sample B shows a transparent thick diamond sample with a high thermal conductivity (1927 W/m-K), and (right) Bulk sample E shows an opaque thick diamond sample with a lower thermal conductivity (714 W/m-K).

2.3.1 Issues in Fabrication

Other samples were received from various laboratories that were fabricated using a CVD process and diced in the dimensions seen in Figure 27. Raman measurements were not able to be conducted on some samples due to poor fabrication that resulted in large defects or high surface roughness. These defects created irregular heating in the samples or proved the samples inoperable as they were not able to hold an electrical current. With a 100nm of Ti/Au heaters deposited on the diamond surface, any surface roughness higher than 30nm RMS did not allow for even heat dissipation throughout the line heaters as the rough surface caused large variations in heater thickness or noncontinuous heaters. Images for these samples are seen in Figure 30.

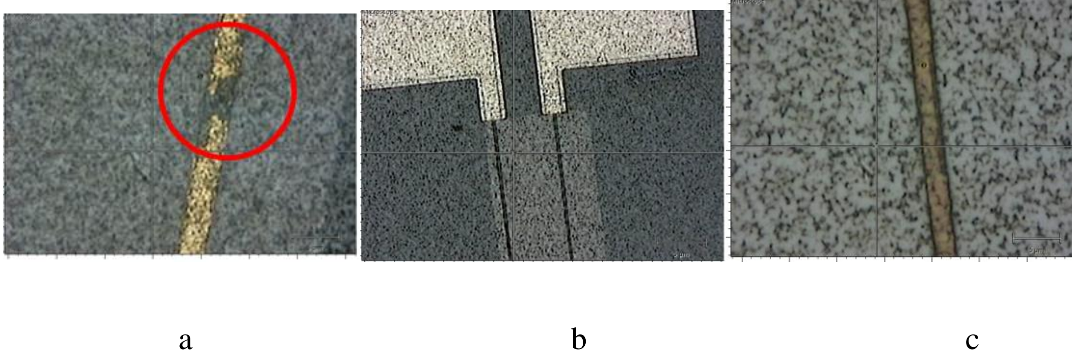

a b c

Figure 30: 5x magnification of fabrication issues due to high surface roughness in the samples. (a) non continuous heaters did not allow for heat dissipation through the heater. (b) and (c) show samples with high surface roughness that did not dissipate heat uniformly. Samples with 30nm RMS or greater surface roughness were not able to be measured.

High surface roughness made the devices inoperable; this could be fixed by ensuring all diamond samples had a surface roughness below 30nm RMS. This could be accomplished by polishing the top surface of the diamond. Issues with silicon etching also arose as the specified dimensions in which the silicon was supposed to be etched was reduced as seen in Figure 31. The dotted red line represents the area that was supposed to etched whereas the dark background refers to the actual areas of etching. This proved troublesome when fitting to an analytical model for one dimensional heat transfer. In order to compensate for these etching issues, a finite element model representing the actual dimensions had to be used to determine more accurately the thermal properties of diamond.

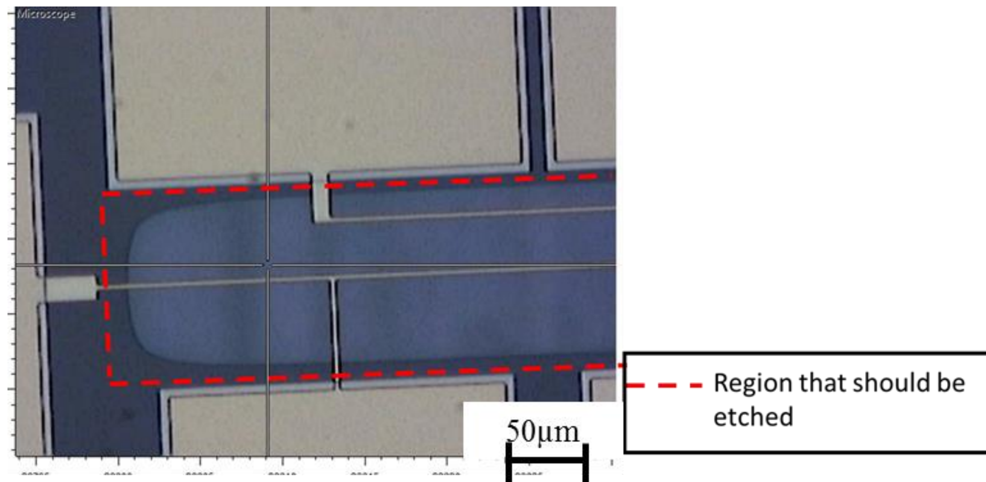

Figure 31: Sample showing silicon etching was not performed to the specifications of the mask.

2.4 Summary and Conclusions

The CVD process has many input parameters that affect the overall microstructure of the diamond. The microstructure of the diamond determines the overall mechanical properties of the material including the thermal properties. The optimization of the CVD technique will improve the thermal properties of the diamond. The nucleation techniques, nucleation density, reactant gases, and growth techniques affect the thermal properties of the diamond thin films. Hot filament techniques allow for faster diamond growth, but with the consequence of worse quality. Microwave plasma CVD allow for higher quality but must be deposited at a slower rates which can increase costs.

Various diamond samples will be studied in this work as natural diamond is compared to free standing bulk samples and thin diamond samples grown on silicon substrates. These thin diamond samples have fabricated structures for measurements by Raman thermography and TDTR. These structures were designed to deduce the

diamond’s anisotropic thermal conductivity and thermal boundary resistance between the diamond and the substrate.

CHAPTER 3: THERMAL PROPERTIES OF DIAMOND

3.1 Introduction

Thermal conductivities of CVD diamond films have experimentally been determined to be as high as 2000 W/m-K [28]. While this does hold promise for the future of GaN-on-diamond technology, a significant portion of the thermal resistance occurs at the interface between the GaN and the diamond within the first 1 μm of diamond growth due to the small grains and defects. This work is primarily focused on the first five microns to better understand how to reduce this region's overall thermal resistance.

In order to accurately measure these properties of diamond, Raman thermography was used due to its high spatial resolution. Raman thermography can perform noncontact thermal measurements, that is not obtrusive to the electrical operations while having a spatial resolution of ~1μm [66]. Raman thermography is able to measure the temperature distributions in a powered structure, either self-heating in AlGaN/GaN HEMTs or resistance heating in substrate materials. Raman has attracted much attention due to its ability to examine devices that are operating without interference in electrical performance with the use of sub-band gap visible lasers. Through the use of Raman spectroscopy, the thermal properties of diamond substrates can be measured.

The goal of determining thermal conductivity in both the lateral and vertical direction as well as the TBR was accomplished using the following strategy: designing diamond structures that attempted to isolate heat flow in a specific direction, determine a

temperature detection technique with small spatial resolution, and comparing temperature profiles to thermal simulations to extract out thermal properties.

3.2 Device Structure

In order to isolate the heat flow in either the lateral or vertical direction, specific test structures were created with the collaboration of the Naval Research Laboratory (Dr. Karl Hobart). To determine $k_{lateral,}$ thin film structures were designed and fabricated as seen in Figure 32. The silicon below the diamond was etched away with gold heaters deposited on top of the diamond sample. This structure will be referred to as a membrane structure. These structures used a thin diamond film of 1.1 µm thick grown on silicon substrates with a thickness of 500µm. Gold resistance heaters were fabricated in the center of the membrane with a titanium adhesion layer between the gold and diamond film. The silicon was then dry etched from the backside using the diamond as an etch-stop layer. The metal heater in the center constrains the heat flow in the lateral direction, with minimal vertical heat spreading.

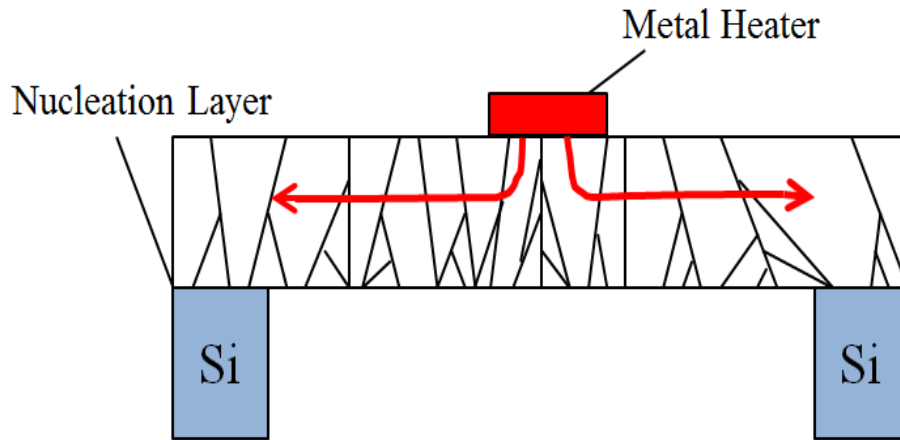

Figure 32: Test structure for lateral thermal conductivity

The dimensions were chosen to allow for calculation of the thermal conductivity assuming one dimensional heat flow through the use of Fourier's Law.

$$k = -q"\frac{\Delta X}{\Delta T} \tag{2}$$

Where q" is the heat flux in W/m^2, ΔX is the change in position and ΔT is the change in temperature. A comparison of the input thermal conductivity of the finite element model to the calculated thermal conductivity from the change in position over the change in temperature as seen in Figure 33 in ANSYS Workbench 16.2 was accomplished, which refers to the normalized thermal conductivity.

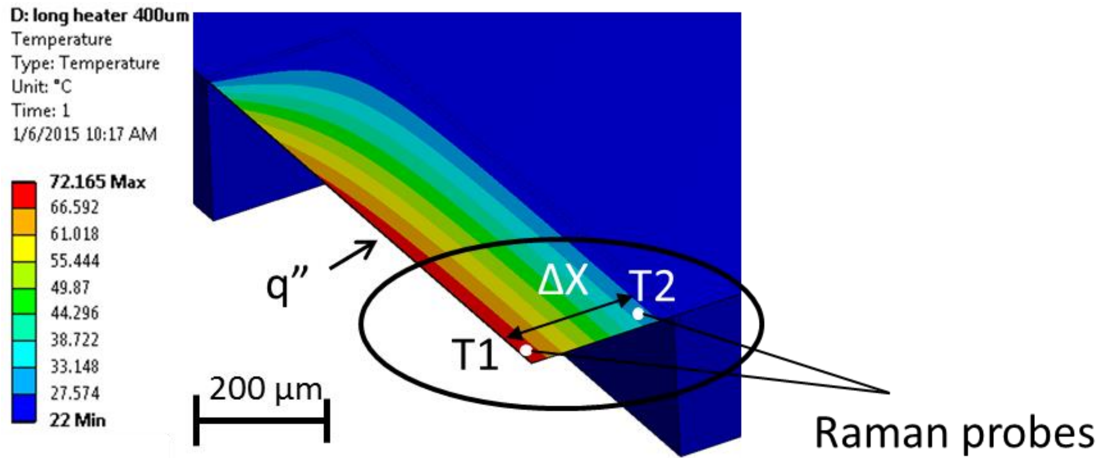

Figure 33: Quarter symmetry FEM of lateral heaters comparing finite element conductivity to calculated thermal conductivity using Fourier's Law.

The dimensions were optimized keeping the length at 1000µm and varying the width from 25µm to 500µm as seen in Figure 34. The maximum normalized thermal conductivity was found with a membrane size of 200µm as seen in Figure 35, so a length to width ratio of 5:1. The final dimensions were 1000µm x 200µm.

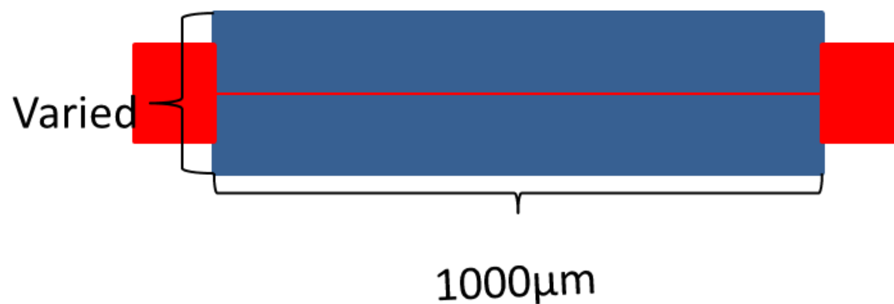

Figure 34: Membrane geometry used to determine optimal length to width ratio

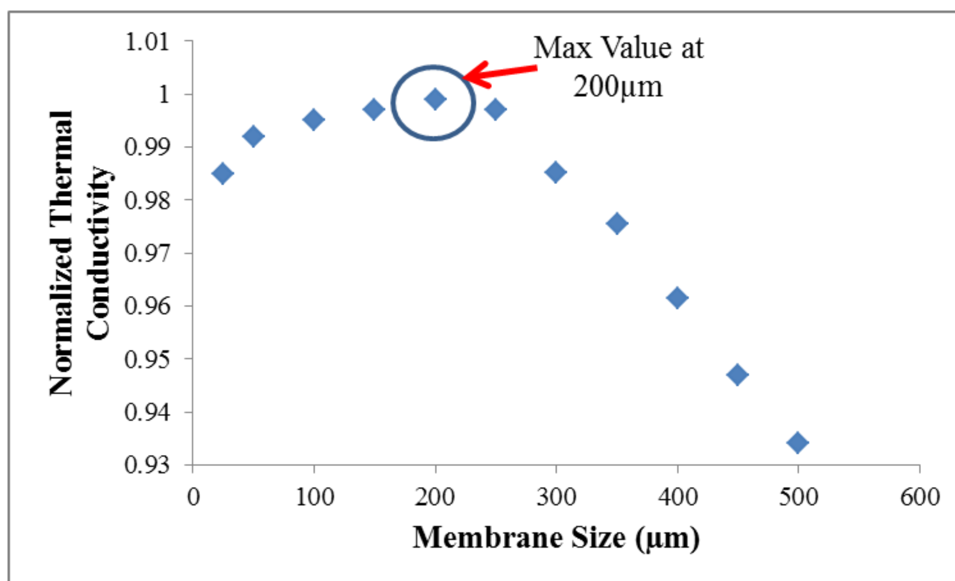

Figure 35: Normalized thermal conductivity compared to membrane size when length is held constant. The maximum occurs at a length to width ratio of 5:1.

The final lateral testing structures utilized the 5:1 ratio and also included metal heaters that could be used for additional resistance measurements as pictured in Figure 36 and Figure 37. A linear change in resistance was observed with increasing temperature. These additional heaters could be used to determine the temperature along these heaters to further validate the temperature gradient along with Raman thermography. Heaters were originally only 100nm thick. High surface roughness on the diamond surface caused non uniform heating and noncontinuous heaters. Diamond samples were required to have 30nm RMS or less of surface roughness for uniform heating. Later samples were fabricated with 200nm of Titanium/ Gold (Ti/Au) heaters.

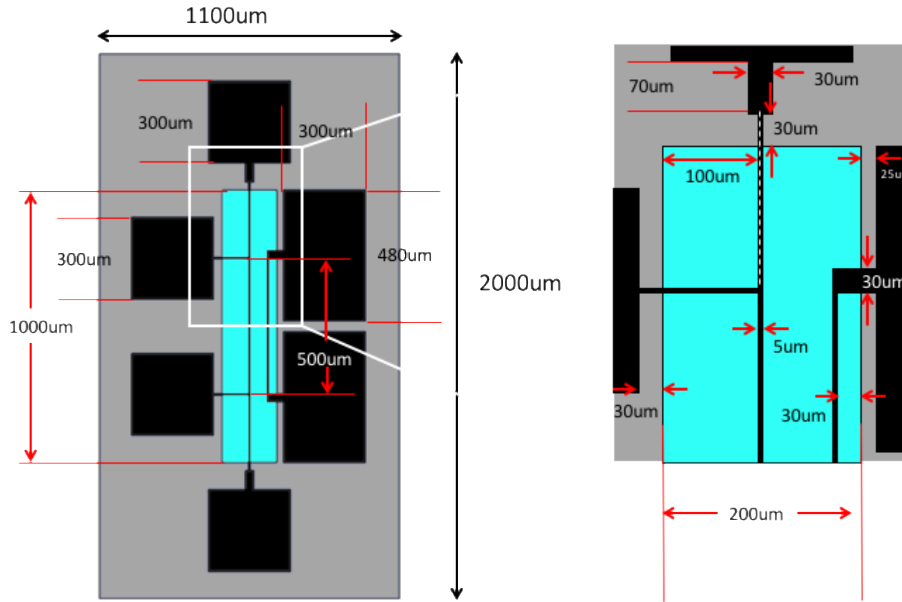

Figure 36: Membrane structure A designed for lateral/ in-plane thermal conductivity measurements.

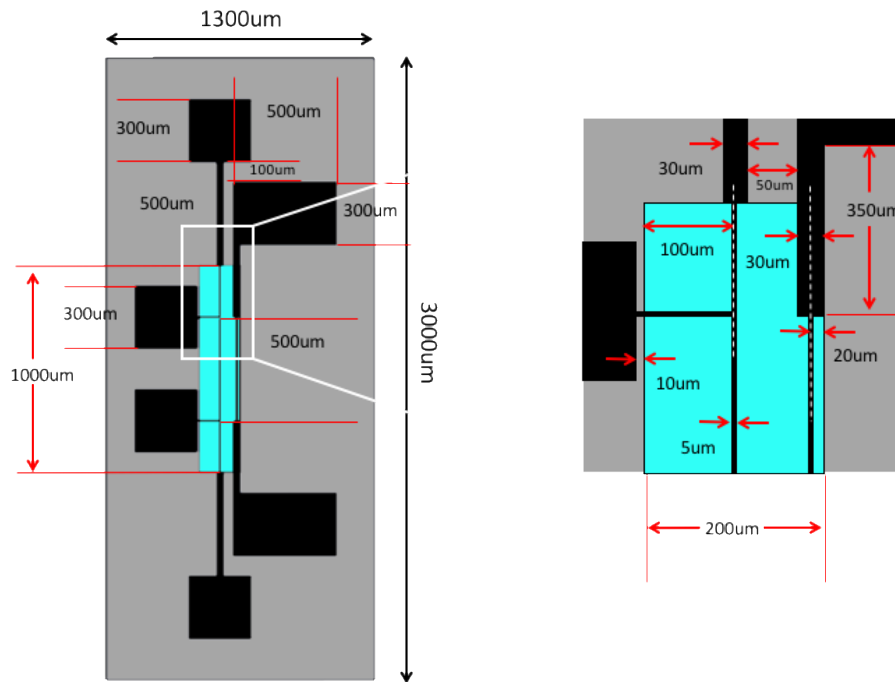

Figure 37: Membrane structure B designed for lateral/ in-plane thermal conductivity measurements.

The vertical or cross-plane thermal conductivity and TBR were determined by attempting to isolate heat flow in the vertical direction using a specifically designed set of

samples as seen in Figure 38. The temperature detection technique chosen for this study, Raman thermography created difficulties in the design of vertical conductivity measurements. Diamond films were again grown on silicon substrates, Ti/Au heaters were applied in mesa or ring like structures as seen in Figure 39. The 10 µm on both sides of the circular heater remained while the rest was etched away. These structures maximized the heat flow along the columnar grain structures, and minimal heat losses due to lateral conduction. Temperature measurements were taken on the surface of heater using a TiO_2 nanoparticle, the through thickness average of the diamond layer and the silicon surface temperature.

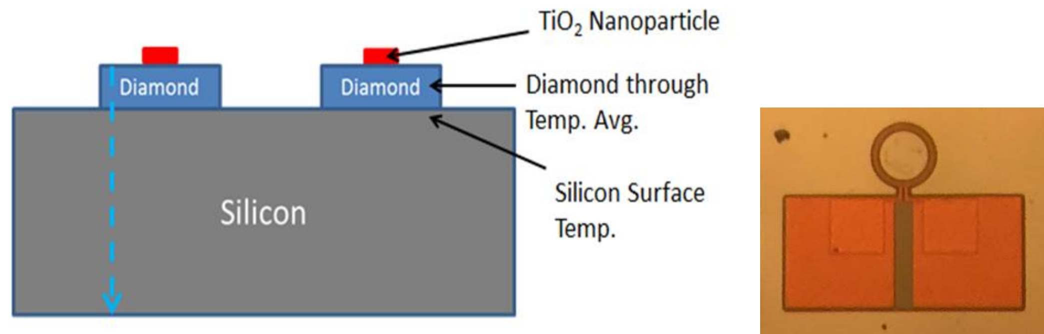

Figure 38: Test structure for vertical thermal conductivity measurements showing the locations of measurements on top of the heater using the nanoparticle, the through thickness average of the diamond, and the silicon surface temperature (left) and a 5x magnification of the actual ring structure (right).

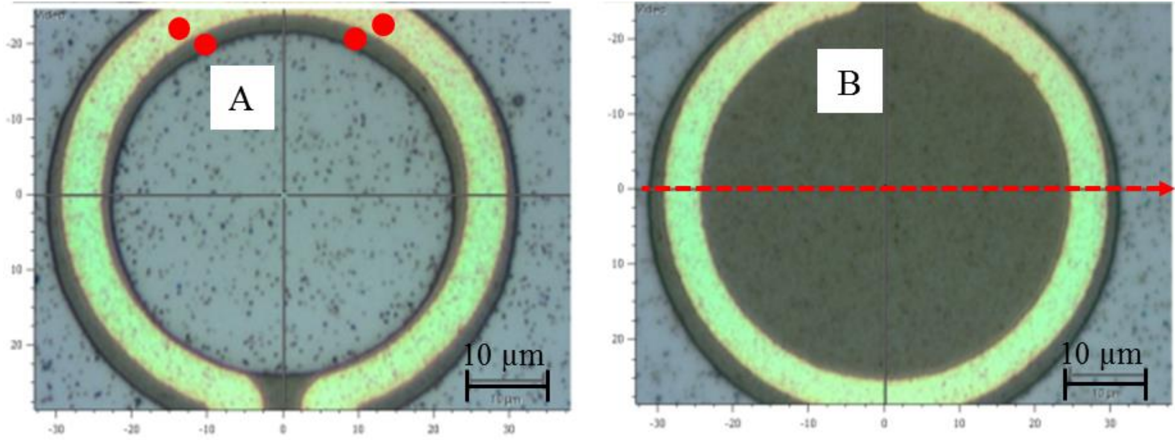

Figure 39: 5x microscope image of diamond ring structures used for vertical thermal conductivity and TBR

Sensitivity analysis of the change in temperature was conducted on the ring structures as seen in Figure 39 using a finite element analysis (FEA) model. This was done by changing the input parameters, diamond on silicon TBR, diamond lateral thermal conductivity, diamond vertical thermal conductivity, and silicon thermal conductivity. The temperature sensitivity analysis was done on the surface of the silicon using the following equation:

$$S(\gamma) = \frac{\delta T(x)}{\delta \gamma} \frac{\gamma}{T(x)} \quad (3)$$

In equation 3, γ is the parameter of interest. By changing each parameter by 10%, the change in temperature was determined through the FEA model and the sensitivity can be determined along the path as seen in Figure 40.

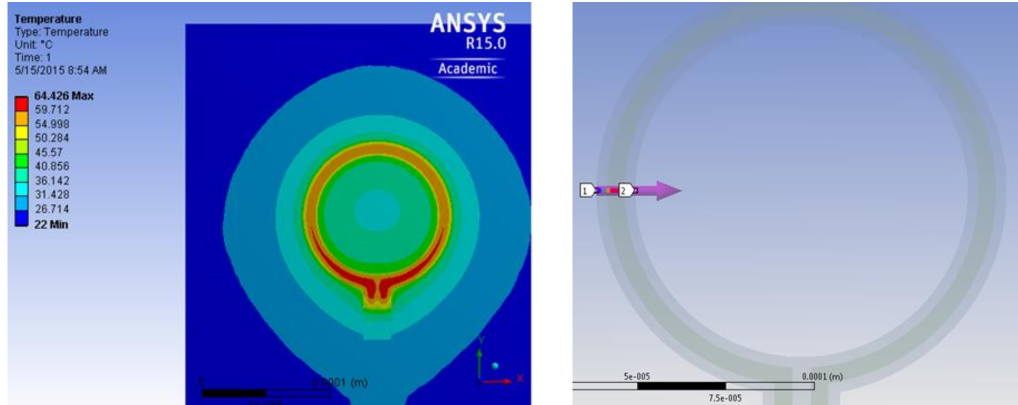

Figure 40: FEA Model with temperature profile (left) and path in which sensitivity analysis was conducted (right).

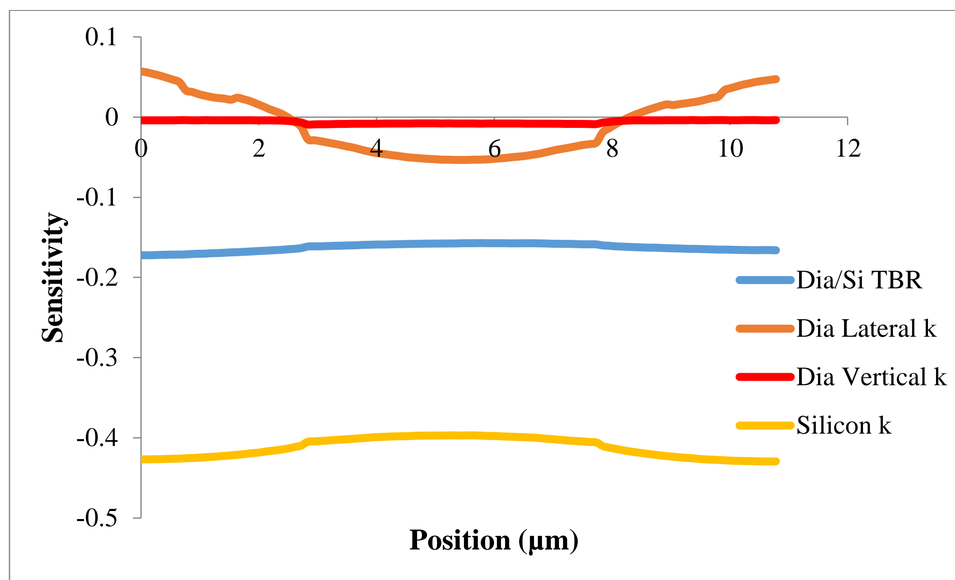

Figure 41: Sensitivity analysis of vertical ring structures along silicon surface.

The temperature in the silicon is sensitive to the diamond/silicon TBR and silicon thermal conductivity as seen in Figure 41. While the lateral and vertical thermal conductivity does not affect the overall change in temperature as much. This graph shows that the vertical ring structures will result in a large uncertainty when obtaining vertical measurements and smaller uncertainty for TBR for diamond on silicon. The final vertical ring structure's dimensions are seen in Figure 42 and Figure 43. The wafer was designed in order to test the spatial variation in the sample as well as to compare

measurement techniques. The wafer layout can be seen in Figure 44 and the individual 1 cm^2 samples for specific measurements can be seen in Figure 45. Common samples were designed and fabricated that included Raman test structures within 1.2mm of TDTR structures to compare measurement techniques while minimizing spatial variations in diamond quality, these designs are seen in Figure 46.

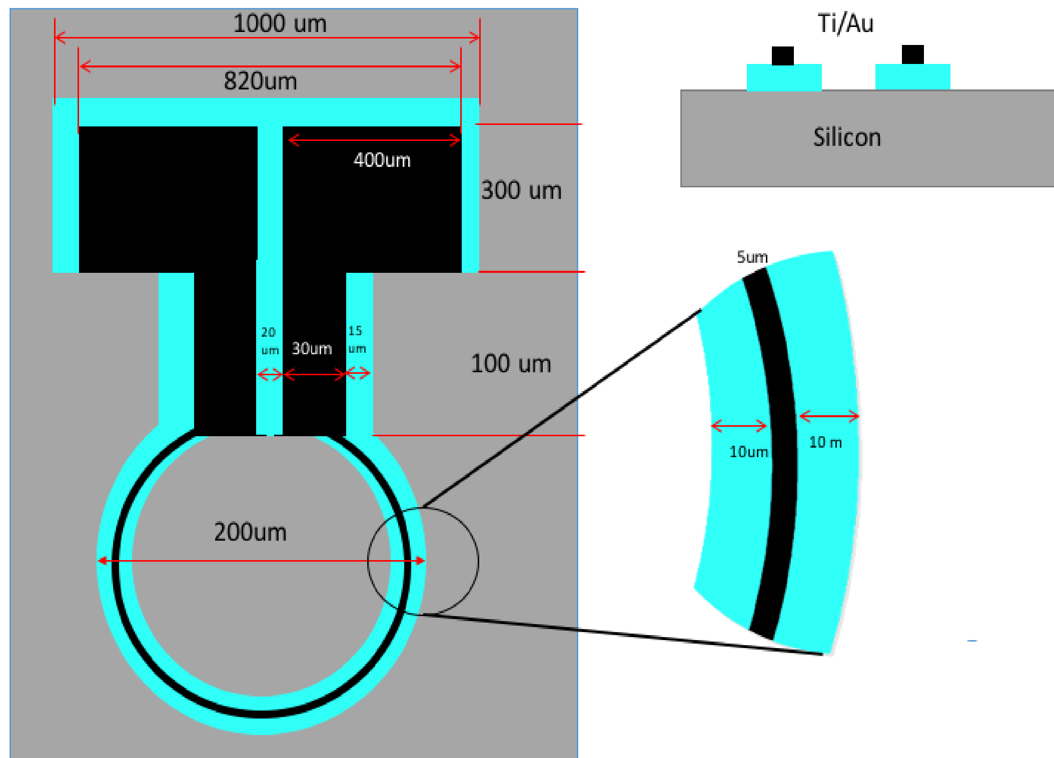

Figure 42: Vertical/ Cross-plane thermal conductivity unfilled ring structures.

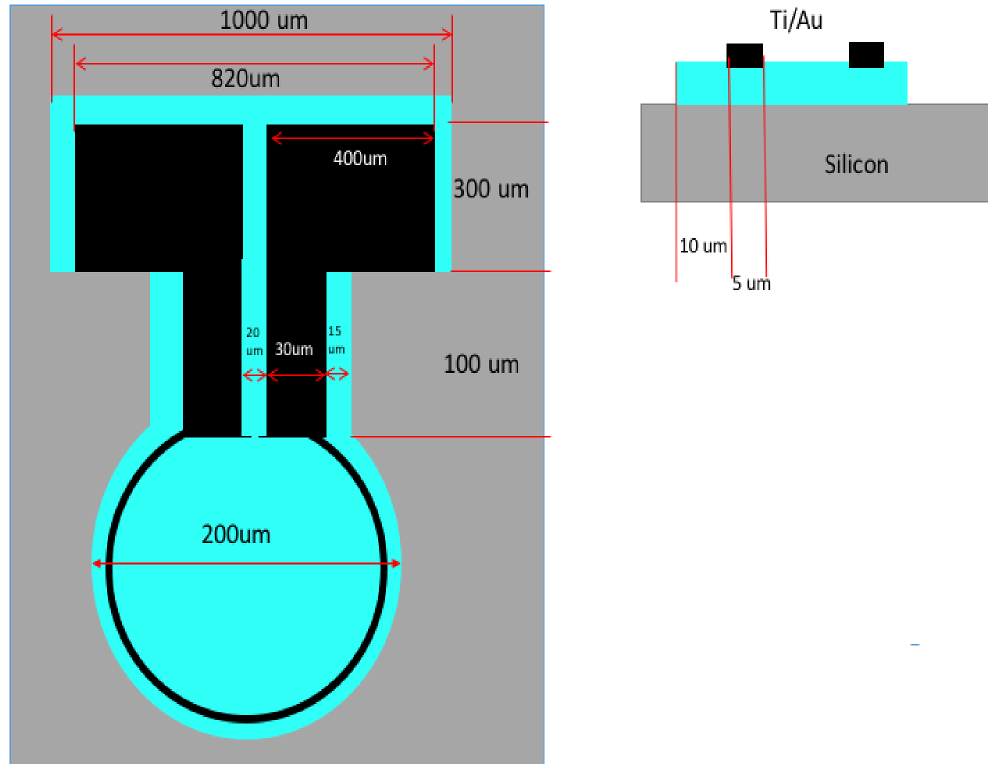

Figure 43: Vertical/ Cross-plane thermal conductivity filled ring structures

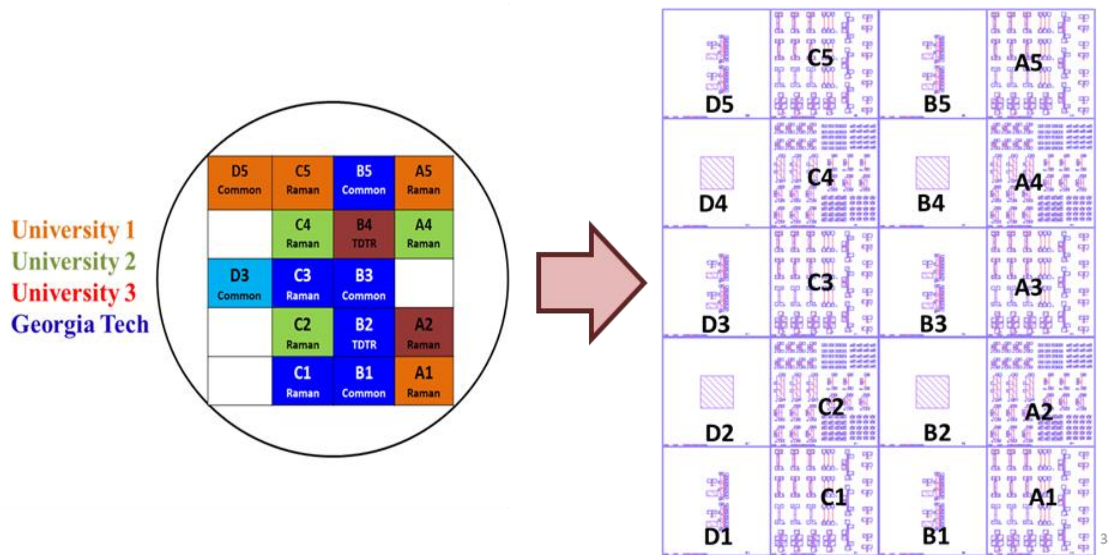

Figure 44: Wafer layout for Round Robin program depicting Raman and TDTR samples.

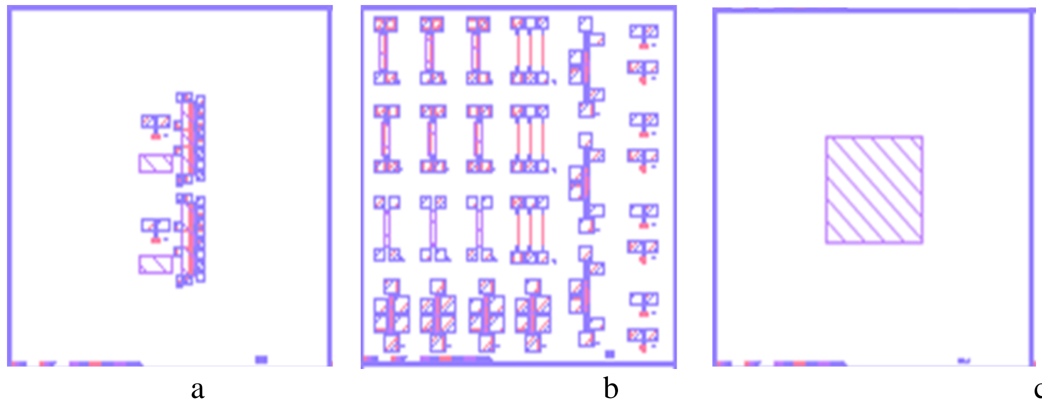

Figure 45: 1 cm^2 samples used in round robin program (a) Common sample for both TDTR and Raman measurements. (b) Raman test structures for lateral and vertical thermal conductivity measurements. (c) TDTR test structures.

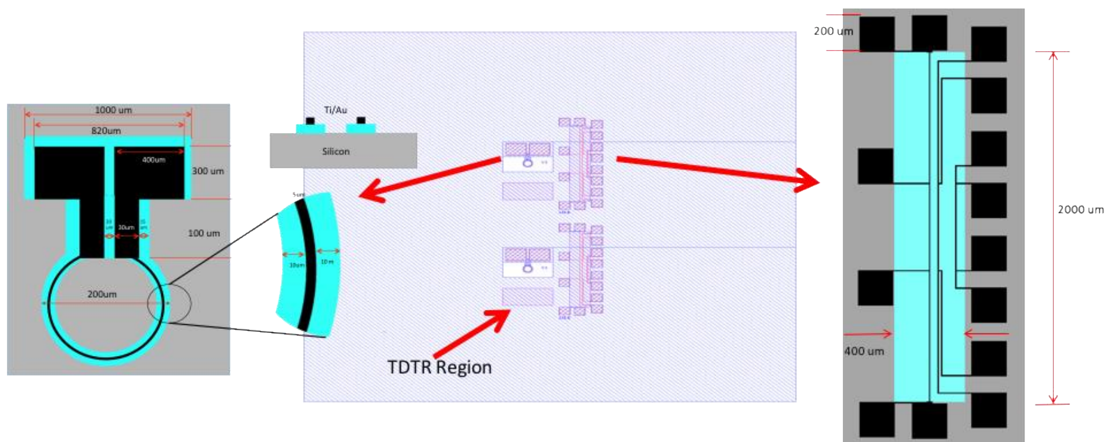

Figure 46: Common samples includes lateral, vertical measurements for Raman thermography as well as TDTR structures to avoid spatial variations in diamond quality.

3.2 Raman Spectroscopy

Raman spectroscopy is an optical scattering technique that is used to probe the vibrational energies of the optical phonons in the material [14]. Raman thermography takes advantage of the inelastic scattering of monochromatic light, usually from a laser. This vibrational energy is transferred either from the incident photon to the molecule (Stokes) or from the molecule to the scattered photon (anti-Stokes). Stokes and anti-Stokes scattering are considered Raman scattering. Micro-Raman spectroscopy measures

phonon frequency of semiconductor materials and is capable of indirectly measuring stress and temperature. The characteristics of the phonons vary with temperature and stress changes. The change in Raman frequencies correlate to the change in temperature/stress states. Figure 47 represents a typical Raman spectrum, when it is heated or under tensile strain, the peaks shift left.

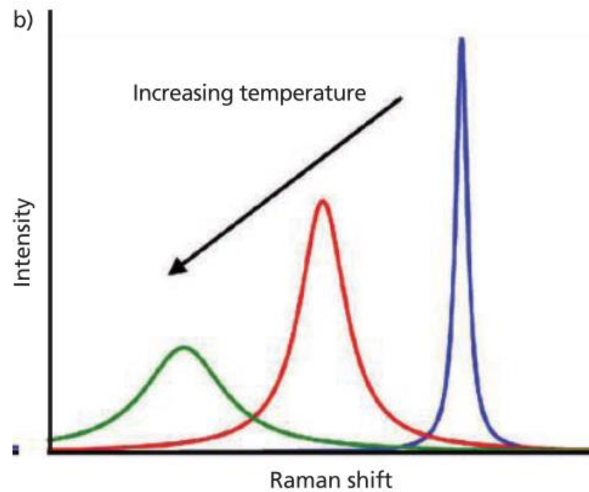

Figure 47: A schematic of a Raman spectrum with peak positions (ω) shifting to the left with increasing temperatures in the material.

3.2.1 Peak Position Method

The peak position of the Raman signal is derived from the energy of the zone-center optical phonons that are probed during the Raman experiment. As the lattice is heated or cooled, the equilibrium of the atoms is changed, which creates an expansion or contraction of the lattice as well as the interatomic forces as a result of the anharmonicity of the bonds [66, 67]. The changes in interatomic forces alter the phonon vibrational frequencies that are shown in the variance of the Raman peak position [8, 66].

3.2.2 Nanoparticles for Surface Measurements

While Raman thermography can provide information for semiconductor material temperature change, this method does not allow for the measurement of metals [68]. Through the use of nanoparticles, specifically Titanium Dioxide (TiO_2) and Zinc Oxide (ZnO), the surface temperature of the heater devices was deduced. This new method uses nanoparticles (<1µm) as small temperature sensors with their own Raman signature as seen in Figure 48. A temperature calibration is determined similarly to that of the substrate material and the devices are powered. These nanoparticles provide accurate, high spatial resolution temperature measurements on surfaces that were not previously able to be measured. These measurements must be conducted at much lower laser powers in order to prevent laser heating of the metal line. The Raman peak for TiO_2 is centered around 144cm^{-1} and is seen in Figure 49.

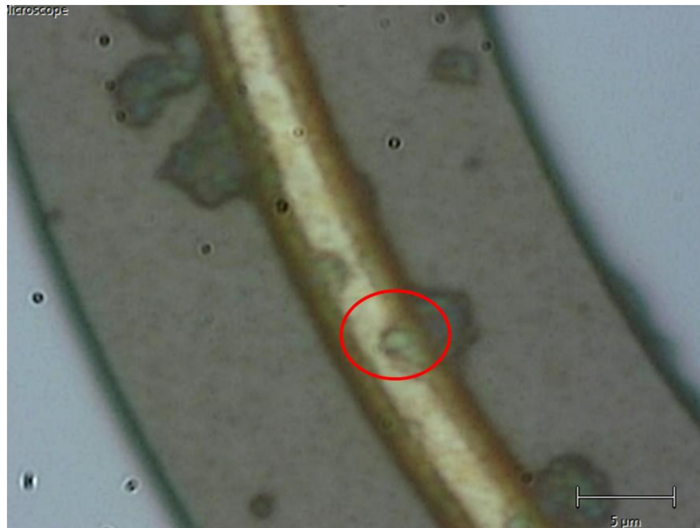

Figure 48: Image of nanoparticles used for surface measurement on heater surface for vertical thermal conductivity measurements

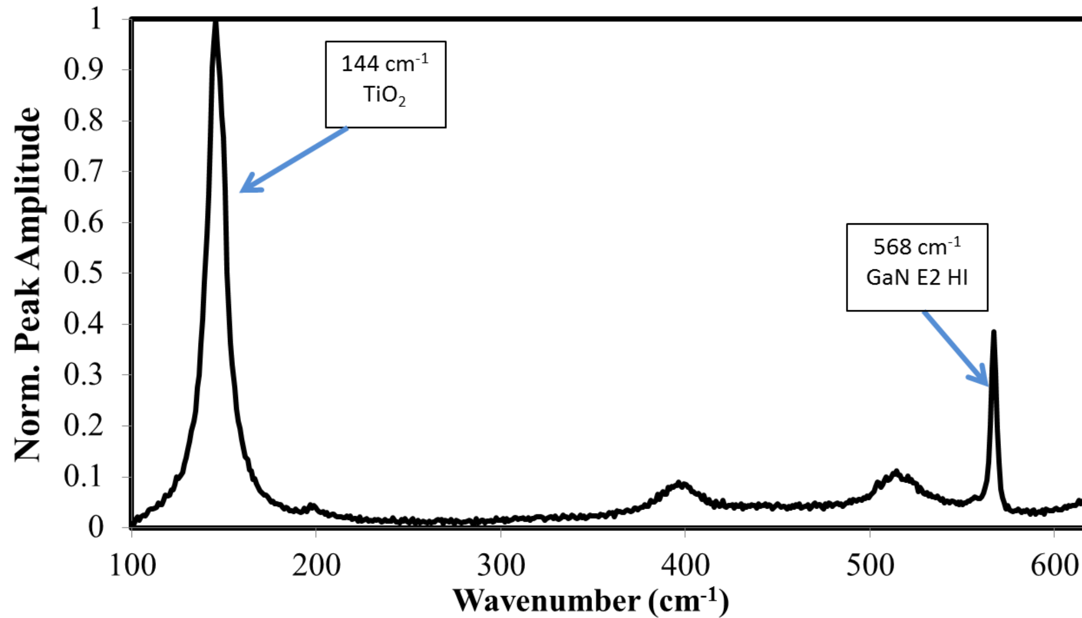

Figure 49: Raman peak of TiO_2 is centered around 144 cm^{-1}.

3.2.3 Calibration

In order to obtain accurate Raman temperature measurements on diamond, a precise calibration is necessary in the range of temperatures probed. The calibration of each sample was obtained by 20 measurements at each temperature condition in the location of interest. The Raman response to temperature rise was calibrated using the peak shift of the Raman spectrum. The calibration began at room temperature, and the temperature was uniformly increased to 30, 50, 75, 100, 125, and 150 °C using an INSTEC temperature controlled stage with a temperature stability of ± 1 °C. With each calibration of the diamond sample taken, a reference sample of silicon was also used to determine the temperature on the copper block. The peak shift coefficient for silicon was determined experimentally to be 0.02189 °C/cm^{-1} using a temperature controlled enclosure to ensure uniform temperature. The changes in the spectrum are fitted with a Voigt function, which is a convolution of Lorentzian and Gaussian form, resulting in

Figure 50. A linear fit was used to describe shifts in phonon frequencies with respect to change in temperatures. Uncertainty was determined from the sources of error including the 95% confidence interval of the calibration and fitted Raman spectra at the powered and unpowered conditions.

Table 6: Change in peak position vs. temperature for diamond calibration

Base Plate Temperature (°C)	**Actual Temperature (°C)**	**Peak Position (cm^{-1})**	**Delta ω**
Room Temp	21.43	1332.202	0
30	27.76	1332.151	-0.05145
60	55.23	1331.730	-0.47230
90	81.24	1331.474	-0.72773
120	109.96	1331.069	-1.13329
150	138.59	1330.552	-1.65017

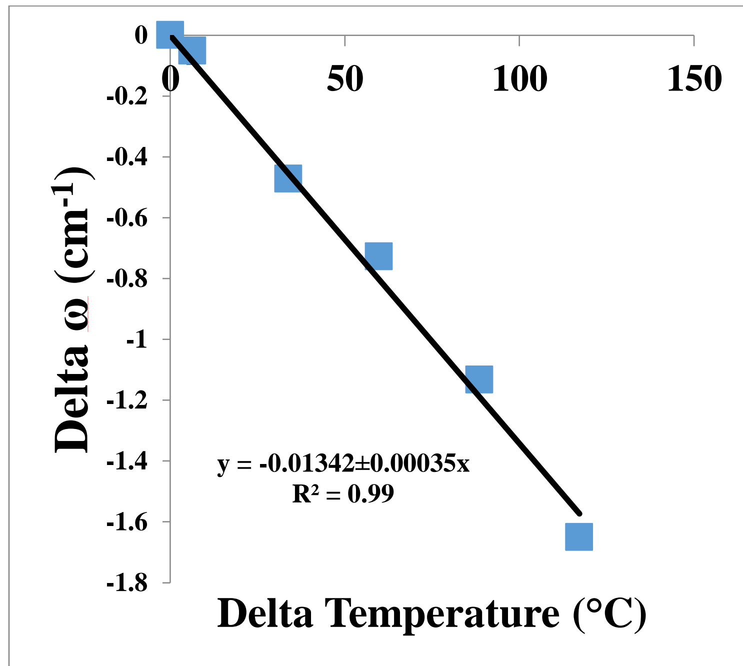

Figure 50: Temperature calibration from change in temperature to change in peak position of diamond.

3.3 Experimental Setup

Thermal property measurements were conducted using a Renishaw InVia Raman system using a 488 nm Ar+ laser and 3000 l/mm diffraction grating, with a laser beam diameter of 1μm as seen in Figure 51. The 488nm laser was used to prevent laser heating in the diamond due to its sub-bandgap wavelength. Silicon has a bandgap of 1.1 eV which would be heated by the 488nm laser. Laser heating was minimized by filtering the laser to 10% of its original power. Experiments were conducted with the laser light perpendicular to the basal plane of the diamond in a 180° backscattering configuration with a 100x lens.

The metal heaters were powered using a 4 point probing method to accurately measure the voltage drop and current in the metal heaters. The 4 point probing method is utilized to minimize electrical contact resistance between the probes and the contacts. The power and sourcing was accomplished with a Keithley 2400 SMU.

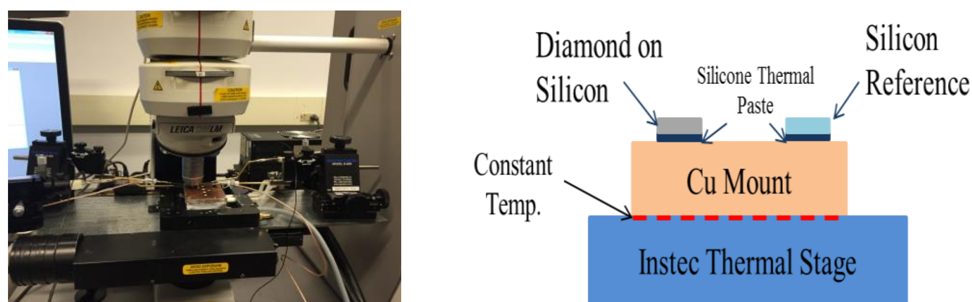

Figure 51: Experimental setup on Renishaw InVia Raman system using a 488nm laser (left) and schematic showing the calibration of diamond using known calibration of silicon reference sample (right).

The temperature of the measurements and calibration were held constant with an Instec heating stage. Due to high heat dissipation in the measurements, liquid cooling was required to stabilize the heating stage. Heat dissipations as low as 500mW increased the thermal stage above the constant base temperature of 30°C. A C300W industrial chiller was used for the cooling system. Samples were fixed on a 1000μm thick cooper mount, while a thin layer of silicone-based thermal paste was applied to the backside of the sample, avoiding areas on the sample that the silicon was etched away. The resulting Raman spectrum was analyzed with a Gaussian-Lorentzian (Voigt) fit to find peak parameters of the peaks in diamond, silicon, and nanoparticles.

3.4 Results and Discussion

Diamond on silicon wafers were grown based on a proprietary method. These wafers were then diced into $1cm^2$ samples and fabricated with specific lateral and vertical structures. The focus of this section will be on the thermal property results obtained on sample A, which will be used to compare all other samples. This sample was a high carbon growth sample, which showed poor thermal properties when compared to other samples. This sample was 1.1μm diamond grown on 300μm silicon and is shown in Figure 52. Figure 52 has structures designed at Georgia Tech as wells as structures designed by other institutions for their own measurements that utilized different geometries. Only device structures mentioned previously in this work will be presented.

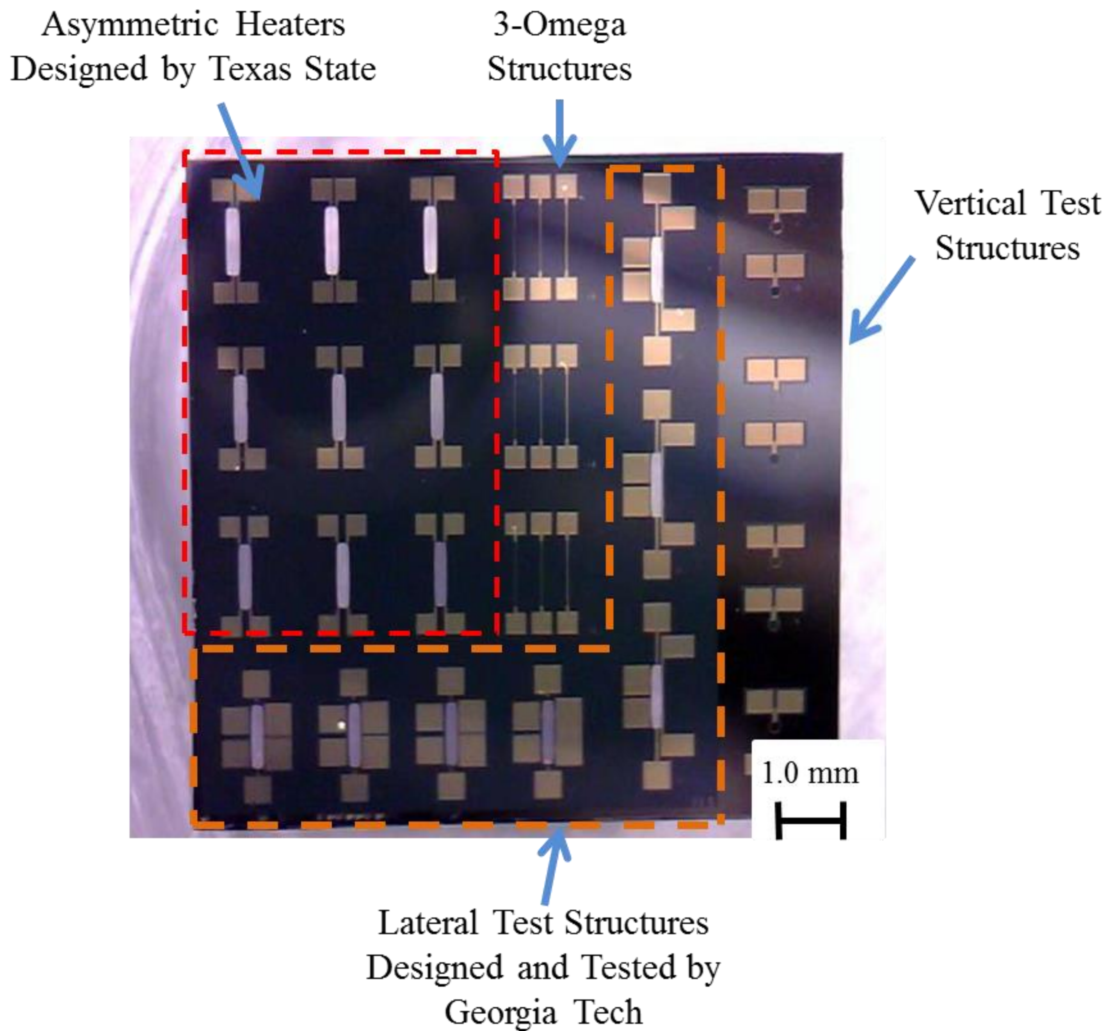

Figure 52: Magnified image of Sample B. Sample B has both lateral and vertical test structures. The vertical structures are on the right and the lateral structures are on the left.

3.4.1 Lateral/In-Plane Thermal Conductivity

In order to determine the lateral thermal conductivity in the samples of interest, devices were fabricated to ensure one dimensional heat flow in the lateral direction as seen in Figure 32. The geometry and material properties were used to create a finite element model that would compare the experimental to modeling results. This model as seen in Figure 53 could then be used to fit the data to the corresponding thermal properties. The thermal simulation using ANSYS Workbench 16.2 converged at 90,488

elements for the quarter symmetry model and 160,000 elements for the full model. A full model had to be used when fabrication errors were encountered and device symmetry could not be utilized. Some samples were not etched symmetrically or they had defects in the thin diamond film. This required the use of a full model to accurately represent the geometry of the samples. Increased refinement in the model was used near the areas of heat generation and where Raman measurements were taken. For all models, the base of the substrate was set at the INSTEC temperature stage input value, usually 30°C except for the temperature dependence study. Adiabatic boundary conditions were applied to all other surfaces because radiation and convection were shown to be negligible.

Raman thermography measures the change in temperature and stress in the material of interest, in order to compensate for changes in stress, multiple calibration measurements were conducted in the sample along the path of interest as described in Section 3.2.3.

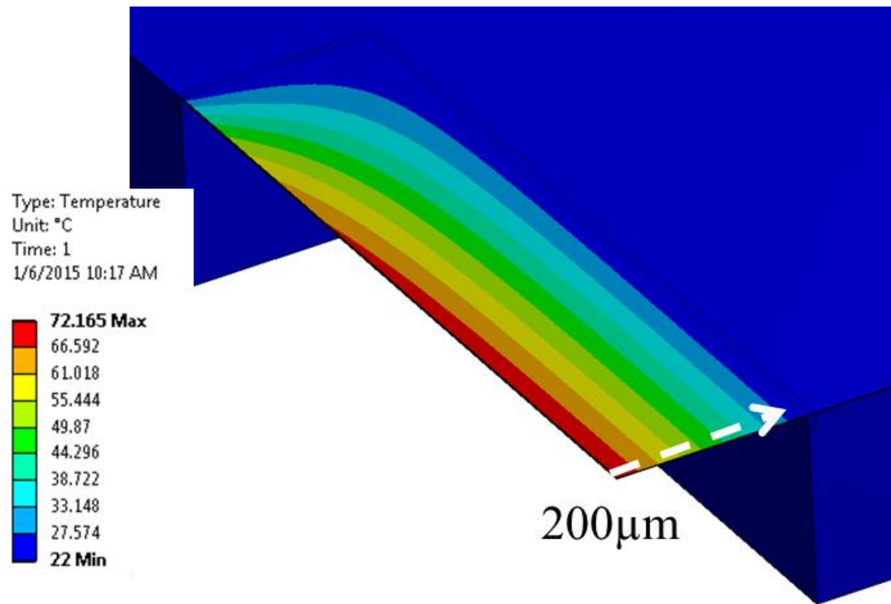

Figure 53: Finite Element Model of lateral thermal conductivity devices

The first sample measured was sample A, which was a high carbon growth diamond. It consisted of 1.1μm of diamond on a silicon substrate. The high carbon growth refers to the amount of CH_4 introduced in the chamber along with H_2. This sample was obtained from the edge of the wafer of interest as seen in Figure 54.

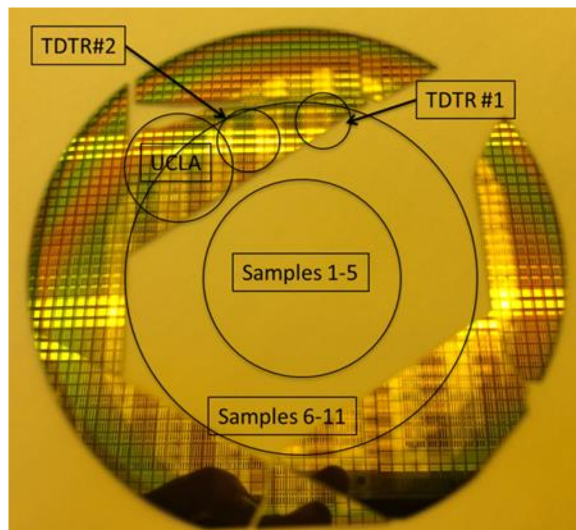

Figure 54: Sample A wafer depicting location of samples measured for thermal properties.

The results of the experiment under 500mW of power are seen in Figure 55. This value represents the average lateral thermal conductivity across the center of the membrane structure.

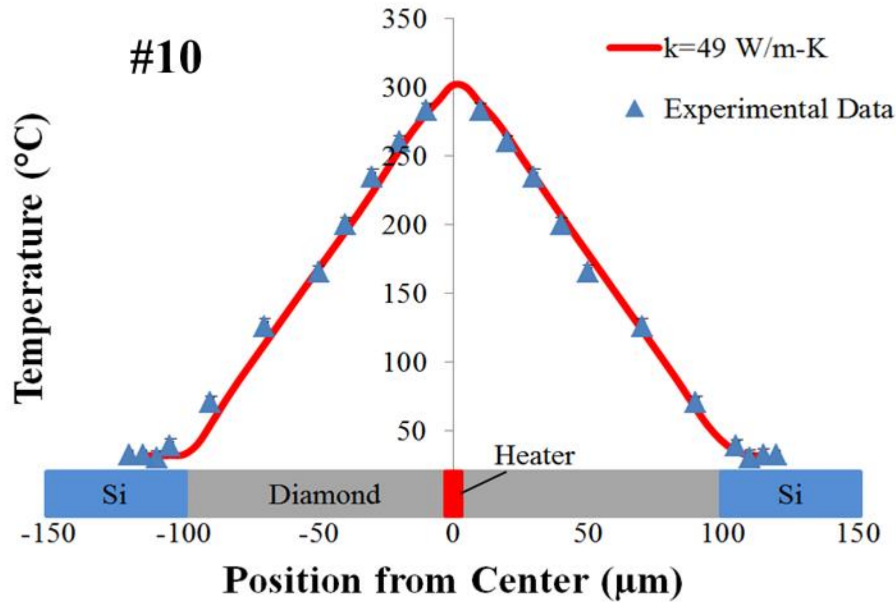

Figure 55: Sample A thermal conductivity measurements. The experimental data fit a lateral thermal conductivity of 49 ±4 W/m-K.

This low thermal conductivity (49 W/m-k) of diamond is due to the low carbon growth process. Due to proprietary reasons, the in-depth growth conditions were not revealed. This measurement was obtained near the edge of the wafer. The results obtained were consistent with other universities that measured Sample A but using other $1cm^2$ test structures. Figure 56 represent lateral thermal conductivity measurements obtained from Bristol University that show the measurements fall within the uncertainties. The image on the left corresponds to measurements made near the center of the wafer while the image on the right corresponds to measurements made on the edge of the wafer near the location of Sample A. The lateral thermal conductivity was found to be higher near the center of the wafer and decreasing diamond quality was found near the edges of the wafer. This could be attributed to the deposition process where the wafer may be heated non-uniformly or the mixture of the reactants can vary spatial during the

deposition process. Details on the deposition process were not provided from the manufacturer due to their proprietary method.

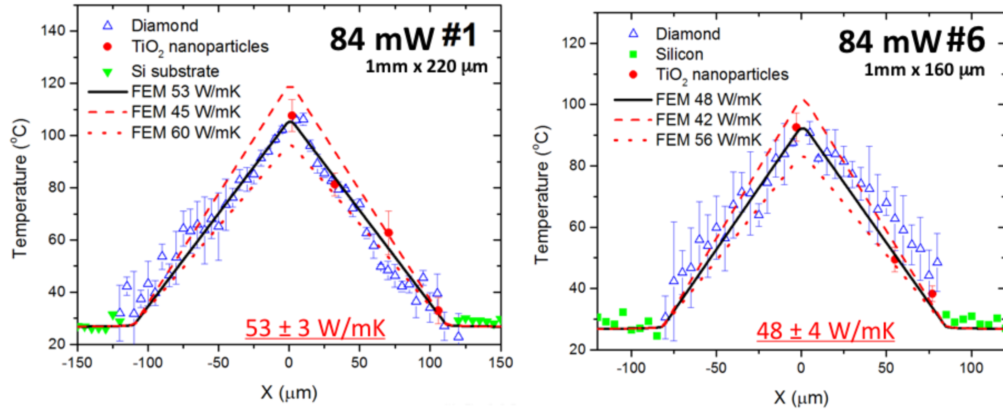

Figure 56: Measurements obtained on Sample A from Bristol University. (Left) Shows data from the center of the wafer. (Right) shows data from the edge of the wafer.

These results were validated by comparing data to results on the same sample but using time-domain thermoreflectance (TDTR). TDTR utilizes a pump-probe optical technique where a pump laser heats up a thin film sample and a probe laser measures the change in the reflectivity over time. This change in the probe's reflectivity can be matched to a model in order to extract thermal characteristics[69]. Using Raman thermography, a lateral thermal conductivity on Sample A of 49 ± 4 W/m-K was measured which takes an average across the thin diamond film. TDTR by Luke Yates at Georgia Tech used a 1cm^2 sample from the same wafer as sample A at room temperature obtained a top side lateral thermal conductivity of 55.7±9.6 W/m-K as seen in Figure 57. The measurements from TDTR were obtained near the edge of the wafer. These measurement differences can be attributed to spatial variations in the diamond sample as well as the slight temperature dependence of diamond which will be discussed in Section 3.4.4. TDTR's temperature rise (~10°C) is much smaller than the temperature seen in the

Raman measurements in this work (~100°C). Higher temperature's reduce the average thermal conductivity of the diamond thin film.

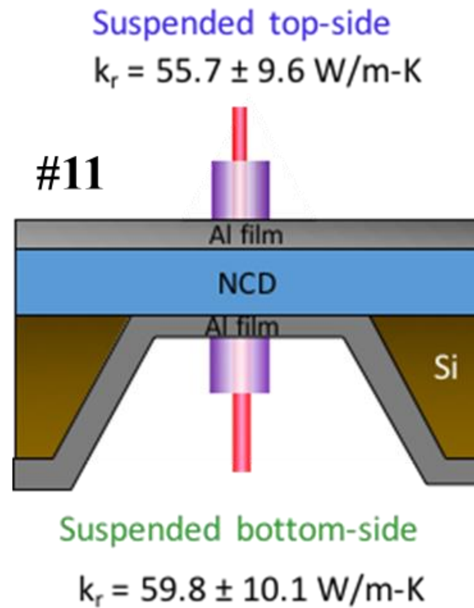

Figure 57: TDTR schematic of lateral thermal conductivity measurements. TDTR at Georgia Tech obtained 55.7 W/m-K on the top side and 59.8 W/m-K from the bottom-side.

The next sample measured was a sample from the same supplier but with lower carbon content in the growth process which was expected to yield higher quality CVD diamond on Si. The geometry was held constant while the growth conditions were altered for Sample B. The temperature profile for 100mW of power dissipation is seen in Figure 58. Sample B's temperature profile was fit to a lateral thermal conductivity of 105±5 W/m-K.

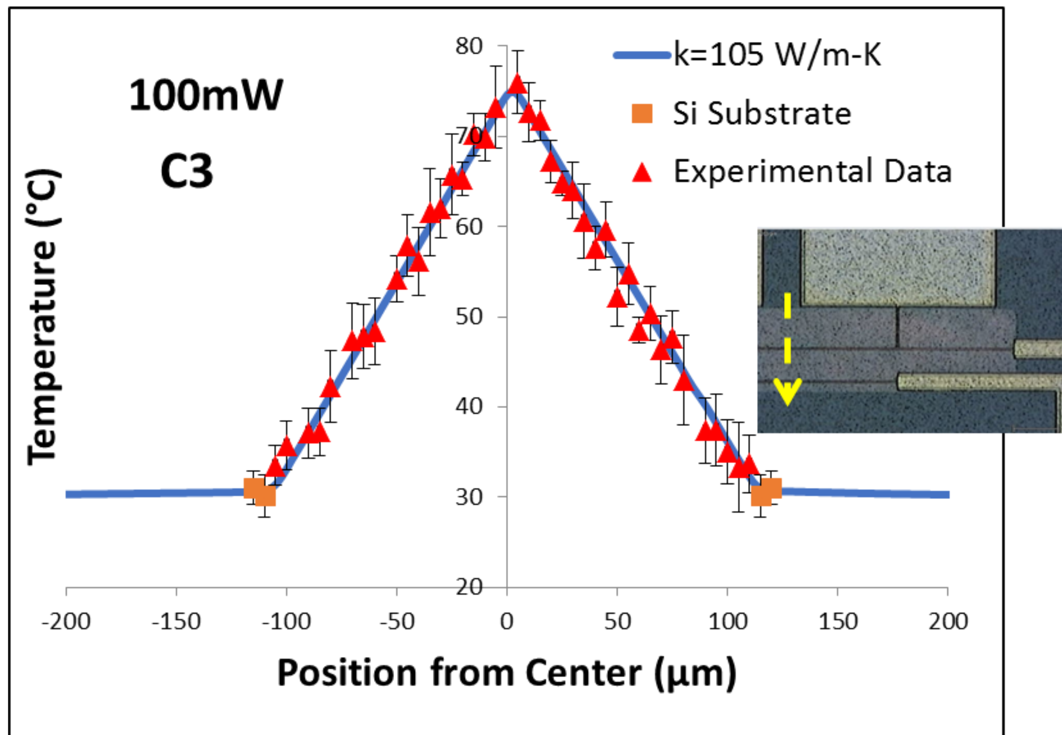

Figure 58: Sample B thermal conductivity measurements. Due to changing growth conditions, the lateral thermal conductivity of sample B was 2.14x higher than the sample A.

Measurements were also shown to be successful on asymmetric membrane structures. Measurements were taken on Sample B using the common sample. Due to issues in fabrication, the center heater was unable to be used for joule heating. Smaller, asymmetric heaters were used, while the temperature profile and membrane's geometry were used to fit to a finite element model. As seen in Figure 59, the lateral thermal conductivity was determined to be 107 ± 6 W/m-K.

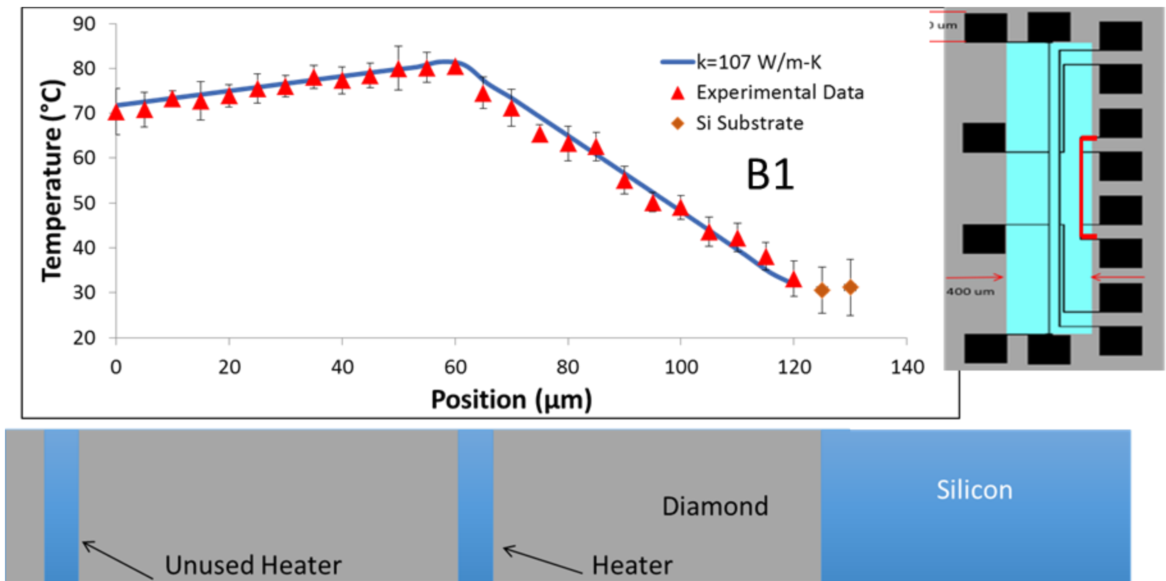

Figure 59: Sample B's lateral thermal conductivity measurement using asymmetric heaters.

In order to minimize spatial variation in the diamond, specific test structures were created that placed TDTR test structures, that need a thin (90nm) transducer usually made of aluminum, and Raman structures within 1200µm of each other. TDTR obtained a lateral thermal conductivity of 86 W/m-K and Raman thermography obtained a lateral thermal conductivity of 85±4 W/m-K as can be seen in Figure 60.

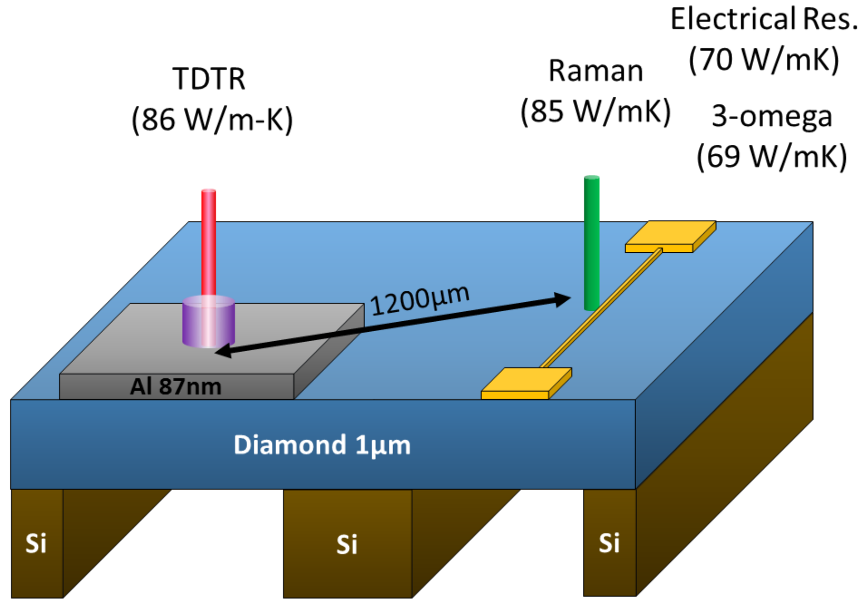

Figure 60: TDTR, Raman thermography, 3-omega, and electrical resistance measurement comparison on Sample B3.

The results from Sample B were compared to other institutions that measured other 1cm^2 squares from the same wafer in order to understand spatial variation in the thermal properties of the same wafer. A full comparison for Sample B was conducted for the lateral thermal conductivity as seen in Figure 61. Measurements near the edge of the wafer showed higher values excluding the center sample, C3. These variations can be attributed to measurement error as well as poor deposition is certain areas. Raman measurements on average produced a lateral thermal conductivity of 97.3 W/m-K and TDTR's measurements averaged 84.0 W/m-K.

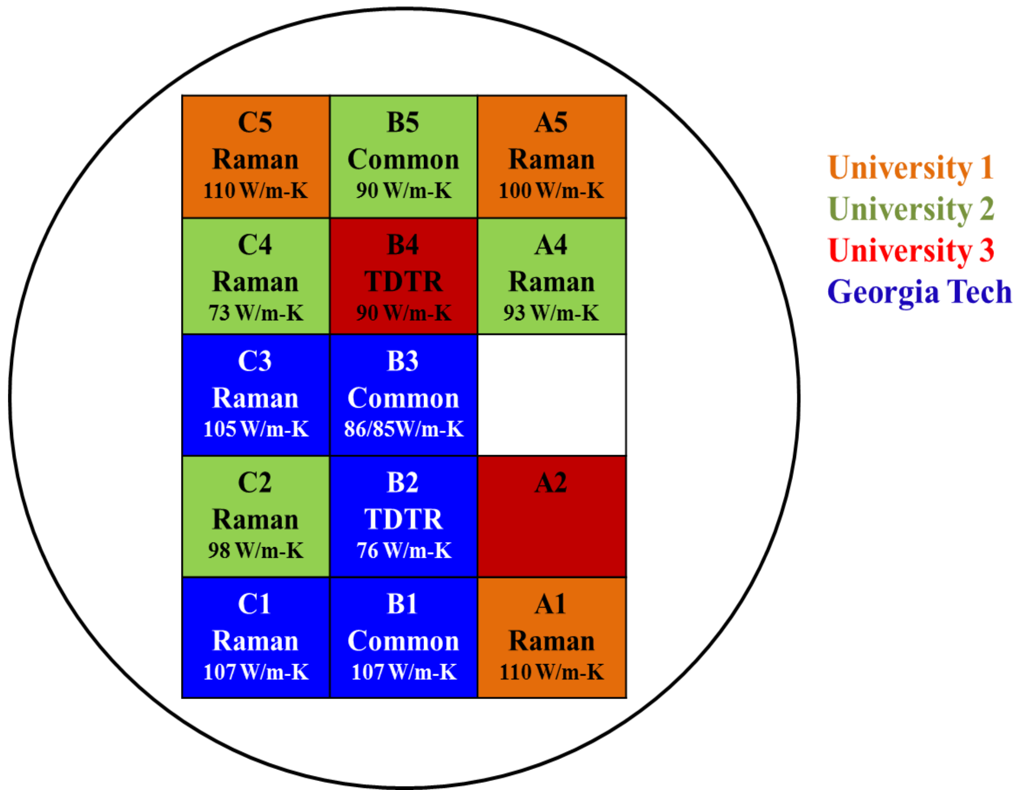

Figure 61: Spatial variation in lateral thermal conductivity measured using Raman thermography and TDTR from various institutions

3.4.3 Vertical/Cross-Plane Thermal Conductivity and Thermal Boundary Resistance

The vertical thermal conductivity measurements were conducted using ring structures previously mentioned in Figure 38 and as well in Figure 62 for sample A. Measurements were taken on the surface of the heater using a cluster of TiO_2 nanoparticles, the through thickness temperature of the diamond and the surface of the silicon. Measurements were taken at various power conditions and fit to a FEA model for the vertical thermal conductivity and thermal boundary resistance between the silicon and the diamond. The thermal simulation using ANSYS Workbench 16.2 converged at approximately 250,000 elements for the full model. A constant base temperature of 30°C

was used as the bottom boundary condition with adiabatic boundary conditions on all other boundaries. Radiation and convection were found to be negligible in the analysis. The lateral thermal conductivity from previous measurements was held constant at 49 W/m-K. The results are seen in Figure 63 and Table 7.

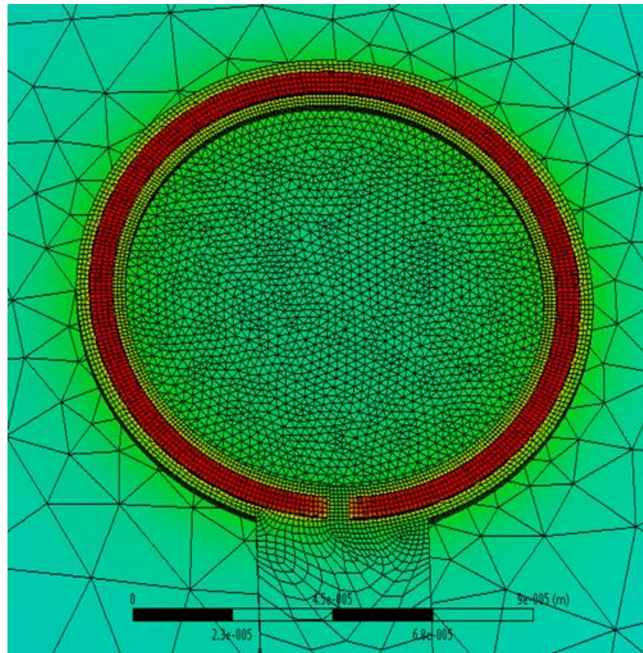

Figure 62: FEA model of 100µm diameter vertical ring structure. This model was used to fit the various temperature profiles to their corresponding thermal conductivities.

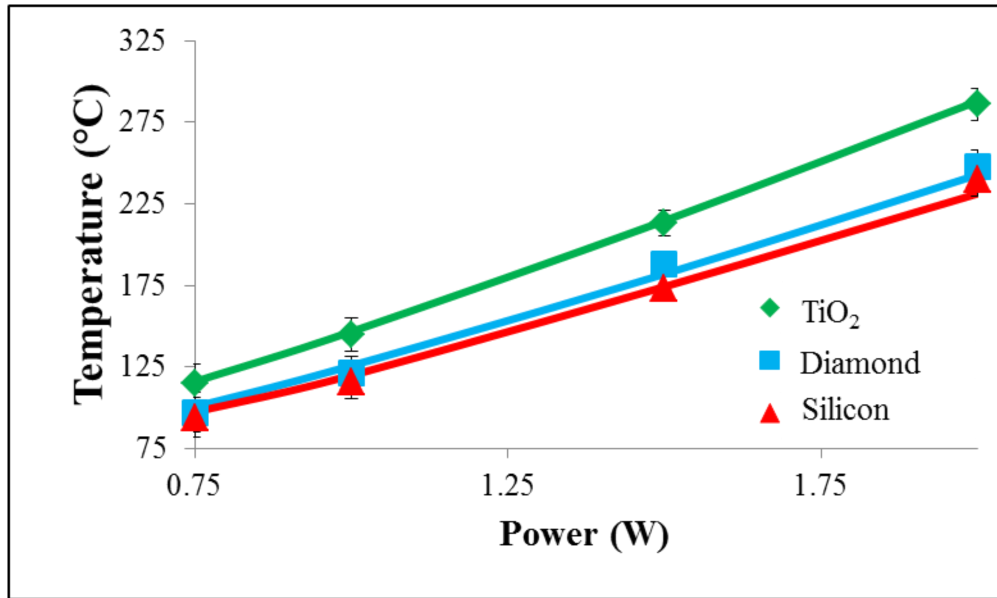

Figure 63: Vertical thermal conductivity measurements of Sample A. A FEM model was fit to the experimental data obtained from various power conditions on the ring structure. The model uses $k_{lateral}$=49 W/m-K, $k_{vertical}$=155 W/m-K, TBR=30m^{2}K/W

Table 7: Cross-plane thermal conductivity and Thermal Boundary Resistance results for Sample A.

In-Plane (W/m-K)	Cross-Plane (W/m-K)	TBR (m^{2}K/GW)
49±4	155±70	30±5

The cross-plane thermal conductivity was found to be 155±70 W/m-K and a thermal boundary resistance between the diamond and the silicon as 30±5 m^{2}K/GW. The high uncertainty on the cross-plane thermal conductivity can be attributed to the low temperature sensitivity to the change in vertical conductivity. These values give an anisotropic ratio of 3.16. This high anisotropic ratio can be attributed to the fact that that this is within the first 1.0 μm of nucleation and growth. The grains are have not finished

the transition into true columnar growth structure. These results were compared to other institutions and were found to be within the uncertainties. The results from a collaborating university, Bristol University, are seen in Table 8. TDTR at Georgia Tech obtained a vertical thermal conductivity of 120 W/m-K and a diamond on silicon TBR of 13.6 m^2K/GW.

Table 8: Vertical thermal conductivity and Diamond on silicon TBR obtained from a collaborating university.

Sample	In-Plane TC (W/mK)	Cross-Plane TC (W/mK)	TBR (m^2K/GW)
A	48 (from membranes)	180 -50/+70	30±2

3.4.4 Temperature Dependence

As seen in Figure 55, a large temperature rise is seen at the center of the membrane with a temperature of 300 °C while the edges of the membrane were on the order of 30°C. Thus, the thermal conductivity measured for Sample A could contain some temperature dependence due to the large variation in temperature. To further investigate this, a temperature dependence study was completed on sample A, the high carbon growth sample. This was accomplished by using a lower heater power (100 mW) and varying the base of the sample using an INSTEC thermal stage from 30°C to 150°C. To obtain a more accurate temperature of the diamond sample, a silicon reference sample mounted near the diamond sample as a fiduciary piece on which the Raman temperature was measured seen in Figure 51. By changing the base temperature, the temperature distribution and thermal conductivity was measured for different temperature conditions. The results are shown in Figure 64 and Table 9.

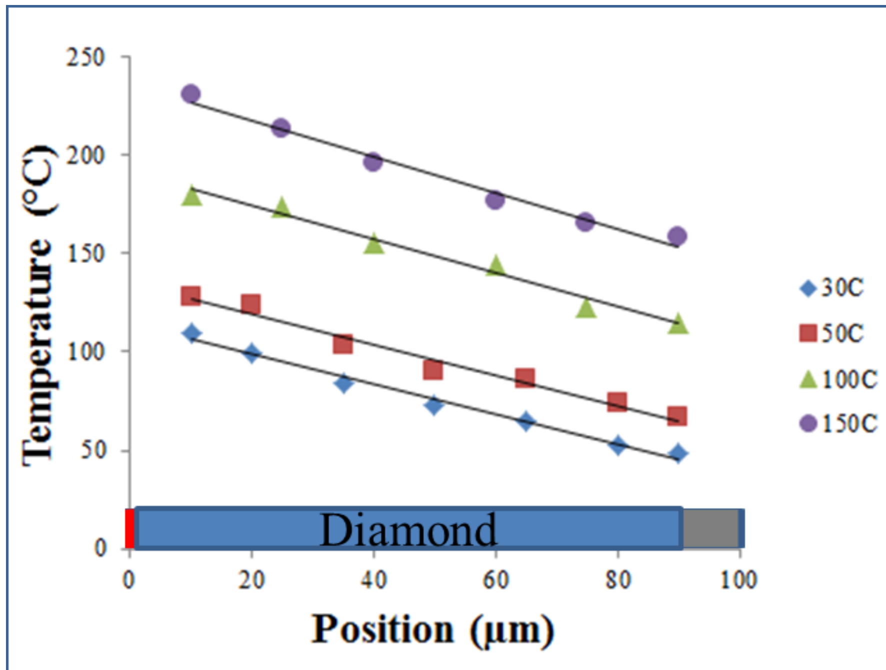

Figure 64: Temperature profile based on varied base temperature conditions to determine temperature dependence of lateral thermal conductivity of Sample A.

Table 9: Temperature dependent lateral thermal conductivity measurements for Sample A.

Base Plate Temperature (°C)	Surface Temperature (°C)	Thermal Conductivity (W/m-K)	Power Condition (mW)
30	27.7	59.8	100
50	47.6	58.5	100
100	90.5	52.8	100
150	138.8	49.4	100

These measurements were taken on sample A, and obtained different values for the lateral thermal conductivity. Sample A's lateral thermal conductivity decreased by

16.9% with 111.1°C increase in temperature. This shows a low temperature dependence in the ranges studied as compared to other materials such as silicon and silicon carbide.

This first micron of diamond growth on silicon substrate does not have the same thermal properties of bulk or thicker CVD diamond. Figure 65 shows Sample B with a low carbon growth using a Scanning Electron Microscope (SEM) image. The first 500 nanometers of diamond show little growth in the upward direction facilitating high quality CVD diamond. As the growth continues to 1μm the columnar growth structure is evident and represents diamond with high thermal conductivity. This transition region within 500 nm of the nucleation reduces the overall thermal conductivity of this sample. Figure 66 shows a High Resolution Transmission Electron Microscope (HRTEM) image of Sample B's diamond on silicon interface. The image shows an amorphous interface layer which random oriented grains directly above the interface. Figure 67 shows dark field cross section images with (111) grains highlighted. These images also support the hypothesis that long columnar grains exist but do not tend to extend from the growth interface to the surface.

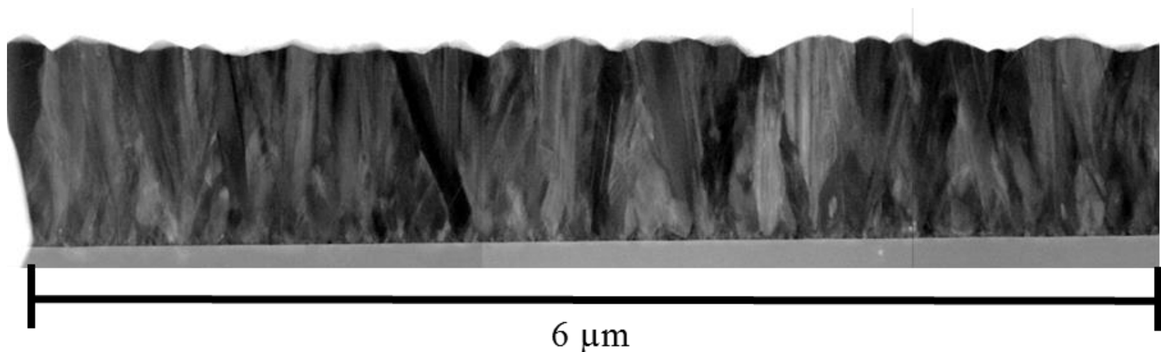

Figure 65: SEM images from UCLA of sample B. This lower carbon growth rate increased columnar growth in the diamond allowing for higher anisotropic thermal conductivity.

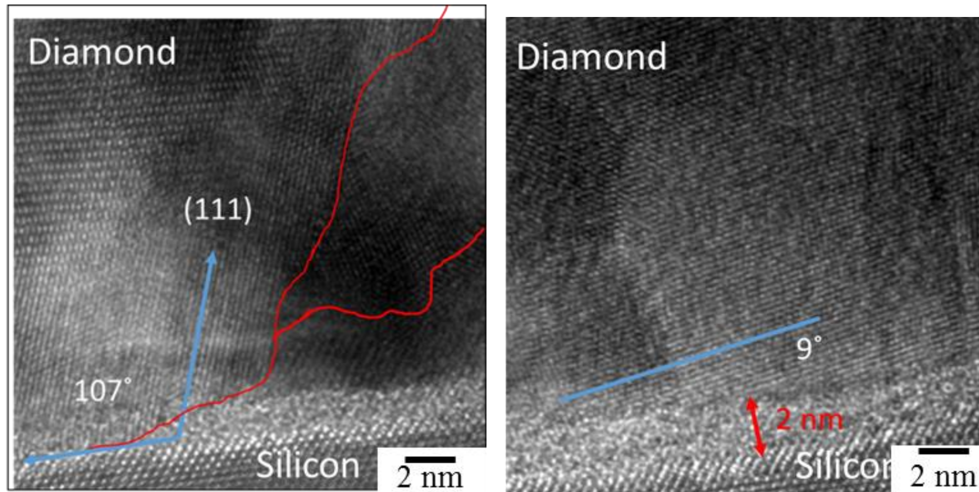

Figure 66: High Resolution Transmission Electron Microscope (HRTEM) image of Sample B's Diamond on Silicon interface via Dr. Mark Goorsky at UCLA.

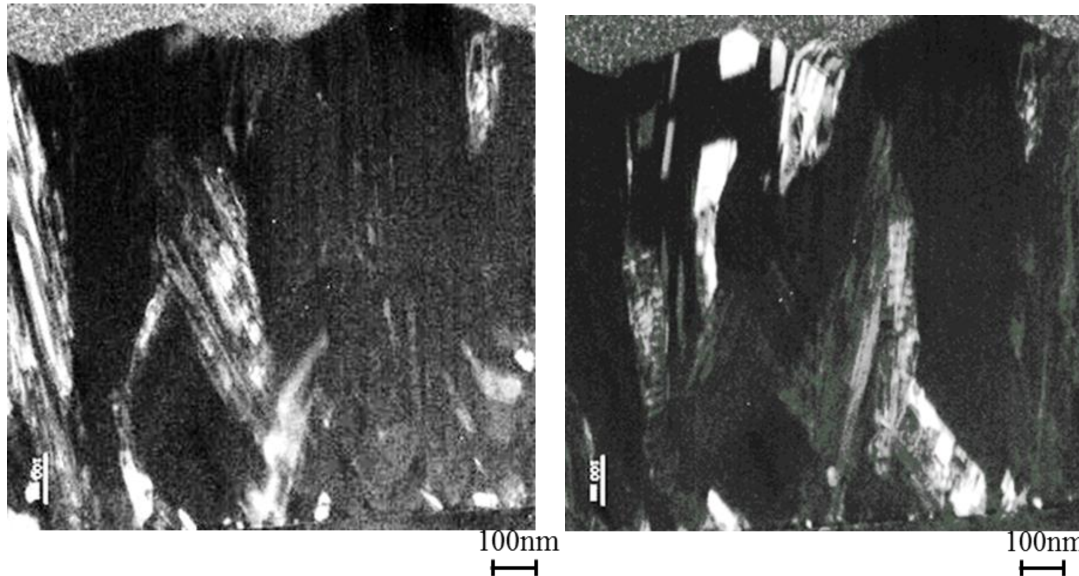

Figure 67: Cross section (111) dark field images showing grains with similar orientation via Dr. Mark Goorsky at UCLA of companion sample to Sample B.

3.5 Summary and Conclusions

In order to determine the thermal properties in thin diamond films, device structures had to be designed and fabricated that isolated heat flow in the lateral direction and in the vertical direction. Thin membrane structures were used to isolate lateral heat flow and a length to width ratio of 5:1 was chosen due to its ability to compare the FEA

and analytical model most accurately. Vertical test structures were designed to isolate heat flow vertically through filled and unfilled ring structures. Temperature measurements could be taken on the heater surface due to the use of nanoparticles, through thickness temperature of the diamond, and the silicon surface temperature.

Raman thermography was used as a noncontact approach that did not interfere with device operation by using a sub bandgap laser on diamond. Raman thermography measures the change in the vibrational state which is affected by temperature and stress. Raman can measure the change in temperature by comparing the unpowered vibrational state to the powered state along with an accurate temperature calibration.

Measurements were taken on sample A with a high carbon growth rate. A lateral thermal conductivity of 49±4 W/m-K, a vertical thermal conductivity of 155±70 W/m-K and a thermal boundary resistance of 30 ±5 m^2K/GW were found when comparing to a FEA model. A temperature dependence experiment was conducted on sample A showing lateral thermal conductivity decreased by 16.9% with a 111.1°C increase in temperature. This technique was validated by comparing the results to TDTR and other universities for both lateral and thermal conductivities. Both thermal conductivity measurements fell within the given uncertainties while the TBR did not.

These measurements provide contrast to the idea that diamond has the overall best properties for AlGaN/GaN HEMTs. Figures were provided showing randomly oriented grains near the nucleation surface and long columnar grains exist but do not tend to extend from the growth interface to the surface. Diamond samples with a high thermal boundary resistance and low thermal conductivity within the first micron of growth can

undermine the attractive and advantageous properties of thick diamond samples (>100µm).

CHAPTER 4: MATERIAL CHARACTERIZATION USING QUICK SCREENING METHODS

4.1 Introduction

The nucleation and growth conditions that are selected for a diamond sample have a profound effect on the microstructure and chemical makeup of the diamond. The evaluation of the diamond quality is key in ensuring the thermal properties meet the necessary standards for thermal boundary resistance and thermal conductivity. Decreased quality from various samples as well as from various locations on the diamond sample can greatly increase overall junction temperatures in the device and lead to performance and reliability issues.

Many techniques to determine thermal properties in thin films require destructive processes that can affect the diamond quality or render the diamond useless for thermal application. Such techniques include time domain thermal reflectance (TDTR), which require a thin transducer layer to be applied to the diamond surface. 3 Omega, Raman thermography, and electrical resistance thermometry require fabrication of line metal line heaters to determine thermal properties from the material of interest [69-71]. These methods are not only destructive but take a large amount of time to execute.

4.2 Raman Spectra and FWHM

A nondestructive way to obtain information about the diamond quality is through its Raman spectrum. Obtaining a Raman spectrum can take less than one second compared to the hundreds of measurements needed to use Raman thermography.

Graphite and other sp^2 bonded amorphous carbons are strong Raman scatterers even though they have large optical absorption. Diamond and related carbons also have strong and easily identifiable Raman spectra [71]. The first order band appears as a single sharp peak at 1332cm^{-1}, which is the characteristic diagnostic feature for diamond as seen in Figure 68 .

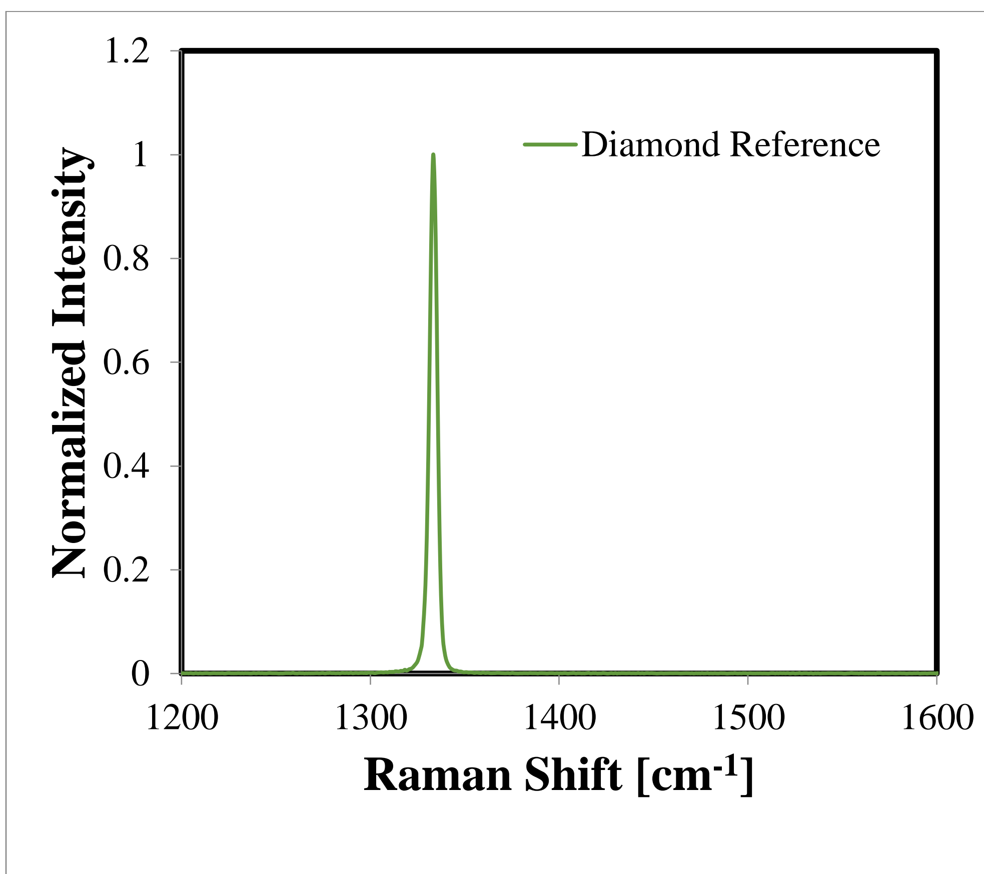

Figure 68: Natural Diamond Ultra Violet (UV) Raman spectra. The sharp peak at 1332 cm^{-1} corresponds to the high quality diamond.

This Raman spectrum was taken using a UV 325nm HeCd laser with 39x UV objective on a Horiba Jobin Yvon Raman system as seen in Figure 69. This sample was a natural diamond anvil that was received from Texas State University. This diamond

sample represents the highest possible thermal conductivity in diamond, due to its uniform and single crystalline form.

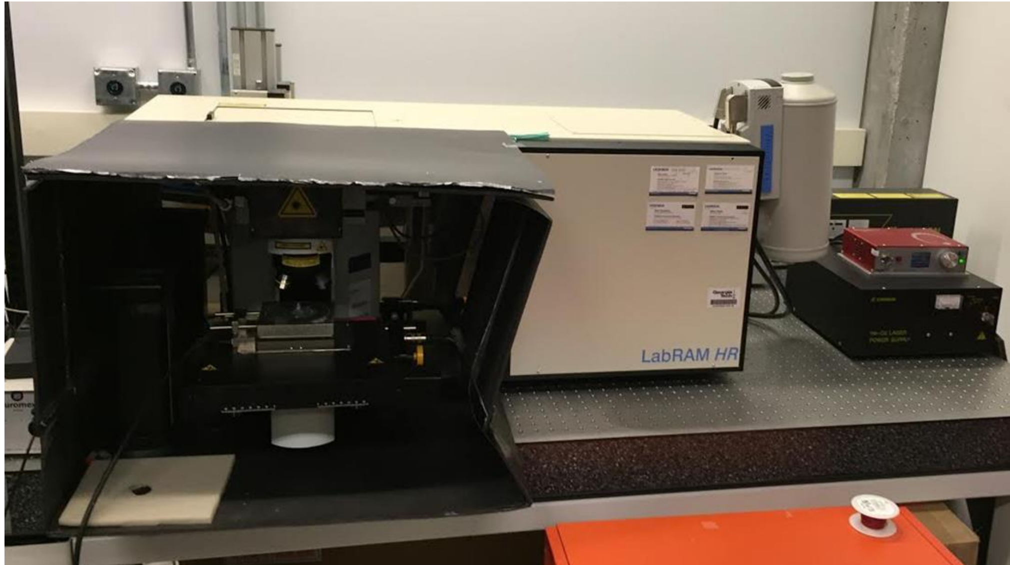

Figure 69: Horiba Jobin Yvon Raman Spectroscopy Setup using UV laser at 325nm.

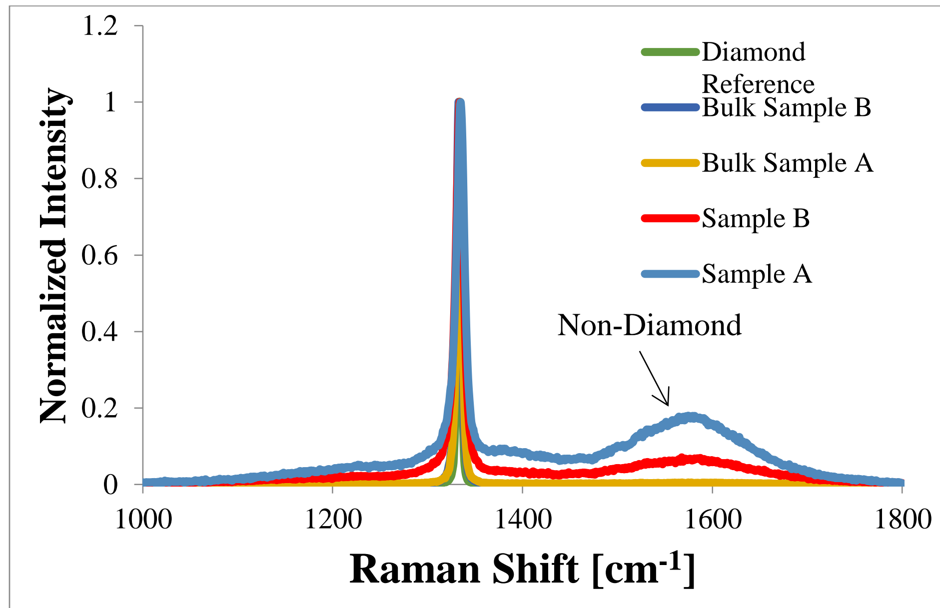

Figure 70: UV Raman Spectra comparison of various samples. Diamond reference refers to the bulk diamond qualities and Sample A has a lateral thermal conductivity of 49 W/m-K.

In Figure 70 five diamond samples with decreasing thermal conductivity are compared. All samples have a large peak at 1332 cm^{-1} which correlates to the diamond or sp^3 hybridization of diamond. As the thermal conductivity of the samples decrease, an increase in the integrated area occurs from 1500 cm^{-1}to1800 cm^{-1}. This increase in area correlates to an increase in non-diamond carbon or sp^2 bonds found in the material due to poor deposition process and quality [71]. The in-plane vibrational mode in graphitic carbon has a peak at 1580 cm^{-1} and is due to the strong in-plane bonds of the graphite which allows for its sheet-like qualities. This graphite peak is combined with the impurities from the diamond-like carbon occurring from 1500 cm^{-1} to 1800 cm^{-1}. The diamond-like carbons are amorphous carbon films formed from the dehydrogenation of organic materials. Calculated Raman spectrum from analysis of multi-atom physical models of the structure suggest that the percentage of tetrahedral carbon is small in diamond-like carbon [72]. The Raman spectrum of the four diamond-like carbons examined are distinctly different from any of the graphitic carbons and support the idea that diamond-like carbon is structurally distinct [71].

The Raman spectrum can also provide diamond quality information based of the full width half max (FWHM) of the 1332 cm^{-1} diamond peak. Figure 71 depicts how the FWHM, or linewidth, is determined. It is determined by finding the mid-height of the peak, subtracting the baseline, and the corresponding width.

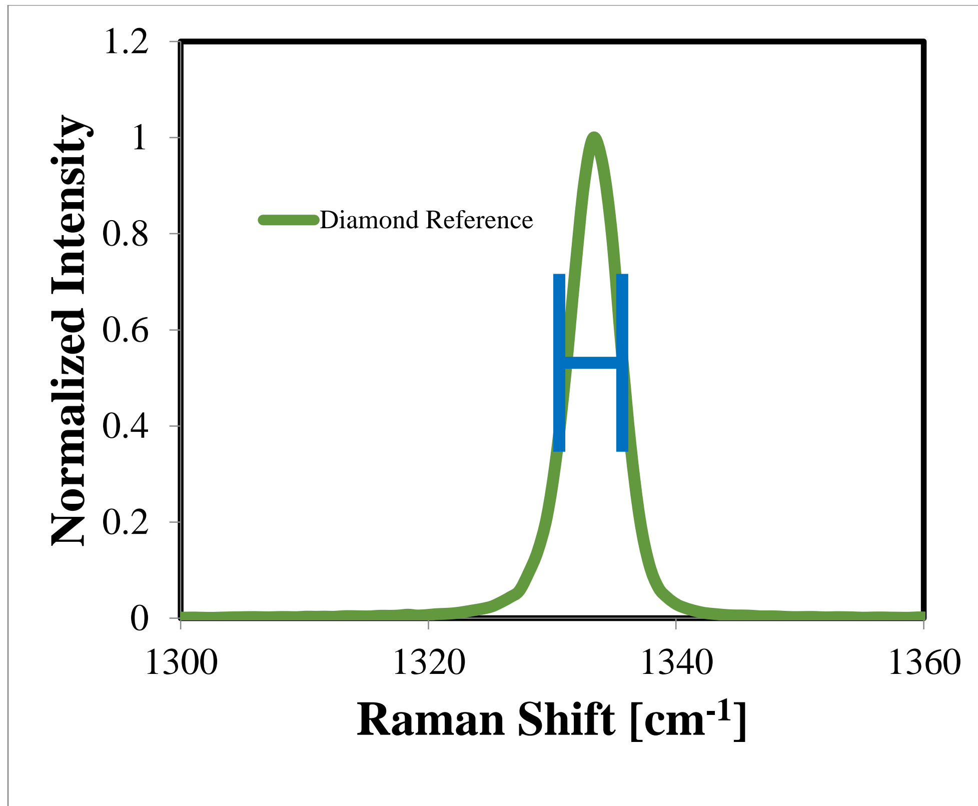

Figure 71: FWHM Graphical representation on a diamond peak centered around 1332 cm^{-1}

A comparison of 8 samples with known thermal conductivity was conducted to evaluate the diamond quality using the UV Raman FWHM as seen in Table 10. The thermal conductivity vs. FWHM for these samples is seen in Figure 72**.**

Table 10: Diamond FWHM and thermal conductivity comparison

	Thickness (µm)	Peak Position (cm^{-1})	FWHM (cm^{-1})	"k" by FTIR (W/m-K)
Diamond Anvil	-	1334	**6.3**	**-**
Bulk Sample A	511	1333.2	**5.5**	**2137**
Bulk Sample B	352	1333.8	**5.7**	**1927**
Bulk Sample C	449	1333.6	**6.6**	**1519**
Bulk Sample D	389	1334.5	**7.5**	**1284**
Bulk Sample E	534	1329.9	**7.8**	**714**
Bulk Sample F	525	1333.2	**9.5**	**695**
Sample A	1.1	1333.7	**13.58**	**49**

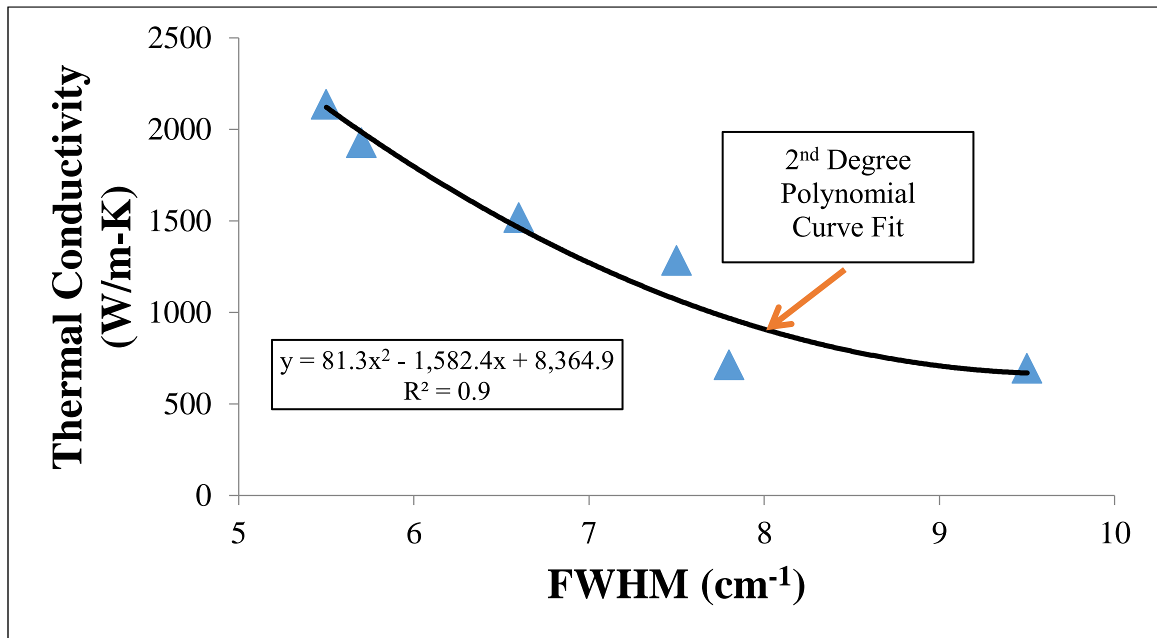

Figure 72: Thermal conductivity vs. FWHM for free standing diamond

The FWHM of the Raman shift plotted against the thermal conductivity shows a basic correlation as seen in Figure 72. These parameters are an indication of the general quality of the diamond and thus *k*. However, they are not as sensitive to variations in k as the CH absorption [71] which will be discussed in the next section.

4.3 FTIR

Fourier Transform Infrared Spectroscopy (FTIR) is an experimental technique where Infrared (IR) radiation passes through a sample and the radiation is absorbed by the sample and some is transmitted through. The resulting spectrum represents the molecular absorption and transmission, creating a molecular fingerprint of the sample [73, 74].

Figure 73: Thermo Scientific Nicolet iS50 FT-IR spectrometer at the Georgia Tech's Organic Cleanroom.

FTIR measurements were conducted in Georgia Tech's organic clean room and is pictured in Figure 73. FTIR is utilized to determine the quality of diamond. This is done by observing the stretch modes of Carbon-Hydrogen ($CH_{x)}$ species within the film by measuring the absorption of the IR spectrum near the range 2760-3030 cm^{-1} as seen in Figure 74. The CH_x absorption correlates to the overall diamond thermal conductivity through the integrated area after subtracting a linear baseline as seen in Figure 74 and Figure 75 [75]. The greater the absorption of the CH species rather than the tetrahedral

carbon-carbon bonds, the lower the quality of diamond. CH bonds in a diamond sample represent a defect where a hydrogen atom was not replaced by a carbon atom in the CVD process. The frequency of the bond vibration is shifted slightly for bonds in different local environments, allowing to differentiate CH_x groups. For example, the CH stretch signatures of hydrogen bonded to sp^2-bonded carbon appear above 2950 cm^{-1}, while those associated with sp^3-bonded carbon appear below 3000 cm^{-1} [76]. These CH bonds or defects increase the phonon scattering in the diamond sample. FTIR was not able to measure samples thinner than 20μm, so Sample A and Sample B were unable to be measured.

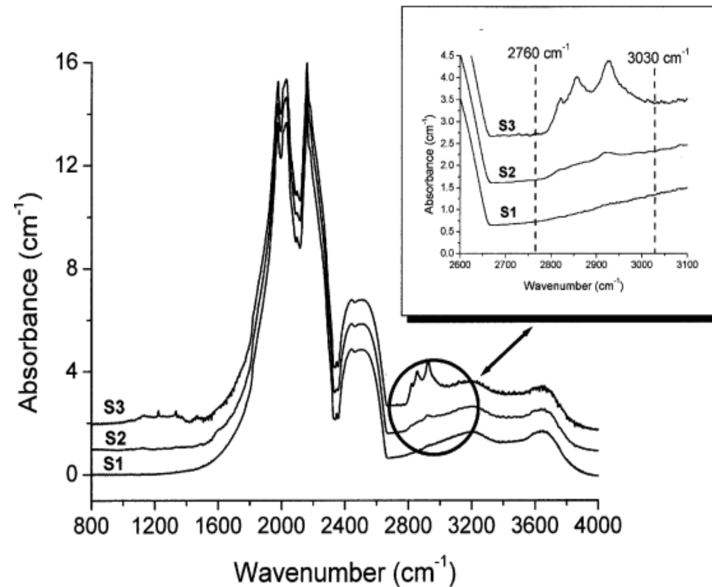

Figure 74: The IR absorption spectra and the measured integrated absorption between 2760 and 3030 cm^{-1} [75].

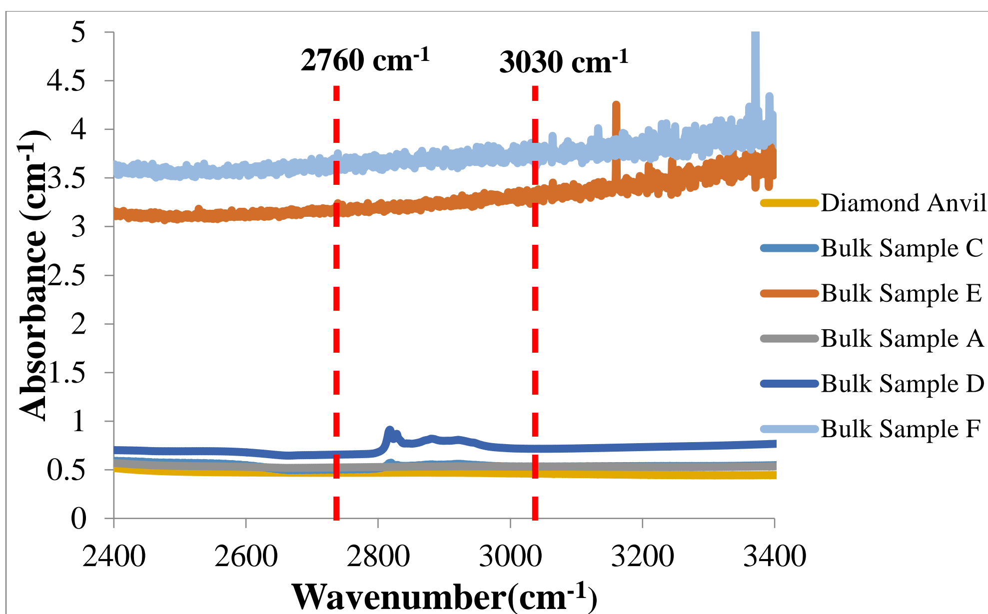

Figure 75: FTIR results showing CH stretching region from 2760cm^{-1} to 3030cm^{-1} relation to thermal conductivity

Table 11: FTIR comparison of thermal conductivity to integrated area

	Thermal Conductivity (W/m-K)	Integrated Absorption (cm^{-1})
Diamond Anvil	2400	104.72
Bulk Sample A	2137	144.2
Bulk Sample C	1519	146.2
Bulk Sample D	1284	204.17
Bulk Sample E	714	367.23
Bulk Sample F	695	390.4

Figure 75 and Table 11 show the results from the FTIR study. The samples with the greatest absorption between 2760cm^{-1} to 3030cm^{-1} correspond to the samples with the lowest thermal conductivity. Whereas, the diamond anvil sample, with no CH stretching represents the ideal case with the highest thermal conductivity of natural bulk diamond. In Figure 76, the integrated absorption between 2760 and 3030cm^{-1}, measured after

subtracting a linear baseline, is plotted against room temperature thermal conductivity. The data was fit to the 2nd degree polynomial which is seen in Figure 76.

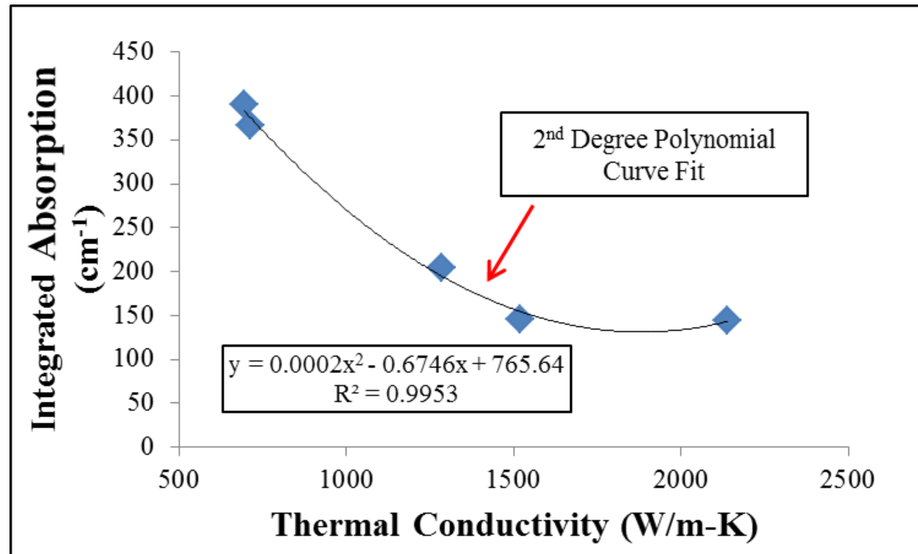

Figure 76: Graphical representation of FTIR integrated area to thermal conductivity

FTIR is an effective tool as a quick screening method to determine relative diamond quality and thermal conductivity. This method does not require sample modification and can be completed rapidly. FTIR does have a drawback that it was unable to correlate samples that had a thickness under 20µm due to saturation in the region of interest examining the CH absorbance.

4.4 XPS

X-ray photo electron spectroscopy (XPS) is a surface measurement technique used to measure the elemental composition, empirical formula, chemical state and electronic state of the elements on a materials surface. XPS spectra are measured by irradiating a material's surface with a beam of X-rays and then measuring the kinetic

energy and amount of electrons that escape the top 10 nm of the material. XPS measurements require a high vacuum (10^{-8} millibar) conditions [77].

Figure 77: Thermo K-Alpha XPS at Georgia Institute of Technology

For the material characterization of diamond thin film, XPS is useful to obtain the ratio of sp^3 to sp^2 bonds on the sample of interest. This ratio gives detail into the thermal conductivity. For this experiment, the Thermo K-Alpha XPS with Al (Kα) source at 1486.69 eV was used at Georgia Tech as seen in Figure 77. This experiment used an elliptical spot size of 400 μm major axis and a depth penetration of 9-10nm. Argon etching with 200 eV was also conducted to remove any surface materials that would interfere with the experiment such as adventitious carbon or organic contamination.

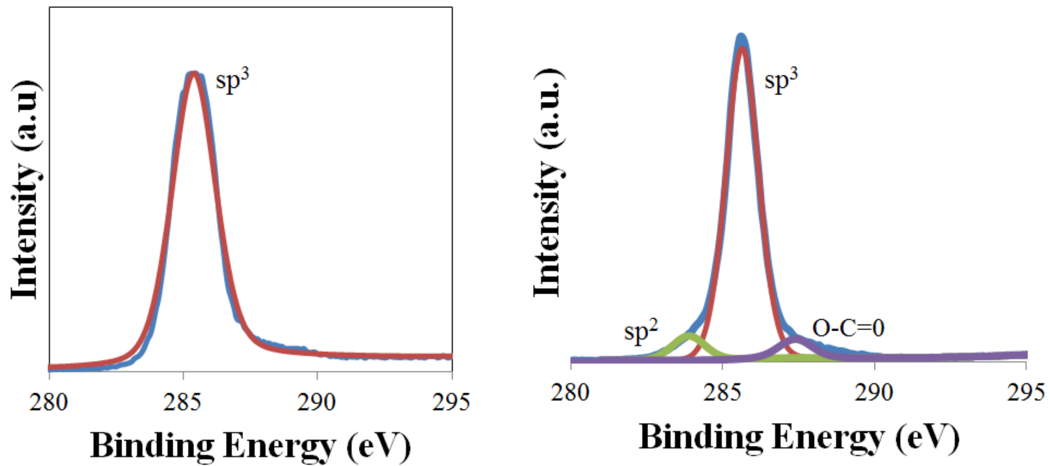

Figure 78: XPS of Bulk Sample F (left) and Sample A (right). The sp^2 content in Sample A shows the poor quality in the microstructure.

Table 12: sp^3 to sp^2 ratio and comparison

Sample	sp^3	sp^2	sp^3/sp^2	Thermal Conductivity (W/m-K)
Sample A	285.47 eV	284.4 eV	7.83	49
Sample B	285.41 eV	284.3 eV	8.1	105
Bulk Sample F	285.38 eV	-	-	695

Figure 78 and Table 12 depict the XPS data from two diamond materials. Sample A, 1.1µm diamond on silicon substrate, is a low carbon growth sample that showed a very low thermal conductivity (49W/m-K in-plane and 155 W/m-K cross-plane). Sample A showed the largest non-diamond peak in the UV Raman spectra. This sample was compared to Bulk Sample F which was a 525 µm sample with an effective thermal conductivity measured as 695 W/m-K. The two samples have a very distinct peak around 285.4 eV that corresponds to the sp^3 bonds on the top surface of the diamond. The distinction between the two samples is evident by looking to either side of the sp^3 main peak. Sample A has a large peak for sp^2 bonded carbon as well as C-O contamination on

the surface due to air exposure in the growth process [78]. Sample B exhibited similar peaks of sp^2 and C-O contamination but with a lower sp^3 to sp^2 ratio. This non diamond carbon greatly reduces the overall thermal conductivity and makes evident that the Sample A is of much poorer quality.

4.4 Summary and Conclusion

Measurement techniques such as Raman thermography, TDTR, electrical resistance, and 3 omega require diamond modification in order to extract thermal properties. These experiments can take days to weeks. In order to more rapidly understand the quality of a specific diamond sample and how that relates to thermal conductivity, four methods were used. By using the Raman spectrum, which takes about 1 second, the comparative amount of graphitic or non-diamond carbon can be deduced. The Raman spectrum can also provide information on the FWHM of the samples of interest. The higher the quality of diamond, the narrower the peak at the 1332 cm^{-1} Raman shift. A 2nd degree polynomial function was fit to the thermal conductivity vs. FWHM.

FTIR provided information on the absorbance of the CH bonds in the microstructure. The CH absorbance correlates to the effective thermal conductivity because the more CH bonds that are present in the sample, the greater the defects which increases overall phonon scattering. A 2nd degree polynomial function was fit to the thermal conductivity vs. integrated area in the CH stretching region. FTIR was only able to accurately measure samples that were greater than 20μm in thickness. XPS was a surface technique that measured the top 10nm. The carbon peaks were around 284-285eV, where both sp^3 and sp^2 peaks are present. XPS obtained a ratio of the sp^3/sp^2

bonds on the surface of the diamond. These four techniques show promise in the field of quick screening methods to determine relative thermal conductivity.

CHAPTER 5: MEASUREMENT AND MODELING OF GAN ON SIC/DIAMOND HEMT DEVICES

5.1 Introduction

Non-contact optical thermal measurements can be conducted on diamond structures as made evident in the previous chapters. Similar measurement techniques can be used to measure the GaN temperature in actual devices in real world conditions. These temperature measurements can provide substantial information into devices thermal performance under various power conditions.

With the use of accurate temperature measurements in real world devices, advanced thermal modeling can be completed in order to vary parameters to improve performance and reliability of these devices. Electro-thermal modeling of these devices can be a difficult task due to the very fine meshing requirements in the active region. Device performance is very sensitive to material defects in the active region which can be extremely difficult to assess and model. Whereas, thermal models use a uniform heat flux in the active region to accurately depict the heat flow from the active region to the ambient conditions.

In this chapter, device measurements on an AlGaN/GaN HEMT with a silicon carbide substrate are conducted at various power conditions. A thermal model was developed to characterize the temperature profile in these devices and ensure accuracy. This model was then altered to include various diamond substrates that resemble the thermal properties that were deduced in the previous sections.

5.2 Device Measurements

In order to better understand the application of diamond as a substrate material in AlGaN/GaN HEMTs, temperature measurements on an operating device were tested at various power conditions. This device did not use a diamond substrate but rather a SiC substrate of 100µm in thickness. Temperature measurements were taken at various power conditions and various locations on the 10 finger HEMT. The 10x360µm device, with a 1.4 µm thick GaN layer, is pictured in Figure 79.

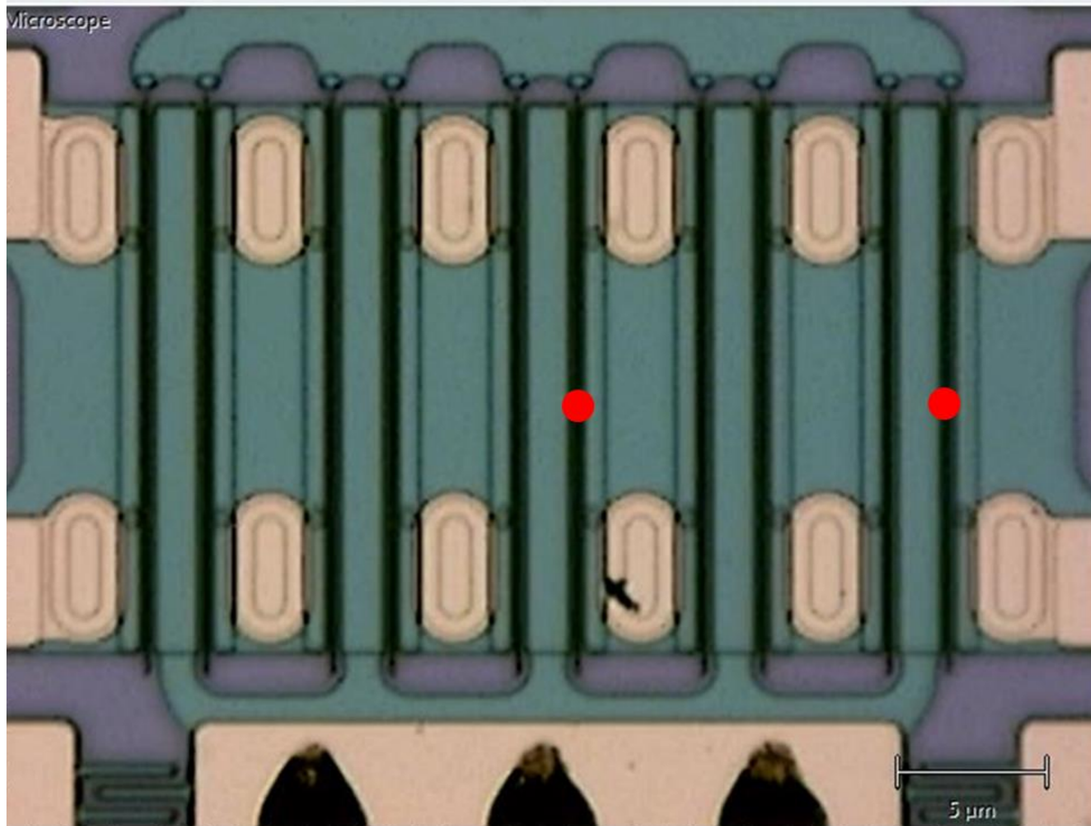

Figure 79: 10x360µm AlGaN/GaN HEMT on SiC substrate provided by CREE. The red dots represent the locations of the results at various power conditions.

The temperature measurements were obtained using a Renishaw InVia Raman system and 488 nm laser at 10.5mW and 100x lens as pictured in Figure 80.

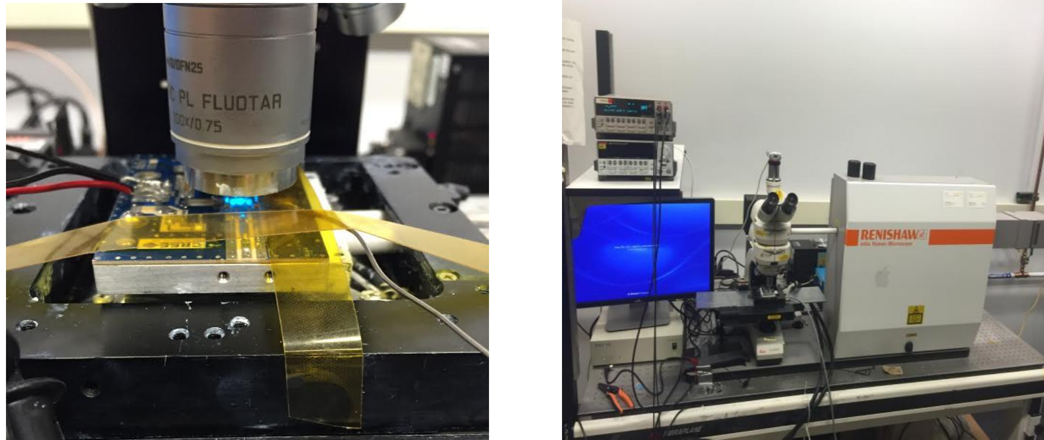

Figure 80: Experimental setup for powering HEMT and 100x lens used to take thermal measurements (left) and Renishaw InVia Raman system (right)

A schematic of the HEMT pictured in Figure 5 shows the overall heat flow from junction to ambient. The base temperature of 30°C was maintained using an INSTEC thermal stage and C300W industrial chiller. All measurements were taken in the drain side of the channel and at fully open conditions as seen in Figure 81 .

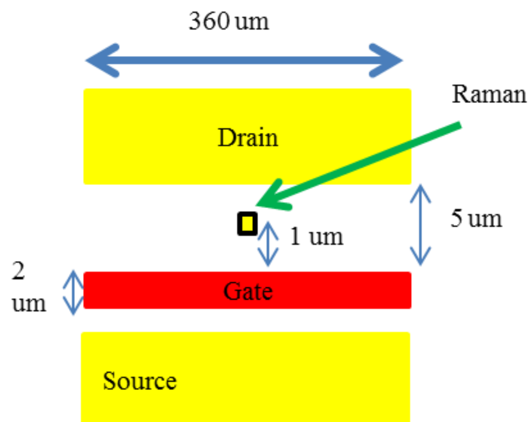

Figure 81: Diagram of HEMT device and location of measurements. Measurements were taken on the drain side of the channel. Raman measurements in GaN take a volumetric average over the spot size and through the GaN thickness.

The measurements were taken comparing the residual or unpowered state to the powered state. Ten unpowered measurements were taken before and after each power

conditions measurement which also consisted of ten measurements. The change in temperature was determined using the 2-peak-fit method [79]. This method utilizes the frequency shifts in E_2(high) and A1(LO) phonon modes in GaN to determine the change in temperature.

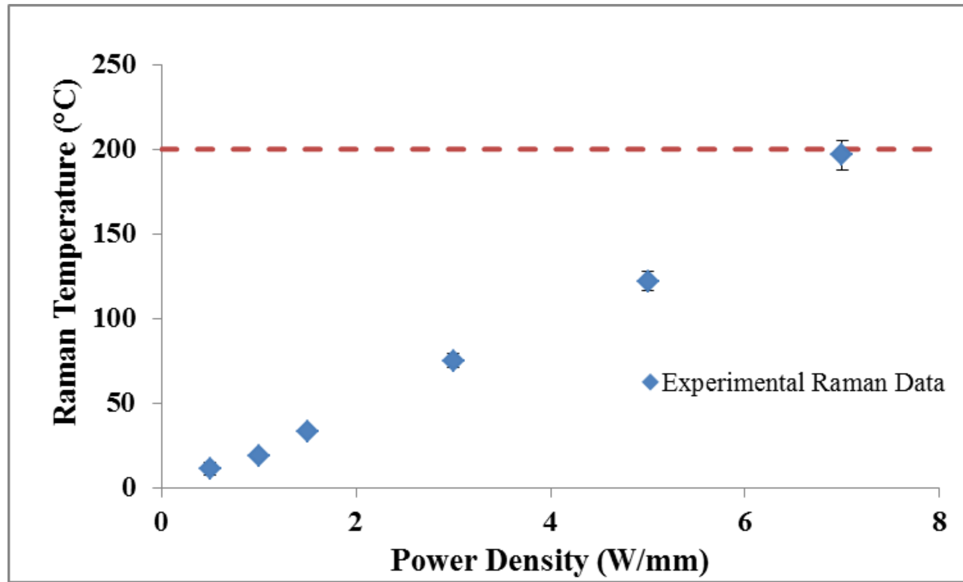

Figure 82: Temperature measurements of GaN in 10x360μm HEMT in center of 5th channel. 200°C was the temperature limit that was set to keep average device reliability over 10^5 hours

The temperature measurements with changing power density are seen in Figure 82, where the measurements were taken at the center of the 5th finger, as seen in Figure 79. These temperatures represent the volumetric average of the GaN layer over the spot size of approximately 1μm in diameter. These volumetric average temperatures are approximately 10% lower than the peak temperatures that are realized in the devices at the active region of the device. The line at 200°C represents the threshold in Figure 4, where increased peak temperatures will exponentially decrease time to failure. These measurements represent the through thickness average of the GaN layer, so the peak

temperature is approximately 10% higher than the Raman averaged temperature. This device would be able to perform reliably for an extended period of time near the 5W/mm power density limit. Any further increases in power would lead to a much quicker failure of the device. 200°C will be the cutoff peak temperature limit for the rest of this study.

5.2.1 Thermal Boundary Resistance on Transmission Line Measurements

In order to accurately determine the thermal boundary resistance of the GaN on SiC in these devices, similar devices were obtained from the same company with the same geometric conditions. Transmission line measurements (TLM) were conducted using structures fabricated on the GaN surface as seen in Figure 83. TLMs are used to determine the contact resistance in semiconductor materials by measuring the temperature decay across a powered channel and fitting that temperature profile to an analytical model.

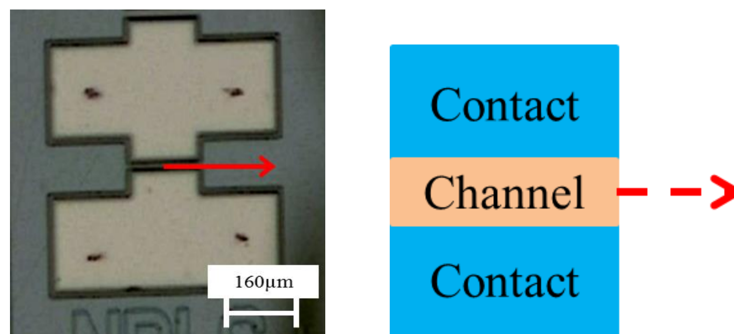

Figure 83: Transmission Line Measurement (TLM) schematic showing direction of temperature profile

An analytical solution for the temperature rise in a two layered structure with a discrete heat source was developed by Kevin Bagnall, *et al.*, and fitting it to the temperature profile in the channel using the 2 peak fit method in GaN, and GaN on SiC

thermal boundary resistance was deduced as seen in Figure 85 [80]. The analytical solution is a closed form, analytical solution for the temperature distribution in arbitrarily complex, rectangular, multilayer structures with a discrete heat flux source. It is based off of 3-D solid that is governed by the steady state heat conduction equation, which reduces to Laplace's equation without internal heat generation in Cartesian coordinates.

$$\frac{\partial^2\theta}{\partial x^2} + \frac{\partial^2\theta}{\partial y^2} + \frac{\partial^2\theta}{\partial z^2} = \nabla^2\theta = 0 \tag{4}$$

$$\theta(x, y, z) = T(x, y, z) - T_\infty \tag{5}$$

Figure 84 represents the geometry used for the solution. The model assumes adiabatic boundary conditions on the top of the first layer and on the sides. The bottom stack has a preset temperature conditions set to 30°C for this experiment. The TBR was determined to be 65.1 m^2K/GW using a Levenberg-Marquardt algorithm.

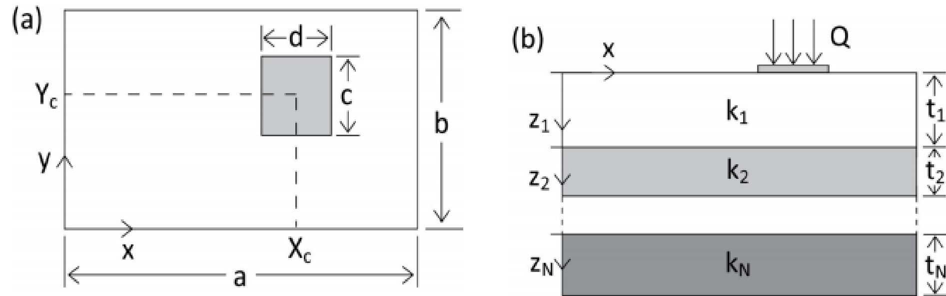

Figure 84: Schematic of structure layout for a sing rectangular heat source on complex, multilayered structure. (a) Top view of the xy-plane. (b) Side view of the xz plane [80].

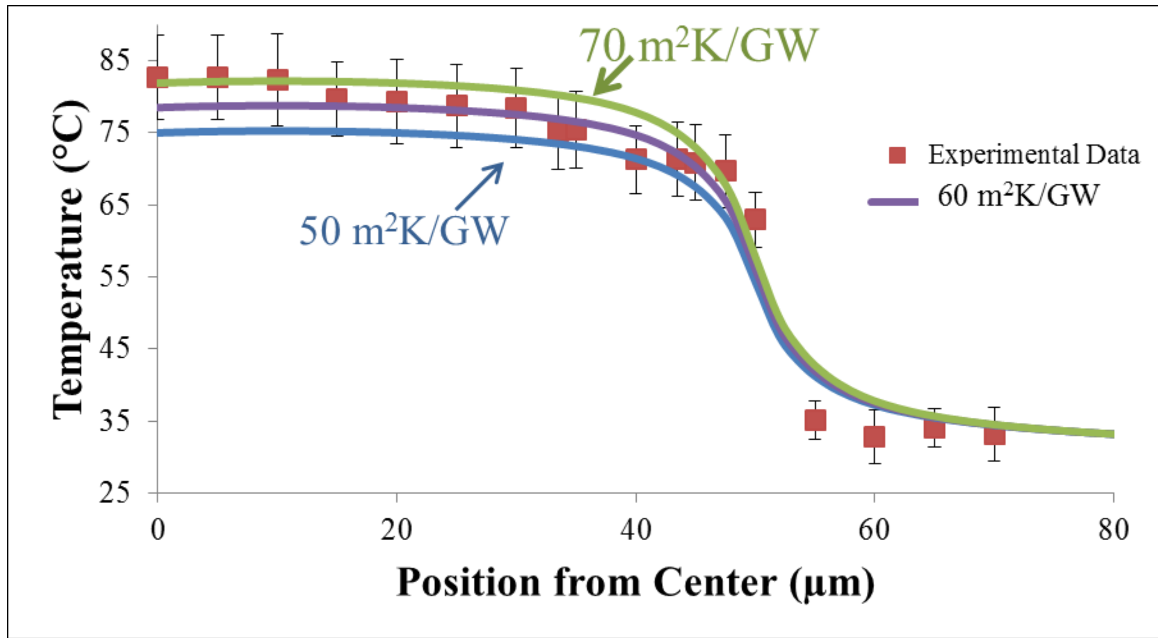

Figure 85: Temperature decay through TLM for GaN on SiC. Each data point corresponds to a temperature measurement made in the channel and the curves represent changes in the GaN on SiC TBR. Using the analytical solution, the TBR was determined to be 65.1 m^2K/GW.

5.3 Modeling

Using the geometry of the device, the temperature measurements, and the thermal boundary resistance of GaN on SiC, a finite element analysis (FEA) model was created in ANSYS Workbench 16.2. This model utilized the thermal properties as seen in Table 13.

Table 13: Thermal properties of materials used in FEA model [11]

Material	Thermal Conductivity (W/m-K)
GaN	$K = 150 * (\frac{T}{300})^{-1.4}$
6H-SiC	$K = 387 * \left(\frac{T}{293}\right)^{-1.49}$
Copper (Cu)	$K = 387$
Diamond	Varied Anisotropically

The experimental structure is shown in Figure 86, where there are multiple layers between the area on interest, the active region in the GaN, and the heat sink. This experimental setup utilized thermal paste and solders to connect some of the layers; and it is difficult to determine the exact thickness of each layer due to the device packaging. To simplify the ANSYS simulations, an effective stack resistance is used to model the layers below the substrate. This reduction is shown in Figure 86.

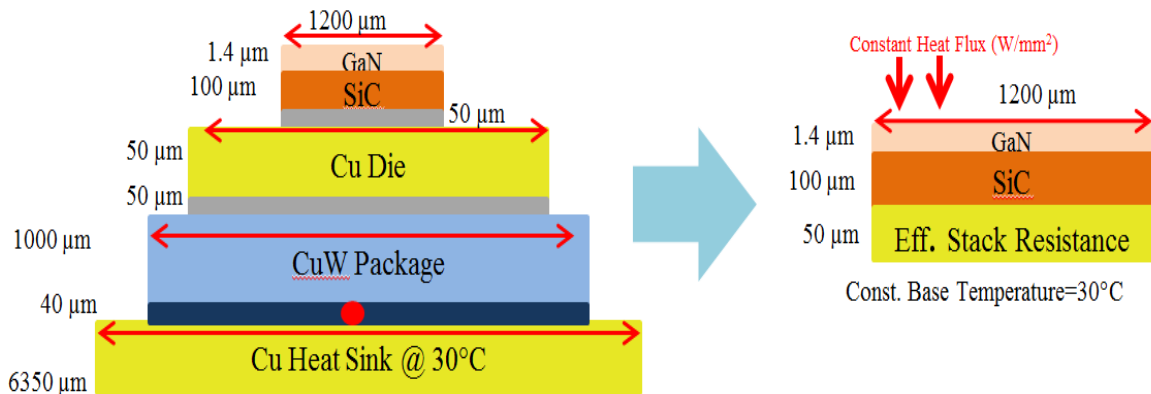

Figure 86: Actual GaN HEMT device structure (left) and GaN HEMT device modeled in ANSYS (right). The effective stack resistance represents the layers under the substrate that were modeled as one layer. The thermal resistance of this layer was altered to match the temperature profile in the highest power condition in the experimental results.

This model included the active HEMT layer, which includes AlGaN, GaN, and buffer layer as one layer with a thickness of 1.4µm. The heat sources were distributed evenly over the channel surface, since the model represented fully open channel conditions. The SiC substrate was 100µm thick and a thermal boundary resistance of 60 m^2K/GW was used from experimental results mentioned earlier between the GaN and SiC. The device was symmetrical which allowed for quarter symmetry to be used to

represent the model by implementing two adiabatic boundary conditions on the planes of symmetry. The temperature profile and mesh can be seen in Figure 87.

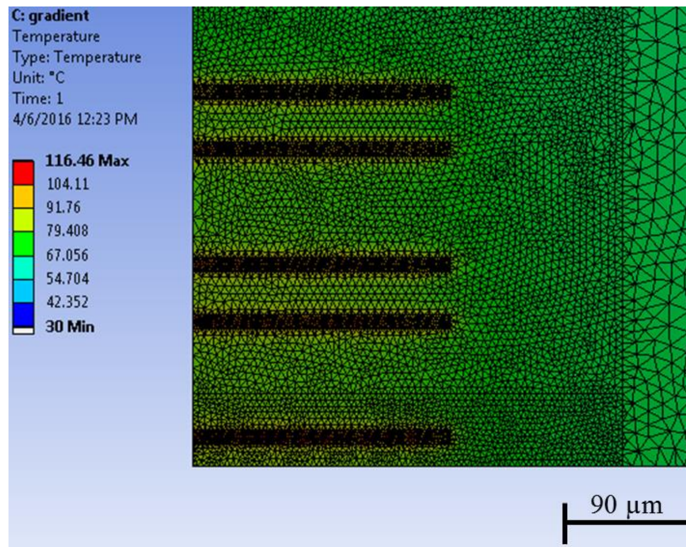

Figure 87: Meshing and Temperature Profile of 10x360μm HEMT Structure. Finer mesh was used in the area of heat generation and were Raman measurements were taken.

The approximation of the effective stack resistance for the entire device packaging was done through a parametric study changing the thermal conductivity of the bottom copper layer until the temperature profile matched that of the highest power condition at 7 W/mm. Since thermal resistance has a more significant impact at higher power densities, the model was fit to the experimental results obtained at the highest power densities applied to the devices as seen in Figure 88. This value was then held constant for all other predictions of temperature versus power response of the device in order to validate the model.

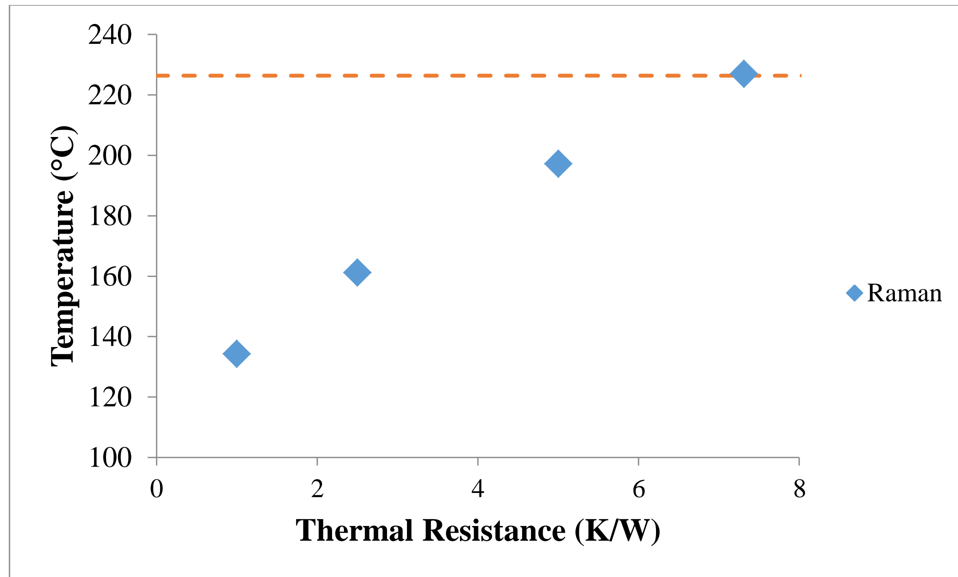

Figure 88: Effective stack resistance matching at 7 W/mm. The orange dotted line represents the volumetric average temperature of the Raman location.

In order to numerically evaluate the thermal and mechanical performance of the device at different powering conditions, appropriate boundary conditions must be applied. The power density applied is calculated by dividing the total power applied by the total gate width. Once having defined the power densities at which the device will be powered, the magnitudes of appropriate heat fluxes were calculated in order to satisfy these conditions as seen in Figure 89. To accurately represent fully open channel conditions, the area to which the heat flux is applied was determined to be the complete channel.

Other thermal boundary conditions applied to the model included imposing a constant base temperature of 30 °C to the bottom surface of the model. This condition permits an accurate representation of the experimental setup where a thermal stage connected to a chiller has been used to keep the base at a constant temperature of 30°C. For all other faces, an adiabatic boundary condition is assumed. The thermal simulation

using ANSYS Workbench 16.2 converged at approximately 150,000 elements for the quarter symmetry model. A more refined mesh was implemented near the areas of heat flow as well as in the area of Raman measurements.

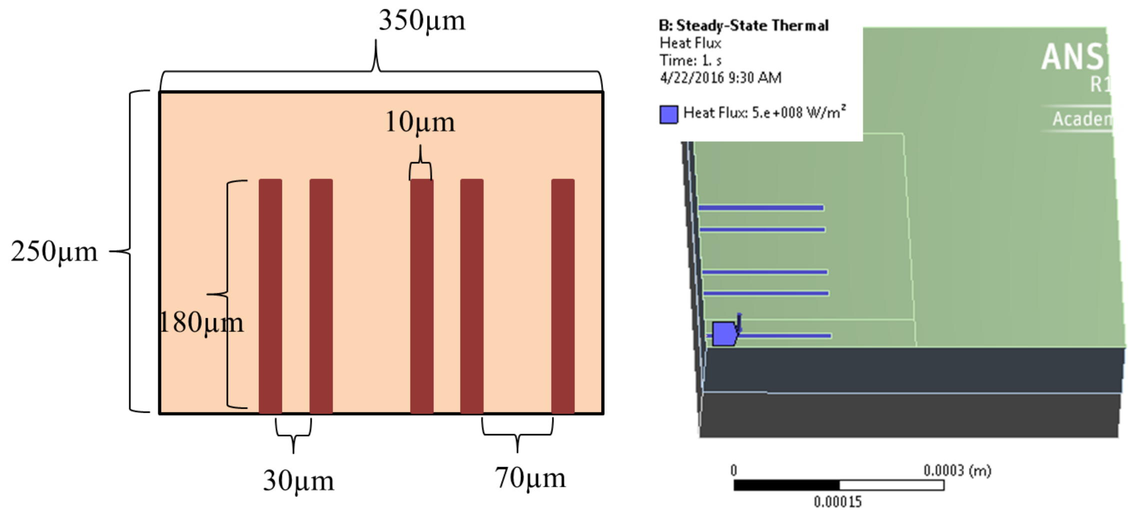

Figure 89: Geometry of quarter symmetry model. Areas where heat fluxes were applied. Constant base temperature of 30°C was held on the bottom surface with adiabatic conditions on the sides and top of the model.

5.3.1 Temperature Results

After the determination of the thermal resistance under the substrate, the model could be compared to the experimental results. The model and the expimental results match nicely as the model falls within the error bars of the measurements at all power conditions as seen in Figure 90.

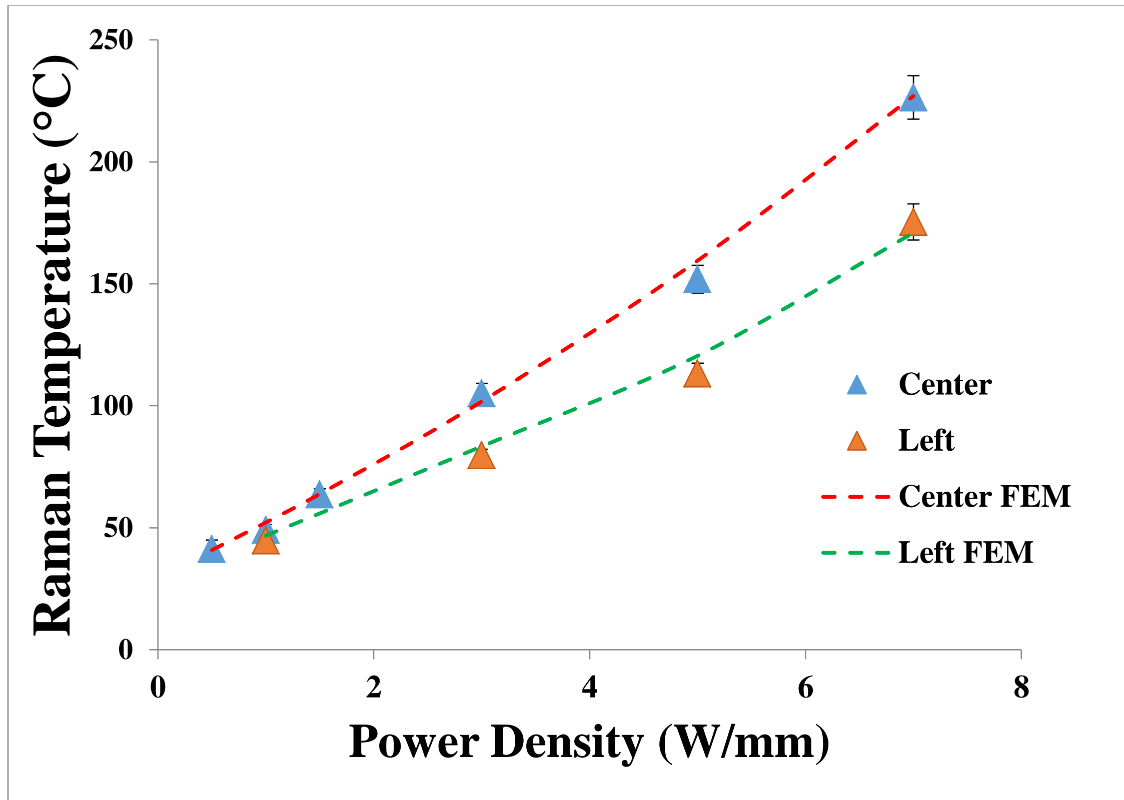

Figure 90: FEA Model to experimental temperature results comparison. Based on the optimized stack resistance, the model's volumetric average temperature was within the uncertainty of the experimental measurements.

The Raman temperature measurements are a volumetric average through the depth of the GaN due to the wide band gap of GaN (3.4eV) and the 488nm wavelength of the laser. In order to accurately model the through thickness average, a 1μm^2 body is created in the model to average the individual nodes and determine the average temperatrue in the 1μm spot size through the GaN in the area of interest. The difference in averaged temperatures and max temperatures are seen in Figure 91. These values differ apporximately 10% from each other over the power conditions of interest.

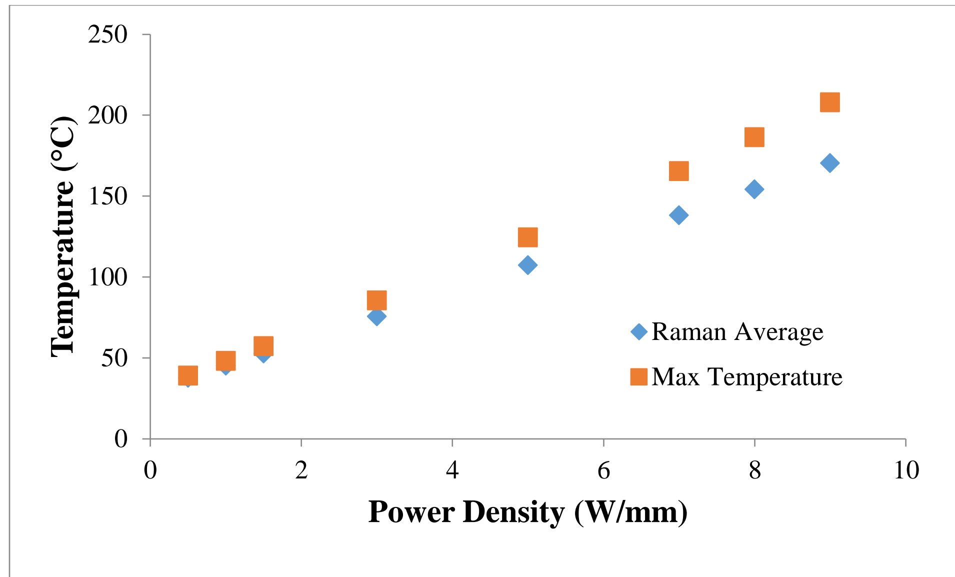

Figure 91: Raman averaged temperature over the 1 μm spot size and through the 1.4μm thick GaN layer compared to max temperature at various power conditions.

As seen in Figure 4, the overall lifetime of a HEMT will exponentially decrease beyond 200°C as the maximum temperature. This temperature occurs in the Raman probed area of interest. Using the geometries mentioned previously and a 60 m^2K/GW, as well as the thermal properties of a high quality diamond with a lateral thermal conductivity of 750 W/m-K, and assuming an anisotropic ratio of 2, a cross-plane conductivity of 1500 W/m-K was used in Figure 92. The SiC device is limited in its power density to slightly over 5W/mm, whereas the diamond device is able to withstand over a 50% increase in power density.

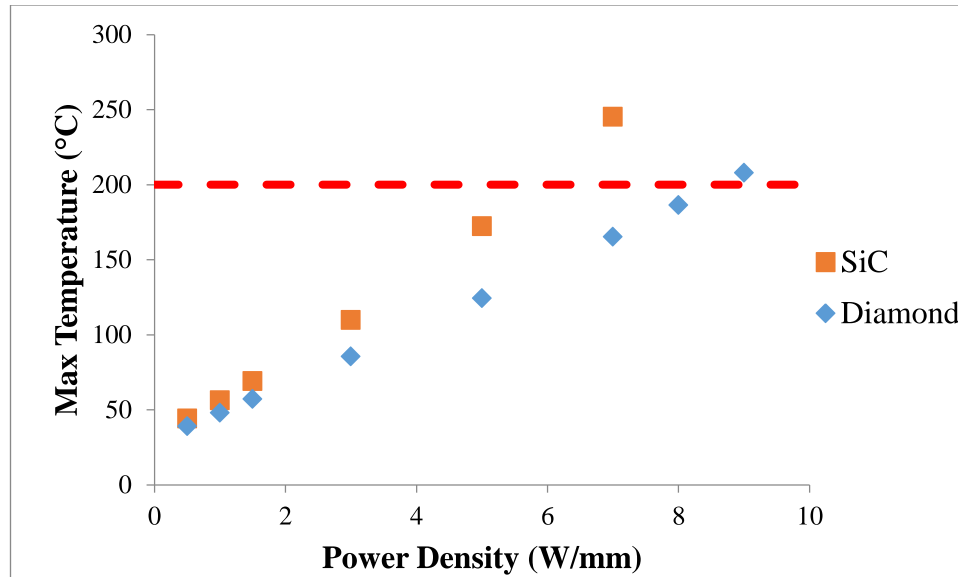

Figure 92: Maximum power density using device geometry, limiting the temperature to 200°C. Diamond substrates with the same TBR and lateral thermal conductivity of 750 W/m-K and vertical thermal conductivity of 1500 W/m-K.

5.3.2 Substrate and Thickness Comparison

The given dimensions of the SiC substrate material was 100µm, which allowed for a 5 W/mm power density limit. This power condition was used as a comparison of substrate thickness. The minimum temperatures in both SiC and diamond with high thermal conductivity diamond were obtained with a substrate thickness of 300µm as seen in Figure 93. The temperature decreases as the thickness increases between 10-250µm, as the spreading resistance dominates and the heat flux is unable to effectively spread laterally. As the thickness increases past 300µm, the one dimensional resistance dominates and additional thickness does not help heat spreading from the areas of heat flux.

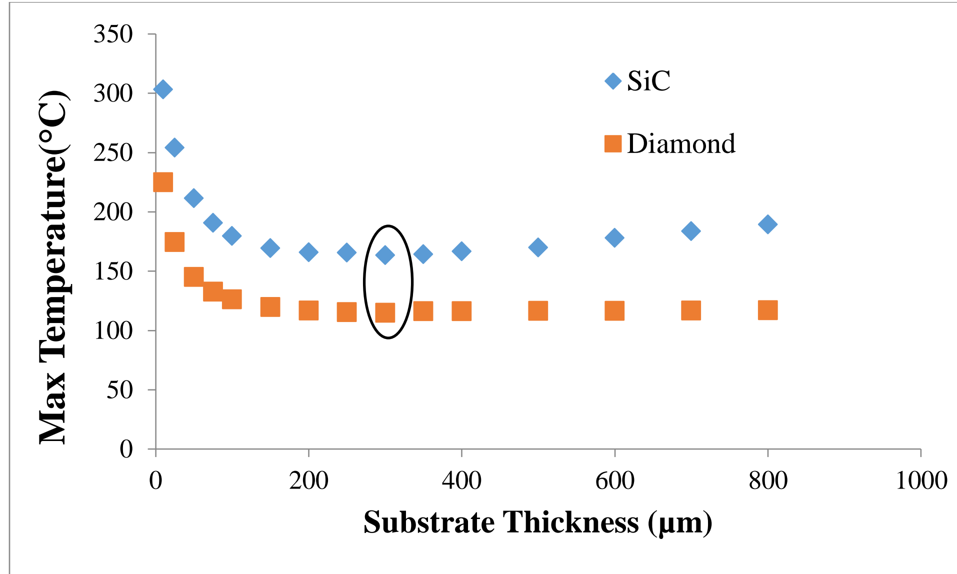

Figure 93: Maximum temperature for various substrate thickness at 5 W/mm. The minimum temperature for both SiC and Diamond substrates occurred at 300µm.

5.3.3 Effect of Diamond Thermal Properties

The implementation and growth of CVD diamond as a HEMT substrate has many factors that affect the overall thermal performance of the operating device. In this work, the anisotropic thermal conductivity and thermal boundary resistance were investigated in thin diamond films less than 1µm thick. The implementation of these thermal properties can be applied to an FEA model and optimized to greatly increase the reliability of GaN HEMT devices. Table 14 shows the variations of parameters, combining thermal conductivity and thermal boundary resistance that were found in this work and applies them to the FEA model. The model used a 300µm substrate thickness which was found as the optimal thickness in an earlier study.

Table 14: Design parameters used for FEA Model

Design		1/A	2	3	4	5
Thermal Conductivity (W/m-K)	In-plane Cross-plane	49 155	Gradient See Below	750 1500	750 1500	750 1500
TBR (m^2K/GW)		30	60	60	30	3

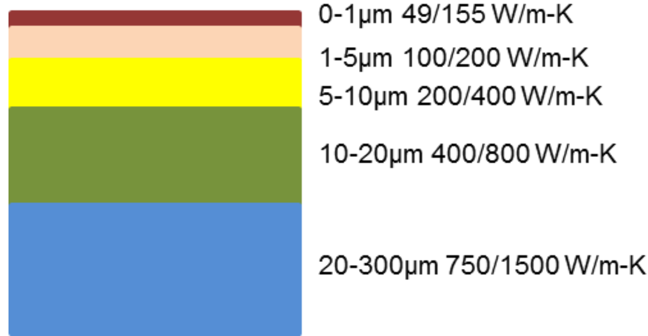

Figure 94: Thermal conductivity gradient used in parametric study. In-plane/Cross-plane thermal conductivity

Design point 1 in Table 14 used the conductivity of Sample A of 49 W/m-K in-plane and 155 W/m-K cross plane with a low thermal boundary resistance of 30 m^2K/GW. Design point 2 used a gradient of thermal conductivities as seen in Figure 94; it began with Sample A's conductivity in the first micron. The conductivity increased as the substrate thickness increased, assuming an anisotropic ratio of 2. The last 280 μm utilized the high thermal conductivity values of 750 W/m-K laterally and 1500 W/m-K. This represents the most accurate thermal properties in polycrystalline CVD diamond. Design point 3 used a high thermal conductivity and high thermal boundary resistance, while design point 4 used a lower TBR that was found in ring structures for diamond on Si in Figure 63. The final design point, 5, used the optimal values for implementation,

high thermal conductivity as well as the theoretically lowest possible value for TBR of 3 m^2K/GW [46]. The temperature depth profile in the first 10μm is seen in Figure 95.

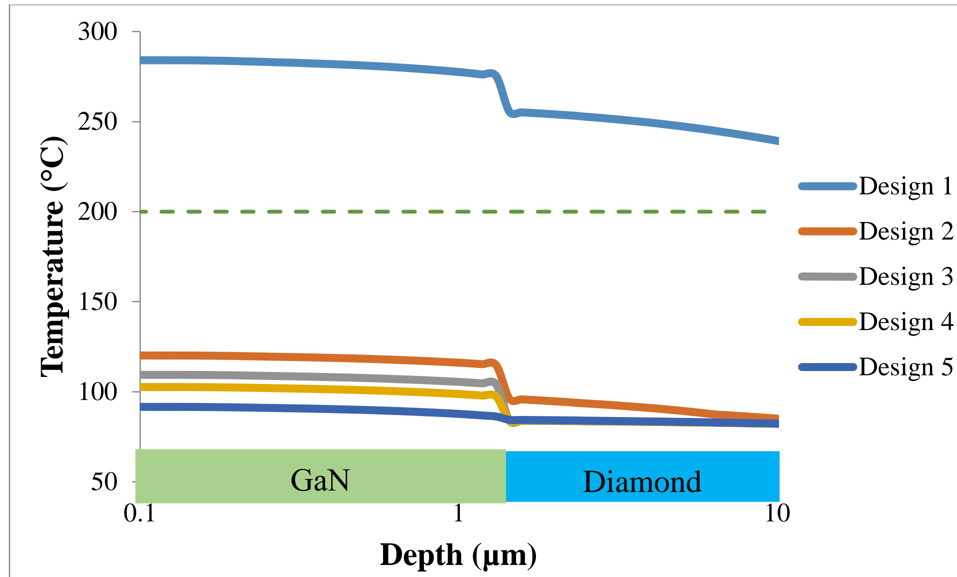

Figure 95: Depth temperature profile for various design points at 5 W/mm power density and 300μm substrate thickness.

Table 15: Temperature results from various design point

Design		1/A	2	3	4	5
Thermal Conductivity (W/m-K)	In-plane Cross-plane	49 155	Gradient See Below	750 1500	750 1500	750 1500
TBR (m^2K/GW)		30	60	60	30	3
Max Temperature (°C)		301.26	131.2	120.66	114.17	103.55

The thermal conductivity of Sample A as seen in Table 15 for 300μm thick substrate with a low TBR would be considerably above the peak temperature limit by over 100°C. All other design points would be well below the limit which would allow for increased power density or reduction in overall size. Design point 2 is the most realistic design point for the current state of GaN on diamond technology. Most samples have a large thermal conductivity gradient that increases as thickness increases, with a

relatively high TBR. This gradient significantly impedes heat flow as the first few microns have a much lower thermal conductivity due to the growth process where grain boundaries, defects, and impurities are most prominent. The growth of high conductivity diamond within the first nanometers of the nucleation region is critical for the implementation of diamond in HEMT structures.

5.4 Summary and Conclusions

Noncontact optical thermal measurements were taken of an AlGaN/GaN HEMT on SiC using Raman thermography with various power densities (0.5W/mm-7W/mm). Transmission Line Measurements were also taken in order to determine the TBR between the GaN and SiC, which was determined to be 65.1 m^2K/GW.

A finite element model was created based on the geometry and temperature dependent properties of the HEMT. The model used an effective stack resistance below the substrate to approximate thermal resistance, which was experimentally determined using the highest power conditions. The model was compared to the experimental results and all results were within the uncertainty values for each power density. A comparison of substrates, SiC and diamond, was accomplished showing a 50% increase in power density for diamond substrates staying below a maximum temperature of 200°C. A parametric study showed that for the above device, the optimal substrate thickness for SiC and diamond were both 300μm.

A final FEM comparison was accomplished using diamond as the substrate, varying anisotropic thermal conductivity and TBR with the GaN. As expected, the high thermal conductivity and low TBR designs had the lowest peak temperatures. A

conductivity gradient was used to simulate realistic diamond growth where the thermal conductivity is proportional to diamond thickness. This design point had a 9% increase in peak temperature with identical thermal conductivity 20μm from the nucleation region and same TBR. This shows the importance of future development in transitioning from the nucleation region with small grains and high defect density to high quality and high thermal conductivity diamond in the first few nanometers to act as a heat spreader.

CHAPTER 6: CONCLUSION AND FUTURE WORK

AlGaN/GaN HEMTs offer greatly improved performance over traditional transistors. Due to the heterostructre in the AlGaN/GaN interface, these devices are able to handle much higher power densities than previous devices. While this technology offers much promise for the future, their performance is limited by current passive thermal management techniques that use Si and SiC as a substrate material. In order to improve device performance and reliability, aggressive thermal management techniques are needed that do not increase size, weight and power of the overall device. CVD diamond grown on the GaN epilayers is a promising alternative to SiC or Si. This work looked at methods to determine thermal properties in chemical vapor deposition diamond and how these properties would affect thermal performance in operating AlGaN/GaN HEMTs.

The CVD process has many parameters that can affect the overall quality of the diamond. The nucleation density, method of activation energy and the percentage of carbon carrying gas can drastically affect the diamond quality as it coalesces and forms the desired columnar growth structure. The quality of CVD diamond directly affects the thermal properties of the diamond as a substrate material.

This work led to contributions that will aid in the development and integration of CVD diamond into electronics. These include:

(A) the development of test structures to measure ultrathin nanoscale diamond films. Test structures were designed and fabricated for lateral thermal conductivity measurements that attempted to isolate heat flow in the lateral direction. These

membrane structures had length to width ratios of 5:1 in order to more accurately compare FEA results to the analytical solution. Ring structures were developed and utilized to measure the cross-plane or vertical thermal conductivity and thermal boundary resistance. Due to small temperature drops through the diamond layer because it was only 1-1.1μm in thickness, large uncertainty was obtained for the vertical thermal conductivity.

B) This lead to measurements of the anisotropy of the films. The first sample that was measured, Sample A, a high carbon growth rate, showed poor thermal properties within the first micron. A lateral thermal conductivity of 49 W/m-k and a vertical thermal conductivity of 155 W/m-K were obtained, with a resulting anisotropic ratio of 3.16. Sample A had a measured TBR for diamond on silicon as 30 m^2K/GW. Sample B, a low carbon growth sample had a much higher lateral thermal conductivity of 85-107 W/m-K which varied based on the location in the wafer. These measurements were compared to various techniques and institutions to ensure accuracy and understand spatial variations along the diamond wafers.

C) The development of quick screening methods that were nondestructive developed an understanding of the overall quality of a diamond film. The Raman spectrum provided information on the non-diamond content in the sample and the FWHM of the diamond peak was correlated to effective thermal conductivity of the sample. FTIR was used to also determine diamond quality by observing the CH_x absorbance in various samples. XPS, a surface technique, offered a method to obtain the sp^3/sp^2 ratio in a sample's surface. .

D) Temperature measurements were taken for a GaN on SiC HEMT under various power conditions. Through the use of a transmission line measurement, the TBR between the GaN and SiC was determined to be 65.1 m^2K/GW. Using the experimental data and given geometry, the 10 x 360μm HEMT was modeled in ANSYS based on quarter symmetry. Sample A, the high carbon growth diamond, when used as a substrate material was a worse performer than SiC as a substrate. By creating a gradient where the anisotropic thermal conductivity increased with thickness, the overall peak temperatures were reduced by 140° C compared to Sample A. This modeling showed that increased effort must be placed on reducing the thermal boundary resistance to levels similar to the TBR for GaN on Si/SiC as well as improved the quality of diamond near the nucleation region in order to take advantage of diamond as a heat spreader.

This work set the groundwork for continued understanding of the microstructure of CVD grown diamond and how that relates to the thermal properties. Using the techniques described in this work, more measurements are needed on diamond of various thicknesses to have a full picture of CVD diamond and how the growth process affects the thermal properties. The vertical ring structures provided high uncertainties due to the 1.0 μm thickness of the diamond. New and novel devices need to be developed that reduce the uncertainty of these vertical measurements while keeping the thickness below or at 1μm. Raman thermography provides accurate temperature measurements with high spatial resolution, but the technique has the drawback that it must have specifically fabricated designs to measure thermal properties. Raman also takes a through thickness average of the temperature in diamond due to the sub bandgap laser, which can make accurate spatial measurements more difficult especially with thick diamond samples.

Raman thermography is a time intensive method to determine thermal conductivity; a more rapid transient method that does not require a transducer deposition is needed.

This study focused on silicon as the substrate of CVD grown diamond, increased interest needs to be placed on SiC as the substrate as well at looking at GaN on diamond and the resulting TBR. GaN on diamond HEMTs compared to GaN on SiC HEMTs with the same geometries will provide a more accurate comparison in real working conditions as to the improvements in thermal management. New methods to determine the grain size and defects near the nucleation region must be developed to reduce thermal resistance. While the thermal properties continue to be understood, more work must be placed on understanding the microstructure in the diamond and what has the largest effect on the quality of diamond near the nucleation region.

REFERENCES

1. Mishra, U.K., P. Parikh, and Y.-F. Wu, *AlGaN/GaN HEMTs-an overview of device operation and applications.* PROCEEDINGS-IEEE, 2002. **90**(6): p. 1022-1031.

2. Kim, J., et al., *Effective temperature measurements of AlGaN/GaN-based HEMT under various load lines using micro-Raman technique.* Solid-state electronics, 2006. **50**(3): p. 408-411.

3. Bar-Cohen[1], A., J.J. Maurer, and J.G. Felbinger. *DARPA's Intra/Interchip Enhanced Cooling (ICECool) Program*. in *CS MANTECH Conference, May 13th-16th*. 2013.

4. *Satellite*. 2016, http://www.spacetoday.org/Satellites/YugoWarSats.html.

5. *Tesla Image*. 2016.

6. Pierret, R.F., *Semiconductor device fundamentals*. 1996: Pearson Education India.

7. Wu, Y.F., et al., *Very high breakdown voltage and large transconductance realized on GaN heterojunction field effect transistors.* Applied physics letters, 1996. **69**(10): p. 1438-1440.

8. Green, D.S., et al., *GaN HEMT thermal behavior and implications for reliability testing and analysis.* physica status solidi (c), 2008. **5**(6): p. 2026-2029.

9. Brown, J.D., et al., *Performance, reliability, and manufacturability of AlGaN/GaN high electron mobility transistors on silicon carbide substrates.* ECS Transactions, 2006. **3**(5): p. 161-179.

10. Choi, S., et al., *Analysis of the residual stress distribution in AlGaN/GaN high electron mobility transistors.* Journal of Applied Physics, 2013. **113**(9): p. 093510.

11. Jones, J.P., *Electro-thermo-mechanical characterization of stress development in AlGaN/GaN HEMTs under RF operating conditions.* 2015.

12. Bhatnagar, M. and B.J. Baliga, *Comparison of 6H-SiC, 3C-SiC, and Si for power devices.* Electron Devices, IEEE Transactions on, 1993. **40**(3): p. 645-655.

13. Ambacher, O., et al., *Two dimensional electron gases induced by spontaneous and piezoelectric polarization in undoped and doped AlGaN/GaN heterostructures.* Journal of Applied Physics, 2000. **87**(1): p. 334-344.

14. Choi, S., et al., *The Analysis of Wide Band Gap Semiconductors Using Raman Spectroscopy*, in *Materials and Reliability Handbook for Semiconductor Optical and Electron Devices*, O. Ueda and J.S. Pearton, Editors. 2013, Springer New York: New York, NY. p. 545-582.

15. Mishra, U.K., et al., *GaN-Based RF Power Devices and Amplifiers.* Proceedings of the IEEE, 2008. **96**(2): p. 287-305.

16. Shinohara, K., et al., *Scaling of GaN HEMTs and Schottky diodes for submillimeter-wave MMIC applications.* Electron Devices, IEEE Transactions on, 2013. **60**(10): p. 2982-2996.

17. Liu, D., et al., *GaN-on-diamond electronic device reliability: Mechanical and thermo-mechanical integrity.* Applied Physics Letters, 2015. **107**(25): p. 251902.

18. Singhal, S., et al., *Reliability of large periphery GaN-on-Si HFETs.* Microelectronics Reliability, 2006. **46**(8): p. 1247-1253.

19. Chao, P., K. Chu, and C. Creamer. *A new high power GaN-on-diamond HEMT with low-temperature bonded substrate technology*. in *CS MANTECH Conference*. 2013. Citeseer.

20. Nakamura, S., S. Pearton, and G. Fasol, *The blue laser diode: the complete story*. 2013: Springer Science & Business Media.

21. Crystran, *Sapphire (Al2O3)*.

22. Kozawa, T., et al., *Thermal stress in GaN epitaxial layers grown on sapphire substrates.* Journal of applied physics, 1995. **77**(9): p. 4389-4392.

23. Leszczynski, M., et al., *Lattice parameters of gallium nitride.* Applied Physics Letters, 1996. **69**(1): p. 73-75.

24. *Properties*. Available from: http://www.ioffe.ru/SVA/NSM/Semicond/.

25. May, P.W., *CVD diamond: a new technology for the future?* Endeavour, 1995. **19**(3): p. 101-106.

26. May, P.W., *Diamond thin films: a 21st-century material.* Philosophical Transactions of the Royal Society of London A: Mathematical, Physical and Engineering Sciences, 2000. **358**(1766): p. 473-495.

27. van Dreumel, G.W.G., et al., *Realising epitaxial growth of GaN on (001) diamond.* Journal of Applied Physics, 2011. **110**(1): p. 013503.

28. Pomeroy, J., et al. *Achieving the best thermal performance for GaN-on-diamond*. in *Compound Semiconductor Integrated Circuit Symposium (CSICS), 2013 IEEE*. 2013. IEEE.

29. May, P.W. and Y.A. Mankelevich, *From Ultrananocrystalline Diamond to Single Crystal Diamond Growth in Hot Filament and Microwave Plasma-Enhanced CVD Reactors: a Unified Model for Growth Rates and Grain Sizes.* The Journal of Physical Chemistry C, 2008. **112**(32): p. 12432-12441.

30. Alomari, M., et al., *AlGaN/GaN HEMT on (111) single crystalline diamond.* Electronics letters, 2010. **46**(4): p. 1.

31. Altman, D., et al. *Analysis and characterization of thermal transport in GaN HEMTs on Diamond substrates*. in *Thermal and Thermomechanical Phenomena in Electronic Systems (ITherm), 2014 IEEE Intersociety Conference on*. 2014. IEEE.

32. Cho, J., et al., *Improved thermal interfaces of GaN–diamond composite substrates for HEMT applications.* Components, Packaging and Manufacturing Technology, IEEE Transactions on, 2013. **3**(1): p. 79-85.

33. Blevins, J., et al. *Recent progress in GaN-on-diamond device technology*. in *Proc. CS MANTECH Conf*. 2014.

34. Goodson, K. *Conduction Cooling Limits for Power Semiconductor Nanostructures (NJTT)*. 2012; Available from: https://nanoheat.stanford.edu/projects/conduction-cooling-limits-power-semiconductor-nanostructures-njtt.

35. Rossi, S., et al., *Thermal analysis of submicron nanocrystalline diamond films.* Diamond and Related Materials, 2013. **40**: p. 69-74.

36. Goodson, K.E., O.W. Kading, and R. Zachai. *Thermal resistances at the boundaries of CVD diamond layers in electronic systems*. in *American Society of Mechanical Engineers, Heat Transfer Division, (Publication) HTD*. 1994.

37. Goodson, K.E., *Thermal conduction in nonhomogeneous CVD diamond layers in electronic microstructures.* Journal of Heat Transfer, 1996. **118**(2): p. 279-286.

38. Graebner, J.E., et al., *Unusually high thermal conductivity in diamond films.* Applied Physics Letters, 1992. **60**(13): p. 1576-1578.

39. Graebner, J., et al., *Large anisotropic thermal conductivity in synthetic diamond films.* 1992.

40. Graebner, J.E., et al., *Diamond 1992 Thermal conductivity and the microstructure of state-of-the-art chemical-vapor-deposited (CVD) diamond.* Diamond and Related Materials, 1993. **2**(5): p. 1059-1063.

41. Francis, D., et al., *Formation and characterization of 4-inch GaN-on-diamond substrates.* Diamond and Related Materials, 2010. **19**(2–3): p. 229-233.

42. *Crystal Structure* The Structure and Entropy of Ice.

43. Kazuyuki, H., K. Makoto, and T. Yoshitaka, *Growth and Device Properties of AlGaN/GaN High-Electron Mobility Transistors on a Diamond Substrate.* Japanese Journal of Applied Physics, 2012. **51**(1S): p. 01AG09.

44. Hirama, K., Y. Taniyasu, and M. Kasu, *Heterostructure growth of a single-crystal hexagonal AlN (0001) layer on cubic diamond (111) surface.* Journal of Applied Physics, 2010. **108**(1): p. 013528.

45. Filippov, K.A. and A.A. Balandin. *Thermal Boundary Resistance and Heat Diffusion in AlGaN/GaN HFETs*. in *MRS Proceedings*. 2003. Cambridge Univ Press.

46. Sun, H., et al., *Reducing GaN-on-diamond interfacial thermal resistance for high power transistor applications.* Applied Physics Letters, 2015. **106**(11): p. 111906.

47. Kuzmik, J., et al., *Thermal characterization of MBE-grown GaN/AlGaN/GaN device on single crystalline diamond.* Journal of Applied Physics, 2011. **109**(8): p. 086106.

48. Yoonjin, W., et al. *Cooling Limits for GaN HEMT Technology*. in *Compound Semiconductor Integrated Circuit Symposium (CSICS), 2013 IEEE*. 2013.

49. Pomeroy, J.W., et al., *Low thermal resistance GaN-on-diamond transistors characterized by three-dimensional Raman thermography mapping.* Applied Physics Letters, 2014. **104**(8): p. 083513.

50. Pomeroy, J.W., et al., *Low thermal resistance GaN-on-diamond transistors characterized by three-dimensional Raman thermography mapping.* Applied Physics Letters, 2014. **104**(8): p. 083513.

51. Sarua, A., et al., *Thermal boundary resistance between GaN and substrate in AlGaN/GaN electronic devices.* Electron Devices, IEEE Transactions on, 2007. **54**(12): p. 3152-3158.

52. Cho, J., et al., *Phonon scattering in strained transition layers for GaN heteroepitaxy.* Physical Review B, 2014. **89**(11): p. 115301.

53. Manoi, A., et al., *Benchmarking of thermal boundary resistance in AlGaN/GaN HEMTs on SiC substrates: Implications of the nucleation layer microstructure.* Electron Device Letters, IEEE, 2010. **31**(12): p. 1395-1397.

54. Cho, J., et al., *Low thermal resistances at GaN–SiC interfaces for HEMT technology.* Electron Device Letters, IEEE, 2012. **33**(3): p. 378-380.

55. Kuzmík, J., et al., *Investigation of the thermal boundary resistance at the III-Nitride/substrate interface using optical methods.* Journal of Applied Physics, 2007. **101**(5): p. 054508.

56. Riedel, G.J., et al., *Reducing thermal resistance of AlGaN/GaN electronic devices using novel nucleation layers.* Electron Device Letters, IEEE, 2009. **30**(2): p. 103-106.

57. Pomeroy, J.W., et al., *Contactless Thermal Boundary Resistance Measurement of GaN-on-Diamond Wafers.* Electron Device Letters, IEEE, 2014. **35**(10): p. 1007-1009.

58. Yates, L., et al. *The Impact of Interfacial Layers on the Thermal Boundary Resistance and Residual Stress in GaN on Si Epitaxial Layers*. in *ASME 2015 International Technical Conference and Exhibition on Packaging and Integration of Electronic and Photonic Microsystems collocated with the ASME 2015 13th International Conference on Nanochannels, Microchannels, and Minichannels*. 2015. American Society of Mechanical Engineers.

59. Cho, J., et al. *Thermal Interface Resistance Measurements for GaN-on-Diamond Composite Substrates*. in *Compound Semiconductor Integrated Circuit Symposium (CSICs), 2014 IEEE*. 2014. IEEE.

60. Graebner, J., et al., *Report on a second round robin measurement of the thermal conductivity of CVD diamond.* Diamond and Related materials, 1998. **7**(11): p. 1589-1604.

61. Peschel, G., *Carbon-Carbon bonds: Hybridization.* obtained online from: http://www. physik. fu-berlin. de/einrichtungen/ag/ag-reich/lehre/Archiv/ss2011/docs/Gina_Peschel-Handout. pdf, published on, 2011. **5**(5).

62. Lee, S.T., Z. Lin, and X. Jiang, *CVD diamond films: nucleation and growth.* Materials Science and Engineering: R: Reports, 1999. **25**(4): p. 123-154.

63. Mitsuda, Y., et al., *The growth of diamond in microwave plasma under low pressure.* Journal of materials science, 1987. **22**(5): p. 1557-1562.

64. Touzelbaev, M. and K. Goodson, *Impact of nucleation density on thermal resistance near diamond-substrate boundaries.* Journal of thermophysics and heat transfer, 1997. **11**(4): p. 506-512.

65. Wang, S.G., et al., *CVD diamond nucleation enhanced by ultrasonic pretreatment using diamond and mixture of diamond and TaC powders.* Diamond and Related Materials, 2002. **11**(9): p. 1683-1689.

66. Beechem III, T.E. and J.R. Serrano, *Raman Thermometry of Microdevices: Comparing Methods to Minimize Error*. 2011, Sandia National Laboratories (SNL-NM), Albuquerque, NM (United States).

67. De Wolf, I., *Raman spectroscopy: chips and stress.* Spectroscopy Europe, 2003. **15**(2): p. 6-13.

68. Lundt, N., et al., *High spatial resolution Raman thermometry analysis of TiO2 microparticles.* Review of Scientific Instruments, 2013. **84**(10): p. 104906.

69. Cahill, D.G., *Analysis of heat flow in layered structures for time-domain thermoreflectance.* Review of Scientific Instruments, 2004. **75**(12): p. 5119-5122.

70. Hu, X.J., et al., *3-omega measurements of vertically oriented carbon nanotubes on silicon.* Journal of Heat Transfer, 2006. **128**(11): p. 1109-1113.

71. Knight, D.S. and W.B. White, *Characterization of diamond films by Raman spectroscopy.* Journal of Materials Research, 1989. **4**(02): p. 385-393.

72. Beeman, D., et al., *Modeling studies of amorphous carbon.* Physical Review B, 1984. **30**(2): p. 870.

73. Nicolet, T., *Introduction to fourier transform infrared spectrometry.* Information booklet, 2001.

74. Tabbal, M., et al., *XPS and FTIR analysis of nitrogen incorporation in CN x thin films.* Surface and Coatings Technology, 1998. **98**(1): p. 1092-1096.

75. Twitchen, D., et al., *Thermal conductivity measurements on CVD diamond.* Diamond and related materials, 2001. **10**(3): p. 731-735.

76. McNamara, K.M., et al., *Identification of defects and impurities in chemical-vapor-deposited diamond through infrared spectroscopy.* Journal of Applied Physics, 1994. **76**(4): p. 2466-2472.

77. Watts, J.F. and J. Wolstenholme, *An introduction to surface analysis by XPS and AES.* An Introduction to Surface Analysis by XPS and AES, by John F. Watts, John Wolstenholme, pp. 224. ISBN 0-470-84713-1. Wiley-VCH, May 2003., 2003: p. 224.

78. Merel, P., et al., *Direct evaluation of the sp 3 content in diamond-like-carbon films by XPS.* Applied Surface Science, 1998. **136**(1): p. 105-110.

79. Choi, S., et al., *Thermometry of AlGaN/GaN HEMTs using multispectral Raman features.* Electron Devices, IEEE Transactions on, 2013. **60**(6): p. 1898-1904.

80. Bagnall, K.R., Y.S. Muzychka, and E.N. Wang, *Analytical solution for temperature rise in complex multilayer structures with discrete heat sources.*

Components, Packaging and Manufacturing Technology, IEEE Transactions on, 2014. **4**(5): p. 817-830.